Insights to the Relationship Between the Condensed Phase and the Gas Phase Structure of Proteins from Ion Mobility Mass Spectrometry Measurements

Meagan M. Gadzuk-Shea

A dissertation

submitted in partial fulfillment of the

requirements for the degree of

Doctor of Philosophy

University of Washington

2020

Reading Committee:

Matthew F. Bush, Chair

Robert Synovec

Frantisek Tureček

Program Authorized to Offer Degree:

Chemistry

University of Washington

Abstract

Insights to the Relationship Between the Condensed Phase and the Gas Phase Structure of Proteins from Ion Mobility Mass Spectrometry Measurements

Meagan M. Gadzuk-Shea

Chair of Supervisory Committee:

Associate Professor Matthew F. Bush

Department of Chemistry

This dissertation investigates the interplay between the condensed phase environment, the generation of charged droplets, and the gas phase structures of protein and protein complex ions. Nanoelectrospray ionization is used to generate gas phase ions from various solutions that retain varying degrees of the native structure. Ion generated from “native” like conditions, solutions with electrolyte concentration and neutral pH, retain noncovalent interactions and aspects of higher–order structure. Conversely, ions generated from acidified solutions with high organic content are unfolded and do not reflect native–like structures. Ion mobility–mass spectrometry (IM–MS) analysis enables gas phase structures to be separated by collision cross section (an approximation of shape) and charge and can be used to infer information about the solution behavior of the structures. Additional gas phase perturbations can be used in combination with IM–MS to increase the information gained in a single experiment. For example, cation-to-anion proton-transfer-reactions (CAPTR) and collisional activation (CIU) is combined with IM–MS to examine the relationship between charge, collision cross section, and condensed phase environment of a large, multi–domain protein. In CAPTR, protein cations are reacted with singly–charged

anions prior to IM separation to generate a series of charge–reduced product ions through proton–transfer reactions. In CIU, protein ions are subjected to increasingly energetic collisions with a neutral gas molecule to affect structural isomerization. The results from this work show that the charge and collision cross section of the CAPTR product ions depend strongly on the solution from which the original ion was generated, the charge state of the product ion, and, to a lesser extent, the charge state of the precursor. Furthermore, these results show that the structures initially assumed is the consequence of kinetic trapping and depend on the solution conditions from which the original ion was generated. In other work, a novel power supply for generating ions from nESI was implemented into an IM–MS platform. This device, a triboelectric nanogenerator (TENG), offers superior sample efficiency relative to conventional DC power supplies due to its ability to trigger nESI in a controlled and pulsed manner. Native–like protein and protein complex ions spanning a range of masses are produced from TENG mediated nESI and studied by IM–MS. Those results show that TENG–nESI produces ions that are statistically similar to those generated by conventional DC power supplies. However, some differences and drawbacks of the TENG device are evident and discussed in the context of leveraging the device for IM–MS analysis of native-like biomolecules. Finally, the electrochemical nature of the nESI process is assessed for its impact on solutions commonly implemented in native–MS workflows. Measuring the fluorescence ratio of a pH–sensitive probe at two wavelengths enabled changes in solution composition during nESI to be determined. The role of electrospray current, concentration of electrolyte, initial solution pH, and polarity of the applied potential are examined on timescales consistent with native MS experiments. Those results show that significant changes in solution composition occur during nESI under conditions used to study intact biomolecule structure, although to varying extents. A polarity–switching scheme was developed to mitigate the observed changes in solution and was demonstrated to be an effective strategy.

Dedication

To my Golden Nugget, Misa

Acknowledgements

The work presented in this dissertation and my success during graduate school would not have come to fruition without the help of friends and family. First, I must thank my graduate advisor, Prof. Matthew F. Bush. Matt found the perfect balance of mentorship and freedom. He provided invaluable insight, ideas, and criticism for each of my research endeavors. More importantly, Matt encouraged my growth as a person and scientist by teaching me the nuances of critical thinking and science communication. I would also like to thank the members of my exam committee, past and present, Prof. František Tureček, Prof. Robert Synovec, Prof. Miklos Guttman, Prof. Niels Andersen, Prof. Daniel Chiu, and Prof. James Bruce. The discussions that took place during and outside of my examinations were thought-provoking and pushed me to take my research to further bounds. I also thank my first research advisors, Dr. Adam Hill and Dr. CJ Jahncke. Their guidance during my senior year of undergraduate opened my eyes to the fun, stressful, and rewarding universe of scientific inquiry. Because of their mentorship, I chose to pursue an advanced degree and, for that, I will be eternally grateful.

There are many members of the UW chemistry department that were instrumental in my graduate career. On the administrative side, I thank Diana Knight (Advancement and Communications Manager) for being the key-master and a source of answers for all random questions, Krista Holden (former Graduate Program Coordinator) and Christine Gormley (current Graduate Program Coordinator) for promptly answering any and all questions about exam procedures. I also thank the stockroom manager, Lochlan Hickock, for keeping track of hundreds of orders and tolerating my panic when an order was missing.

I taught many quarters during graduate school, and there were many individuals that made those times easier and more fun. First, I must thank the late Thomas Leach. Quantitative Analysis and Bioinstrumental Analysis would have failed without the expertise of Tom. Not only did Tom teach me numerous useful tricks with lab equipment, but he was also a friend that was always willing to lend an ear to an exasperated TA. I also thank Martin Sadilek for the many fun conversations and help getting

students excited about mass spectrometry. Additionally, I thank Brandon Bol for preparing solutions and tracking down missing reagents at all hours when I was a disorganized mess.

The members of the Bush lab deserve more thanks than I can convey in words. I joined the Bush lab largely in a panicked whim because it 'felt right' and I am so grateful that I chose to follow that instinct. The camaraderie and support the Bush members have for each other fosters an environment that encourages collaboration and where one does not have to fear asking for help. A special thanks to Dr. Kenneth J. Laszlo, who took me under his wing when I first joined the lab. I had no experience with ion mobility, mass spectrometry, or working with proteins. Ken taught me how to run experiments, but also to have confidence in my abilities as scientist. Another special thanks to Evan Hubbard, who worked on Chapter 4 with me as an undergraduate researcher. Evan demonstrated impressive perseverance and helped me laugh off the failures and challenges of that project. I also thank Dr. Kimberly Davidson, Dr. Seoyong Hong, and Dr. Rae Eaton for the much-needed coffee breaks, scientific feedback, and chats. Dr. Sam Allen, I am grateful for your seemingly endless supply of solutions to any problem I brought to you. AnneClaire Wageman, I am so grateful for the office banter and for you being my most loyal bingo attendee. Daniele Canzani, thank you for always keeping me honest about my intolerance for heat. To both Daniele and ACW, thank you for diving into nonsensical math on the whiteboard and tolerating my untamable messiness in the office. Ben Zercher, thank you for conversations that made me think about research from new perspectives and the fun times on the ski slopes – nothing like a seasonal friend! Theresa, thank you for being a constant source of support and encouragement. You are incredibly smart and an amazing scientist, I cannot wait to see what you do. And last, but not least, I thank Casey Chen, Lindsey Ulmer, and Emily Pruitt for their helpful feedback and discussions.

I want to thank my cohort and the friends I have made during my time in graduate school. From first-quarter homework sessions to fifth-year brain trust beer Tuesdays, you all made graduate school the amazing (albeit trying) experience that it was. Thank you to those that kept me active in soccer and volleyball, the activities I did not realize I needed to keep me sane. Thank to the friends that went to raves

with me, because even when I am 50 years old, I will still love EDM and having friends to experience that with made it so much more special.

And finally, I thank my family. Although my parents thought I would pursue a career in art, they supported my decision to pursue the hard sciences, even if they did not understand it. To my mother (Mommy), thank you for always being there for me, especially when I teetered on giving up. To my father (Daddy), thank you for working tirelessly to provide me the opportunities I have been so lucky to have. To Connor, thank you for taking on this adventure with me. You have helped me grow so much over the past five years. You have been my rock, a constant that kept me grounded, and for that I thank you. Of course, I must mention the sunshine of my world, Misa (my golden retriever). I thank the Bush lab and Matt for welcoming Misa into the lab and allowing her to join me in the office almost every day. I like to think that everyone in CHL benefited from her adorable antics.

Nomenclature

ATD	Arrival time distribution
CRM	Charged-Residue Model
Da	Dalton, the unified atomic mass unit
DC	Direct Current
CAPTR	Cation-to-anion proton-transfer-reaction
C	CAPTR product ion charge state
e	elementary charge, 1.6021766208(98) x 10–19 C
E	Electric Field
EHSS	Exact Hard Sphere Scattering
He	helium, in reference to IM buffer gas
IM	Ion Mobility
kB	Boltzmann's constant, 1.38064852(79) x 10–23 J·K–1
μ	reduced mass, often between ion and neutral masses
MS	Mass Spectrometry
m/z	mass-to-charge ratio, the standard measurement unit in MS
N_2	nitrogen, in reference to IM buffer gas
nESI	Nanoelectrospray Ionization
Ω	ion-neutral collision cross section
P	CAPTR precursor ion charge state
PA	Projection Approximation
PDCH	Perfluoro-1,3-dimyethylcyclohexane
TM	Trajectory Method
rf	Radio-Frequency
t_D	drift time
TOF	time-of-flight, an MS analyzer

TABLE OF CONTENTS

Chapter 1: Introduction

1.1 General Overview

The functioning of all life relies on the structures and interactions of proteins and protein complexes.[1] A protein that starts as a nascent chain of peptides will fold to a highly specified structure that dictates the when, how, and what of its function.[1–3] Traditional condensed-phase techniques such as X-ray crystallography[4] and NMR spectroscopy[5] have played critical roles in determining the structures of many proteins. However, these techniques often fail to capture the inherent complexity of these systems with respect to structural intermediates, inter- and intra- molecular interactions, and dynamic ensembles.[3] Ion mobility (IM) – mass spectrometry (MS) has emerged as a technique capable of capturing these more transient and complicated aspects of biomolecule structures and dynamics. IM separates molecules by shape and mass spectrometry by mass-to-charge; together, these techniques offer a semi-orthogonal, two-dimensional, gas-phase separation that benefits from speed, sensitivity, and selectivity.[6] Building a complete understanding of how various aspects of IM–MS measurements influence the gas-phase structure and behavior of biomolecules is crucial to extending the utility of these techniques for evaluating biomolecules. In this dissertation, specific components of the IM–MS measurement are characterized to assess how each affects the results of the measurement. The results of this work evaluate power sources to generate gas-phase ions, the duration, magnitude, and polarity of the applied potential used to generate gas-phase ions, the relationship between condensed-phase environment, charge, and gas-phase structure, and the influence of rapid temperature cycling in solution prior to ionization.

1.2 Mass Spectrometry (MS)

MS is a gas-phase technique that separates ions by their mass-to-charge (*m*/*z)* ratio. All MS techniques contain three primary components: an ion source, mass analyzer, and a detector.[7] In a MS experiment, the analyte is converted into bare, gas-phase ions at the ion source, then directed using electric fields to the mass analyzer that separates the ions by their *m*/*z*; the separated ions are measured at

the detector, which converts the signals that comprise a mass spectrum.[8,9] Mass spectrometry was born out of efforts to measure the electron[10] and early implementations of it were confined to primarily physics applications (*i.e.*, measuring the weights of atoms and sub-atomic particles).[10–12] Indeed, a mass spectrum is, in its simplest form, a gas-phase scale for determining the weight of an analyte,[13] however significant advances in the technology during the past half-millennia have extended both the limits of this scale and the applications of MS.[10,14] Today, MS is an invaluable asset to fields ranging from forensic science[15] to drug discovery and development.[16] Many modern configurations of MS workflows incorporate additional instrument components that are used to further probe the structures of gas-phase analytes. Some of these additions include gas-phase, hydrogen-deuterium exchange,[17] electron dissociation sources.[18] ion-ion reactions,[19] various optical spectroscopies,[20,21], and IM.[22] Coupling MS with such components in addition to its unrivaled speed, sensitivity, and selectivity has enabled MS to become one of the most prevalent methods for studying gas-phase structure in recent decades.

1.3 Ionization of Protein Ions

Prior to the development of soft ionization techniques, producing charged gas phase structures involved high energy processes that would break covalent bonds in the analytes.[8,13] While this allowed experimenters to elucidate structures through predictable fragmentation,[23,24] they were limited to analytes that were small and had vapor pressures great enough to produce substantial gas phase molecules prior to ionization. The 1980's brought about two new ionization sources that opened the doors to examining much larger analytes. These two ionization sources are matrix-assisted-laser-desorption-ionization (MALDI)[25] and electrospray ionization (ESI)[26]. In MALDI, a sample is co-crystallized with a matrix which is irradiated with a laser beam that generates ions,[27] although the direct mechanism of ion formation is still not fully understood[28]. While MALDI is capable of producing ions of high mass analytes (>300 kDa)[10,29], it typically produces singly charged ions ($z = 1$) and therefore very high m/z ions[30]. ESI offers the persuasive difference from MALDI of generating ions directly from solutions rather than a solid substrate.[30,31] Additionally, ESI generates a distribution of multiply charged ions from an analyte

solution, enabling it to be implemented on many MS platforms, including those with lower maximum *m*/*z* limits.[9,26] Consequently, ESI is more commonly employed for the analysis of proteins, especially those generated under biologically relevant conditions which tend to generate signals in higher *m*/*z* regimes.[32]

1.4 Electrospray Ionization (ESI)

1.4.1 Overview: In ESI, gas-phase ions are generated by biasing a capillary that contains the analyte solution by kilovolts relative to the inlet of the mass spectrometer.[33] The application of a high potential creates a Taylor cone at the tip of the capillary, which becomes a plume of analyte-containing droplets.[33–35] The residual solvent evaporates from the analyte containing droplets to produce bare gas-phase analyte ions, which are then analyzed by the mass spectrometer. Figure 1.4.1 illustrates the basics of this procedure. The process by which bare ions are formed from the initially charged droplets is still not completely understood.[36–38] However, many studies suggest that accepted that small molecules follow an ion-evaporation model,[39,40] elongated structures like denatured proteins are thought to undergo chain ejection processes,[41] and ions of larger, globular macromolecules, such as native-like proteins, are thought to form via the charged-residue model.[9,38,42]

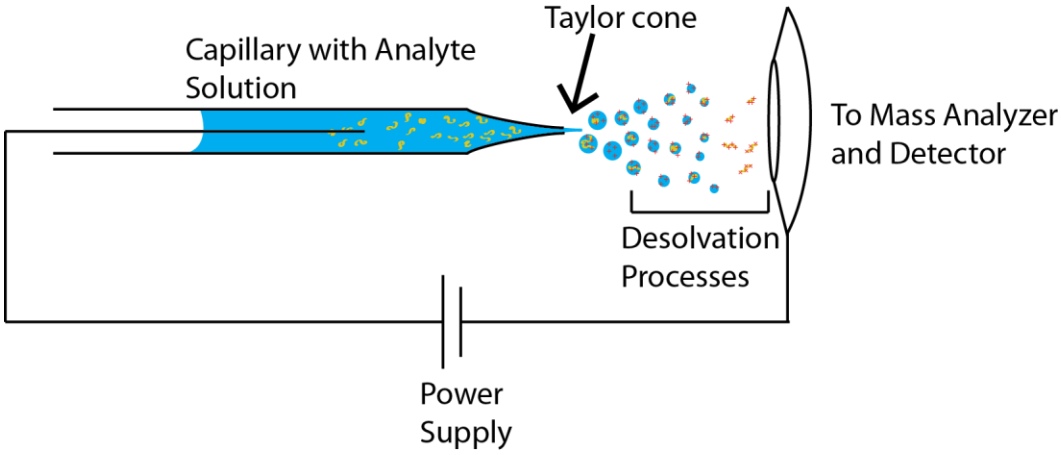

Figure 1.4.1. General overview of ESI components leading to the production and analysis of bare gas-phase ions.

1.4.2 ESI versus nESI: The first implementations of ESI used capillaries with inner diameters of ~100-200 µm, electric potentials in excess of 3 kV relative to ground, and external pumping to generate a flow of sample.[41,43,44] Such implementations of ESI are still common for the analysis of small molecules and metabolites, and some protein analysis workflows still use similar sources.[45–47] However, such configurations can suffer from high sample consumption and increased probability of nonspecific aggregation due to large droplet sizes.[48] In 1994, Wilm and Mann pioneered "micro electrospray" which aimed to reduce the size of the Taylor cone produced by the application of an electric potential and mitigate the aforementioned drawbacks of ESI.[35] This modified approach used flow rates of ≤ 25 nL·min^{-1} to produce a spray and produced droplets ≤ 200 nm, a significant decrease from the µm droplets produced by conventional ESI sources. The setup of ESI was further miniaturized in the development of nanoelectrospray ionization (nESI).[49] Generally, nESI utilizes capillaries with even smaller tips and no external pumping to promote electrospray; a potential of < 1.5 kV is typically sufficient enough to generate a Taylor cone and to create enough electric force to move the solution toward the capillary orifice.[48,49] All work presented in this dissertation uses nESI to produce gas-phase ions.

1.4.3 ESI to study biomolecules: Early applications of ESI to study biomolecules generated ions from acidified and organic solvents, which denatures the analyte structure and produces highly charged (low *m*/*z*) ions with broad charge-state distributions.[43,50] In 1993, the development of a mass spectrometer with higher *m*/z capabilities enabled the tetrameric form of Concanavalin A (103 kDa) to be observed when it was generated from a solutions near physiological pH.[51] This, in addition to advancements in the limits of mass analyzers[14] triggered a flurry of studies[52–55] examining the ability to retain native-like structures and noncovalent interactions in gas-phase biomolecules. These studies paved the development of the field of native MS.

1.4.4 Electrolytic nature of ESI: The ability to generate a continuous flow of charged droplets depends on the electrolytic nature of the electrospray process.[56,57] For example, when a positive potential is applied to the capillary electrode, charge separation of the ionic species within the solution will occur with positively charged species moving away from the electrode and toward the opening of the capillary.

Conversely, species of the opposite charge of the applied potential will gravitate toward the electrode where they will neutralize. At the opening of the capillary, where positive charges congregate, the solution distorts into a Taylor Cone from which positively–charged droplets emit when the surface tension is broken..[35,58] The departure of the positively charged species necessitates that more are produced in order to satisfy charge balance. The production of additional positively charged species can occur through multiple pathways including oxidation of the solvent, the electrode, and the analyte itself.[59] The rates at which negatively charged species are neutralized and positively charged species are expelled and replenished can be unequal, leading to a surplus buildup of REDOX reaction products.[57] Previous work has demonstrated that this can lead to changes in the composition of the electrospray solution.[57,59–61]

1.5 Charged-Residue Model

Previous work has reported a correlation between biomolecule mass and the charge states observed in the mass spectrum when the ions are generated from biologically relevant solutions.[38,42,62] This correlation suggests that the ions are formed through the charged-residue model (CRM). In the CRM, the initial droplet undergoes evaporation until charge repulsion exceeds the surface tension, at which point Coulombic fission occurs (Rayleigh Limit).[39,42,63] The resulting progeny droplets will evaporate off the final solvent molecules and the remaining charges are deposited onto the analyte structure, producing a bare and charged gas phase ion.

1.6 Native MS

Native MS refers to the technique of analyzing gas phase biomolecules generated from solution conditions that mimic the environment they would encounter in a biological system.[64–66] This typically involves a solution with some concentration of electrolyte, commonly ammonium acetate, that has been adjusted to a near-neutral pH.[67] When protein ions are generated from such solutions they exhibit relatively low charge states and narrow charge state distributions, which can make charge state and mass determination more challenging.[19,66] Previous work has shown that such solution conditions retain many

aspects of the native structure of proteins as well as preserve noncovalent interactions to other proteins and small molecules. This enables native MS to probe the stoichiometry, oligomeric state, and composition of protein complexes in solution.[65,68,69] For example, native MS has been leveraged to determine the role of lipid binding on the stability of membrane-protein oligomers, which is crucial to understanding many cell-signaling pathways.[70]

1.7 Ion Mobility (IM)

IM is an electrophoretic gas-phase separation technique that separates structures by size and charge.[71] There are multiple configurations of IM instrumentation that each possess their own advantages and disadvantages relative to each other; this has been reviewed elsewhere.[72] The majority of the IM work presented in this dissertation was conducted on an radio-frequency (rf) confining drift cell,[73] which consists of a series of stacked ring electrodes connected via a voltage divider with opposite phase rf AC currents applied to adjacent electrodes for enhanced ion confinement. The following discussion of IM measurements reflects those collected on this platform.

Separation occurs by applying a weak potential field to the drift region, which is often an enclosed chamber filled with an inert background gas. As ions enter the drift region, they experience two opposing forces that induce separation of different structures, the electric field, which pulls the ions down the axis of transmission, and collisions with the background gas, which slow the ions down. The ions reach a steady-state drift velocity (v_D) when these two opposing forces reach equilibrium. The occurrence of differing steady-state velocities results in the separation of ions. Figure 1.7.1 demonstrates how two ions with the same charge can exhibit different arrival-time distributions (ATD). This separation can occur because one of the structures is more elongated and takes longer to traverse the drift cell and the other structure is more compact and thus experiences fewer collisions with the background gas and travels the region in a shorter time.

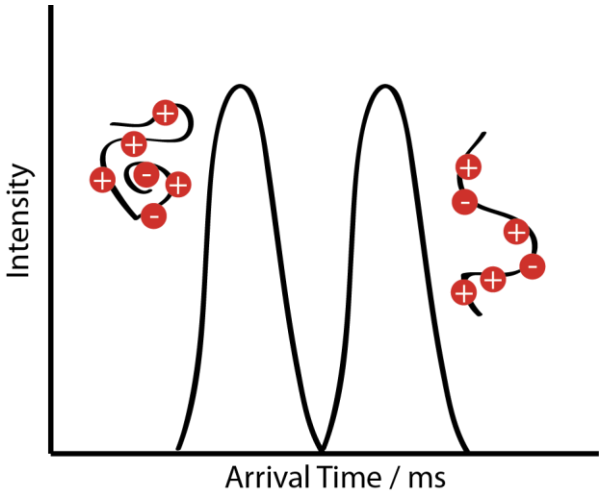

Figure 1.7.1 Mock IM separation demonstrating that smaller, more compact structures will traverse the mobility cell faster than an elongated structure with the same charge.

The net velocity that an ion will reach depends on the magnitude of the applied electric field, *E*, and the mobility of the ion, *K*:

$$v_D = KE = K\frac{V}{L} \tag{1.2}$$

The output of the ion mobility measurement is the arrival time (t_A), is a combination of the mobility-dependent component of the experiment (drift time, t_D) and the time an ion spends in the parts of the instrument that are not involved in the mobility separation (t_0):

$$t_A = t_D + t_0 \tag{1.3}$$

Mobility is an intrinsic property of an analyte and can be determined by measuring the time an ion takes to traverse the drift cell (t_D) over a range of E values and plotting the observed t_D as a function of 1/V. Examination of this relationship also allows the "dead" time (t_0) associated with IM separations to be determined from the y-intercept of these plots:

$$t_D = t_A - t_0 = \frac{L^2}{K}\frac{1}{V} \tag{1.4}$$

It is then possible to correct the observed t_A to determine the mobility-dependent time an ion spends in the drift region of the instrument.[74] This corrected drift time can be used to determine the mobility, *K*, of an ion. The *K* value can then be related to the collision cross section (Ω) of the ion structure based on the Mason-Schamp equation:[75]

$$\Omega = \frac{3ez}{16N}\left(\frac{2\pi}{\mu k_B T}\right)^{1/2}\frac{1}{K} \tag{1.5}$$

Where *e* is the elementary charge, *z* is the charge state of the ion, *N* is the number density of the drift gas, μ is the reduced mass of the ion-neutral collision pair, k_B is the Boltzmann constant, and *T* is the drift-gas temperature. The Ω value, to a crude first approximation, represents the rotationally averaged projection of the ion-neutral collision pair. Measurements of Ω values have proven a useful metric for evaluating gas-phase structures and comparing them to condensed-phase results and structural models.[6,76]

1.8 Ion Mobility Mass Spectrometry

During the early 1990's, the utility of combining IM to MS (IM–MS) for the analysis of protein structure began to be realized.[77–79] This semi-orthogonal combination offered improved opportunities for studying analyte conformations and structural dynamics relative to mass spectral analysis alone.[72,80] The release of the first commercially available IM–MS platform[81] led to an explosive growth in the application of IM–MS for studying biologically relevant molecules.[6] A significant contribution to this growth was the first observation of a native-like ion of a biomolecule, which provided definitive evidence that features of higher-order structure could be maintained in the absence of solvent during IM–MS analysis.[82]

1.9 Perturbing Structures of Gas Phase Ions

The application of native IM–MS to intact protein and protein complexes has pushed the ability to assess the structures and assemblies of analytes, many of which were previously unexaminable by alternative condensed phase techniques.[6] For example, native IM–MS has been leveraged in the determination of intrinsically-disordered protein conformations,[83] examining the structural variation associated with protein mutations,[84] and identifying substrate binding in membrane proteins.[85]

Additional tandem techniques are often used in combination with both native and non-native IM–MS to expand the information learned in a single experiment. Collision-induced unfolding (CIU), in which ions are sequentially accelerated into a gas-filled chamber prior to IM–MS separation and analysis, has been used to examine energy related processes such as ligand-binding stabilization[86] and subtle stability differences in biotherapeutic structures.[87] Cation-to-anion, proton-transfer reactions (CAPTR), in which the charge state of an ion is modulated through proton-transfer prior to IM–MS, has been used to examine the relationship between structure and charge state of a broad range of protein ions.[74,76,88,89] Condensed-phase heating prior to ionization and IM–MS analysis has been leveraged to examine structural ensembles of different proteins and protein complexes.[45,90,91] These are just a few examples in which the information gained from IM–MS experiments can be enhanced from incorporating additional forms of structural perturbation.

1.10 Outline of Present Study

This dissertation aims to deepen our understanding of factors that influence the appearance of mass and ion mobility spectra and how these factors inform what we learn about the relationship between solution- and gas-phase structures of biomolecules. Broadly speaking, nESI–IM–MS experiments consist of four major pains, as outlined in Figure 1.10.1: the (1) preparation of the of the analyte in solution, (2) generation of gas-phase ions through the application of an electric potential, (3) separation of the generated ions in the gas phase, and (4) analysis of the observed mass and ion mobility spectra. Part 3 reflects how the structures and dynamics of an analyte in the gas-phase respond as a result of (A) the

environment from which it was generated in parts 1 and 2 or (B) perturbations performed in the gas phase (*e.g.*, collisional activation). Part 4 is how our understanding of the preceding steps and their relation to condensed phase environment structure and behavior is advanced. In the following experiments, parts 1 and 2 are varied and closely examined for how these variations influence the appearance of the MS and IM spectra. Gas-phase perturbations, such as ion/ion reactions and collisional activation, are implemented to further inform on how structures of gas-phase ions differed in the condensed phase.

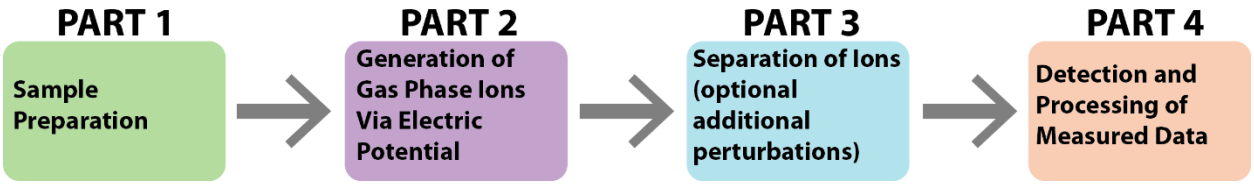

Figure 1.10.1 The four primary components of a nESI–IM–MS experimental workflow. This chart provides context for the various work presented in this dissertation.

Chapter 2 investigates how the characteristics of the condensed phase environment from which ions of serum albumin affect the appearance of the mass and ion mobility spectra. Serum albumin is a 66 kDa protein with 3 domains and 17 internal disulfide bonds. Ions are generated from five different solutions that preserve varying extents of the native fold. Cation-to-anion, proton-transfer reactions and collisional activation are used in combination to IM–MS to further understand how the condensed-phase environment influences the gas-phase structures and dynamics of a large, multi-domain protein with multiple disulfide bonds.

Chapter 3 moves forward in the IM–MS experiment and examines how the power supply used to apply the potential used in ionization influences the outcome of the measurement. A novel triboelectric nanogenerator (TENG) device[92] is used to generate ions for IM–MS analysis. The TENG device generates ions in controlled, user-defined pulses and presents a strategy for drastically improved sampling efficiency relative to continuous ion sources. The results of these experiments are systematically

compared to ions generated using a standard DC power supply at the same time for differences in collision cross section values and the appearance of the mass spectra. A comparison of the collision cross sections measured of ions generated via TENG to the values measured previously is also presented. Additionally, the coupling of the TENG device to a structures-for-lossless ion-manipulation (SLIM) ion mobility instrument demonstrates the ability of a single TENG event to generate adequate ions for IM–MS analysis.

Chapter 4 critically examines how the processes that occur during the electrospray process affect the characteristics of the electrospray solution, specifically in native MS solutions. Changes in the solution during native MS experiments have the potential to alter the structure of the analyte and invalidate the results of the experiment. Factors such as the magnitude of the electrospray current, the concentration of electrolyte in the solution, and the polarity of the applied application are each considered on timescales relevant to typical native MS applications. Strategies are discussed, and one is demonstrated, for the mitigation of the revealed electrospray–induced changes in the capillary solution.

1.11 References

(1) Fersht, A. R. From the First Protein Structures to Our Current Knowledge of Protein Folding: Delights and Scepticisms. *Nat Rev Mol Cell Biol* **2008**, *9* (8), 650–654. https://doi.org/10.1038/nrm2446.

(2) Englander, S. W.; Mayne, L. The Nature of Protein Folding Pathways. *PNAS* **2014**, *111* (45), 15873–15880. https://doi.org/10.1073/pnas.1411798111.

(3) Dill, K. A.; MacCallum, J. L. The Protein-Folding Problem, 50 Years On. *Science* **2012**, *338* (6110), 1042–1046. https://doi.org/10.1126/science.1219021.

(4) Shi, Y. A Glimpse of Structural Biology through X-Ray Crystallography. *Cell* **2014**, *159* (5), 995–1014. https://doi.org/10.1016/j.cell.2014.10.051.

(5) Wuthrich, K. Protein Structure Determination in Solution by Nuclear Magnetic Resonance Spectroscopy. *Science* **1989**, *243* (4887), 45–50. https://doi.org/10.1126/science.2911719.

(6) Lanucara, F.; Holman, S. W.; Gray, C. J.; Eyers, C. E. The Power of Ion Mobility-Mass Spectrometry for Structural Characterization and the Study of Conformational Dynamics. *Nature Chemistry* **2014**, *6* (4), 281–294. https://doi.org/10.1038/nchem.1889.

(7) Demartini, D. R. A Short Overview of the Components in Mass Spectrometry Instrumentation for Proteomics Analyses. *Tandem Mass Spectrometry - Molecular Characterization* **2013**. https://doi.org/10.5772/54484.

(8) Siuzdak, G. An Introduction to Mass Spectrometry Ionization: An Excerpt from The Expanding Role of Mass Spectrometry in Biotechnology, 2nd Ed.; MCC Press: San Diego, 2005. *JALA:*

Journal of the Association for Laboratory Automation **2004**, *9* (2), 50–63. https://doi.org/10.1016/j.jala.2004.01.004.

(9) Banerjee, S.; Mazumdar, S. Electrospray Ionization Mass Spectrometry: A Technique to Access the Information beyond the Molecular Weight of the Analyte https://www.hindawi.com/journals/ijac/2012/282574/ (accessed Mar 28, 2018). https://doi.org/10.1155/2012/282574.

(10) Griffiths, J. A Brief History of Mass Spectrometry. *Anal Chem* **2008**, *80* (15), 5678–5683. https://doi.org/10.1021/ac8013065.

(11) Beynon, J. H. The History of Mass Spectrometry and the Search for Zero. *Biomedical Mass Spectrometry* **1981**, *8* (9), 380–383. https://doi.org/10.1002/bms.1200080906.

(12) Yates Iii, J. R. A Century of Mass Spectrometry: From Atoms to Proteomes. *Nature Methods* **2011**, *8* (8), 633–637. https://doi.org/10.1038/nmeth.1659.

(13) Aebersold, R.; Mann, M. Mass Spectrometry-Based Proteomics. *Nature* **2003**, *422* (6928), 198–207. https://doi.org/10.1038/nature01511.

(14) Mehmood, S.; Allison, T. M.; Robinson, C. V. Mass Spectrometry of Protein Complexes: From Origins to Applications. *Annu Rev Phys Chem* **2015**, *66*, 453–474. https://doi.org/10.1146/annurev-physchem-040214-121732.

(15) R. Ifa, D.; M. Gumaelius, L.; S. Eberlin, L.; E. Manicke, N.; G. Cooks, R. Forensic Analysis of Inks by Imaging Desorption Electrospray Ionization (DESI) Mass Spectrometry. *Analyst* **2007**, *132* (5), 461–467. https://doi.org/10.1039/B700236J.

(16) Michnowicz, J. Mass Spectrometry in Drug Discovery and Development. *Nature Reviews Drug Discovery* **2002**, *1* (8), 651–652.

(17) Konermann, L.; Pan, J.; Liu, Y.-H. Hydrogen Exchange Mass Spectrometry for Studying Protein Structure and Dynamics. *Chemical Society Reviews* **2011**, *40* (3), 1224–1234. https://doi.org/10.1039/C0CS00113A.

(18) Mikesh, L. M.; Ueberheide, B.; Chi, A.; Coon, J. J.; Syka, J. E. P.; Shabanowitz, J.; Hunt, D. F. The Utility of ETD Mass Spectrometry in Proteomic Analysis. *Biochim Biophys Acta* **2006**, *1764* (12), 1811–1822. https://doi.org/10.1016/j.bbapap.2006.10.003.

(19) Laszlo, K. J.; Bush, M. F. Analysis of Native-Like Proteins and Protein Complexes Using Cation to Anion Proton Transfer Reactions (CAPTR). *J. Am. Soc. Mass Spectrom.* **2015**, *26* (12), 2152–2161. https://doi.org/10.1007/s13361-015-1245-4.

(20) I. Smith, S.; S. Brodbelt, J. Rapid Characterization of Cross-Links, Mono-Adducts, and Non-Covalent Binding of Psoralens to Deoxyoligonucleotides by LC-UV/ ESI-MS and IRMPD Mass Spectrometry. *Analyst* **2010**, *135* (5), 943–952. https://doi.org/10.1039/B924023C.

(21) Quick, M. M.; Crittenden, C. M.; Rosenberg, J. A.; Brodbelt, J. S. Characterization of Disulfide Linkages in Proteins by 193 Nm Ultraviolet Photodissociation (UVPD) Mass Spectrometry. *Anal. Chem.* **2018**, *90* (14), 8523–8530. https://doi.org/10.1021/acs.analchem.8b01556.

(22) Baker, E. S.; Clowers, B. H.; Li, F.; Tang, K.; Tolmachev, A. V.; Prior, D. C.; Belov, M. E.; Smith, R. D. Ion Mobility Spectrometry – Mass Spectrometry Performance Using Electrodynamic Ion Funnels and Elevated Drift Gas Pressures. *J Am Soc Mass Spectrom* **2007**, *18* (7), 1176–1187. https://doi.org/10.1016/j.jasms.2007.03.031.

(23) Shapiro, R. H.; Djerassi, C. Mass Spectrometry in Structural and Sterochemical Probelms. L.1 Fragmentation and Hydrogen Migration Reactions of ,-Unsaturated 3-Keto Steroids2 https://pubs.acs.org/doi/pdf/10.1021/ja01068a014 (accessed Oct 16, 2020). https://doi.org/10.1021/ja01068a014.

(24) Tokes, L.; Jones, G.; Djerassi, C. Mass spectrometry in structural and stereochemical problems. CLXI. Elucidation of the course of the characteristic ring D fragmentation of steroids https://pubs.acs.org/doi/pdf/10.1021/ja01022a025 (accessed Oct 16, 2020). https://doi.org/10.1021/ja01022a025.

(25) Karas, Michael.; Bachmann, Doris.; Hillenkamp, Franz. Influence of the Wavelength in High-Irradiance Ultraviolet Laser Desorption Mass Spectrometry of Organic Molecules. *Anal. Chem.* **1985**, *57* (14), 2935–2939. https://doi.org/10.1021/ac00291a042.

(26) Wong, S. F.; Meng, C. K.; Fenn, J. B. Multiple Charging in Electrospray Ionization of Poly(Ethylene Glycols). *J. Phys. Chem.* **1988**, *92* (2), 546–550. https://doi.org/10.1021/j100313a058.

(27) El-Aneed, A.; Cohen, A.; Banoub, J. Mass Spectrometry, Review of the Basics: Electrospray, MALDI, and Commonly Used Mass Analyzers. *Applied Spectroscopy Reviews* **2009**, *44* (3), 210–230. https://doi.org/10.1080/05704920902717872.

(28) Lu, I.-C.; Lee, C.; Lee, Y.-T.; Ni, C.-K. Ionization Mechanism of Matrix-Assisted Laser Desorption/Ionization. *Annual Rev. Anal. Chem.* **2015**, *8* (1), 21–39. https://doi.org/10.1146/annurev-anchem-071114-040315.

(29) Karas, Michael.; Hillenkamp, Franz. Laser Desorption Ionization of Proteins with Molecular Masses Exceeding 10,000 Daltons. *Anal. Chem.* **1988**, *60* (20), 2299–2301. https://doi.org/10.1021/ac00171a028.

(30) Zhou, J.; Lee, T. D. Charge State Distribution Shifting of Protein Ions Observed in Matrix-Assisted Laser Desorption Ionization Mass Spectrometry. *J Am Soc Mass Spectrom* **1995**, *6* (12), 1183–1189. https://doi.org/10.1016/1044-0305(95)00578-1.

(31) Nadler, W. M.; Waidelich, D.; Kerner, A.; Hanke, S.; Berg, R.; Trumpp, A.; Rösli, C. MALDI versus ESI: The Impact of the Ion Source on Peptide Identification. *J. Proteome Res.* **2017**, *16* (3), 1207–1215. https://doi.org/10.1021/acs.jproteome.6b00805.

(32) Donnelly, D. P.; Rawlins, C. M.; DeHart, C. J.; Fornelli, L.; Schachner, L. F.; Lin, Z.; Lippens, J. L.; Aluri, K. C.; Sarin, R.; Chen, B.; Lantz, C.; Jung, W.; Johnson, K. R.; Koller, A.; Wolff, J. J.; Campuzano, I. D. G.; Auclair, J. R.; Ivanov, A. R.; Whitelegge, J. P.; Paša-Tolić, L.; Chamot-Rooke, J.; Danis, P. O.; Smith, L. M.; Tsybin, Y. O.; Loo, J. A.; Ge, Y.; Kelleher, N. L.; Agar, J. N. Best Practices and Benchmarks for Intact Protein Analysis for Top-down Mass Spectrometry. *Nature Methods* **2019**, *16* (7), 587–594. https://doi.org/10.1038/s41592-019-0457-0.

(33) Fenn, J. B.; Mann, M.; Meng, C. K.; Wong, S. F.; Whitehouse, C. M. Electrospray Ionization–Principles and Practice. *Mass Spectrometry Reviews* **1990**, *9* (1), 37–70. https://doi.org/10.1002/mas.1280090103.

(34) Wilm, M. Principles of Electrospray Ionization. *Mol Cell Proteomics* **2011**, *10* (7). https://doi.org/10.1074/mcp.M111.009407.

(35) Wilm, M.; Mann, M. Electrospray and Taylor-Cone Theory, Dole's Beam of Macromolecules at Last? *International Journal of Mass Spectrometry and Ion Processes* **1994**, *136* (2–3), 167–180. https://doi.org/10.1016/0168-1176(94)04024-9.

(36) Hogan, C. J.; Carroll, J. A.; Rohrs, H. W.; Biswas, P.; Gross, M. L. A Combined Charged Residue-Field Emission Model of Macromolecular Electrospray Ionization. *Anal Chem* **2009**, *81* (1), 369–377. https://doi.org/10.1021/ac8016532.

(37) Ahadi, E.; Konermann, L. Modeling the Behavior of Coarse-Grained Polymer Chains in Charged Water Droplets: Implications for the Mechanism of Electrospray Ionization. *J Phys Chem B* **2012**, *116* (1), 104–112. https://doi.org/10.1021/jp209344z.

(38) Fernandez de la Mora, J. Electrospray Ionization of Large Multiply Charged Species Proceeds via Dole's Charged Residue Mechanism. *Analytica Chimica Acta* **2000**, *406* (1), 93–104. https://doi.org/10.1016/S0003-2670(99)00601-7.

(39) Kebarle, P.; Peschke, M. On the Mechanisms by Which the Charged Droplets Produced by Electrospray Lead to Gas Phase Ions. *Analytica Chimica Acta* **2000**, *406* (1), 11–35. https://doi.org/10.1016/S0003-2670(99)00598-X.

(40) Iribarne, J. V.; Thomson, B. A. On the Evaporation of Small Ions from Charged Droplets. *J. Chem. Phys.* **1976**, *64* (6), 2287–2294. https://doi.org/10.1063/1.432536.

(41) Konermann, L.; Ahadi, E.; Rodriguez, A. D.; Vahidi, S. Unraveling the Mechanism of Electrospray Ionization. *Anal. Chem.* **2013**, *85* (1), 2–9. https://doi.org/10.1021/ac302789c.

(42) Allen, S. J.; Schwartz, A. M.; Bush, M. F. Effects of Polarity on the Structures and Charge States of Native-Like Proteins and Protein Complexes in the Gas Phase. *Anal. Chem.* **2013**, *85* (24), 12055–12061. https://doi.org/10.1021/ac403139d.

(43) Fenn, J. B.; Mann, M.; Meng, C. K.; Wong, S. F.; Whitehouse, C. M. Electrospray Ionization for Mass Spectrometry of Large Biomolecules. *Science* **1989**, *246* (4926), 64–71. https://doi.org/10.1126/science.2675315.

(44) Whitehouse, C. M.; Dreyer, R. N.; Yamashita, Masamichi.; Fenn, J. B. Electrospray Interface for Liquid Chromatographs and Mass Spectrometers. *Anal. Chem.* **1985**, *57* (3), 675–679. https://doi.org/10.1021/ac00280a023.

(45) El-Baba, T. J.; Woodall, D. W.; Raab, S. A.; Fuller, D. R.; Laganowsky, A.; Russell, D. H.; Clemmer, D. E. Melting Proteins: Evidence for Multiple Stable Structures upon Thermal Denaturation of Native Ubiquitin from Ion Mobility Spectrometry-Mass Spectrometry Measurements. *J. Am. Chem. Soc.* **2017**, *139* (18), 6306–6309. https://doi.org/10.1021/jacs.7b02774.

(46) Gong, X.; Zhao, Y.; Cai, S.; Fu, S.; Yang, C.; Zhang, S.; Zhang, X. Single Cell Analysis with Probe ESI-Mass Spectrometry: Detection of Metabolites at Cellular and Subcellular Levels. *Anal. Chem.* **2014**, *86* (8), 3809–3816. https://doi.org/10.1021/ac500882e.

(47) Robinson, P. S. D.; Khairallah, G. N.; da Silva, G.; Lioe, H.; O'Hair, R. A. J. Gold-Mediated C□I Bond Activation of Iodobenzene. *Angewandte Chemie International Edition* **2012**, *51* (16), 3812–3817. https://doi.org/10.1002/anie.201108502.

(48) Karas, M.; Bahr, U.; Dülcks, T. Nano-Electrospray Ionization Mass Spectrometry: Addressing Analytical Problems beyond Routine. *Fresenius J Anal Chem* **2000**, *366* (6), 669–676. https://doi.org/10.1007/s002160051561.

(49) Wilm, M.; Mann, M. Analytical Properties of the Nanoelectrospray Ion Source. *Anal. Chem.* **1996**, *68* (1), 1–8. https://doi.org/10.1021/ac9509519.

(50) Mann, Matthias.; Meng, C. Kai.; Fenn, J. B. Interpreting Mass Spectra of Multiply Charged Ions. *Anal. Chem.* **1989**, *61* (15), 1702–1708. https://doi.org/10.1021/ac00190a023.

(51) Light-Wahl, K. J.; Winger, B. E.; Smith, R. D. Observation of the Multimeric Forms of Concanavalin A by Electrospray Ionization Mass Spectrometry. *J. Am. Chem. Soc.* **1993**, *115* (13), 5869–5870. https://doi.org/10.1021/ja00066a083.

(52) Schwartz, B. L.; Gale, D. C.; Smith, R. D.; Chilkoti, A.; Stayton, P. S. Investigation of Non-Covalent Ligand Binding to the Intact Streptavidin Tetramer by Electrospray Ionization Mass Spectrometry. *Journal of Mass Spectrometry* **1995**, *30* (8), 1095–1102. https://doi.org/10.1002/jms.1190300806.

(53) Loo, J. A. Studying Noncovalent Protein Complexes by Electrospray Ionization Mass Spectrometry. *Mass Spectrom. Rev* **1997**, 1–23.

(54) Loo, J. A.; Hu, P.; Smith, R. D. Interaction of Angiotensin Peptides and Zinc Metal Ions Probed by Electrospray Ionization Mass Spectrometry. *J Am Soc Mass Spectrom* **1994**, *5* (11), 959–965. https://doi.org/10.1016/1044-0305(94)80014-6.

(55) Eckart, K.; Spiess, J. Electrospray Ionization Mass Spectrometry of Biotin Binding to Streptavidin. *Journal of the American Society for Mass Spectrometry* **1995**, *6* (10), 912–919. https://doi.org/10.1016/1044-0305(95)00480-2.

(56) Blades, A. T.; Ikonomou, M. G.; Kebarle, Paul. Mechanism of Electrospray Mass Spectrometry. Electrospray as an Electrolysis Cell. *Anal. Chem.* **1991**, *63* (19), 2109–2114. https://doi.org/10.1021/ac00019a009.

(57) Van Berkel, G. J.; Kertesz, V. Using the Electrochemistry of the Electrospray Ion Source. *Anal. Chem.* **2007**, *79* (15), 5510–5520. https://doi.org/10.1021/ac071944a.

(58) Taylor Geoffrey Ingram. Disintegration of Water Drops in an Electric Field. *Proceedings of the Royal Society of London. Series A. Mathematical and Physical Sciences* **1964**, *280* (1382), 383–397. https://doi.org/10.1098/rspa.1964.0151.

(59) Van Berkel, G. J.; Asano, K. G.; Schnier, P. D. Electrochemical Processes in a Wire-in-a-Capillary Bulk-Loaded, Nano-Electrospray Emitter. *Journal of the American Society for Mass Spectrometry* **2001**, *12* (7), 853–862. https://doi.org/10.1016/S1044-0305(01)00264-1.

(60) Gatlin, C. L.; Turecek, Frantisek. Acidity Determination in Droplets Formed by Electrospraying Methanol-Water Solutions. *Anal. Chem.* **1994**, *66* (5), 712–718. https://doi.org/10.1021/ac00077a021.

(61) Pan, P.; Gunawardena, H. P.; Xia, Y.; McLuckey, S. A. Nanoelectrospray Ionization of Protein Mixtures: Solution PH and Protein PI. *Anal. Chem.* **2004**, *76* (4), 1165–1174. https://doi.org/10.1021/ac035209k.

(62) Tolić, L. P.; Anderson, G. A.; Smith, R. D.; Brothers, H. M.; Spindler, R.; Tomalia, D. A. Electrospray Ionization Fourier Transform Ion Cyclotron Resonance Mass Spectrometric Characterization of High Molecular Mass Starburst™ Dendrimers. *International Journal of Mass Spectrometry and Ion Processes* **1997**, *165–166*, 405–418. https://doi.org/10.1016/S0168-1176(97)00161-4.

(63) Dole, M.; Mack, L. L.; Hines, R. L.; Mobley, R. C.; Ferguson, L. D.; Alice, M. B. Molecular Beams of Macroions. *J. Chem. Phys.* **1968**, *49* (5), 2240–2249. https://doi.org/10.1063/1.1670391.

(64) Heck, A. J. R.; Heuvel, R. H. H. van den. Investigation of Intact Protein Complexes by Mass Spectrometry. *Mass Spectrometry Reviews* **2004**, *23* (5), 368–389. https://doi.org/10.1002/mas.10081.

(65) van den Heuvel, R. H. H.; Heck, A. J. R. Native Protein Mass Spectrometry: From Intact Oligomers to Functional Machineries. *Curr Opin Chem Biol* **2004**, *8* (5), 519–526. https://doi.org/10.1016/j.cbpa.2004.08.006.

(66) Kaddis, C. S.; Loo, J. A. Native Protein MS and Ion Mobility: Large Flying Proteins with ESI. *Anal. Chem.* **2007**, *79* (5), 1778–1784. https://doi.org/10.1021/ac071878c.

(67) Susa, A. C.; Xia, Z.; Tang, H. Y. H.; Tainer, J. A.; Williams, E. R. Charging of Proteins in Native Mass Spectrometry. *J Am Soc Mass Spectrom* **2017**, *28* (2), 332–340. https://doi.org/10.1007/s13361-016-1517-7.

(68) Barth, M.; Schmidt, C. Native Mass Spectrometry—A Valuable Tool in Structural Biology. *Journal of Mass Spectrometry* **2020**, *55* (10), e4578. https://doi.org/10.1002/jms.4578.

(69) Erba, E. B.; Petosa, C. The Emerging Role of Native Mass Spectrometry in Characterizing the Structure and Dynamics of Macromolecular Complexes. *Protein Science* **2015**, *24* (8), 1176–1192. https://doi.org/10.1002/pro.2661.

(70) Gupta, K.; Donlan, J. A. C.; Hopper, J. T. S.; Uzdavinys, P.; Landreh, M.; Struwe, W. B.; Drew, D.; Baldwin, A. J.; Stansfeld, P. J.; Robinson, C. V. The Role of Interfacial Lipids in Stabilizing Membrane Protein Oligomers. *Nature* **2017**, *541* (7637), 421–424. https://doi.org/10.1038/nature20820.

(71) Gabelica, V.; Marklund, E. Fundamentals of Ion Mobility Spectrometry. *Current Opinion in Chemical Biology* **2018**, *42*, 51–59. https://doi.org/10.1016/j.cbpa.2017.10.022.

(72) May, J. C.; McLean, J. A. Ion Mobility-Mass Spectrometry: Time-Dispersive Instrumentation. *Anal. Chem.* **2015**, *87* (3), 1422–1436. https://doi.org/10.1021/ac504720m.

(73) Allen, S. J.; Bush, M. F. Radio-Frequency (Rf) Confinement in Ion Mobility Spectrometry: Apparent Mobilities and Effective Temperatures. *J. Am. Soc. Mass Spectrom.* **2016**, *27* (12), 2054–2063. https://doi.org/10.1007/s13361-016-1479-9.

(74) Laszlo, K. J.; Munger, E. B.; Bush, M. F. Folding of Protein Ions in the Gas Phase after Cation-to-Anion Proton-Transfer Reactions. *J. Am. Chem. Soc.* **2016**, *138* (30), 9581–9588. https://doi.org/10.1021/jacs.6b04282.

(75) Mason; E.A.; McDaniel; E.W. *Transport Properties of Ions in Gases*; Wiley: New York, 1988.

(76) Laszlo, K. J.; Bush, M. F. Interpreting the Collision Cross Sections of Native-like Protein Ions: Insights from Cation-to-Anion Proton-Transfer Reactions. *Anal. Chem.* **2017**, *89* (14), 7607–7614. https://doi.org/10.1021/acs.analchem.7b01474.

(77) Helden, G. von; Wyttenbach, T.; Bowers, M. T. Inclusion of a MALDI Ion Source in the Ion Chromatography Technique: Conformational Information on Polymer and Biomolecular Ions. *International Journal of Mass Spectrometry and Ion Processes* **1995**, *146–147*, 349–364. https://doi.org/10.1016/0168-1176(95)04211-3.

(78) Smith, R. D.; Loo, J. A.; Loo, R. R. O.; Busman, M.; Udseth, H. R. Principles and Practice of Electrospray Ionization—Mass Spectrometry for Large Polypeptides and Proteins. *Mass Spectrometry Reviews* **1991**, *10* (5), 359–452. https://doi.org/10.1002/mas.1280100504.

(79) Wittmer, Doug.; Chen, Y. Hong.; Luckenbill, B. K.; Hill, H. H. Electrospray Ionization Ion Mobility Spectrometry. *Anal. Chem.* **1994**, *66* (14), 2348–2355. https://doi.org/10.1021/ac00086a021.

(80) Jurneczko, E.; E. Barran, P. How Useful Is Ion Mobility Mass Spectrometry for Structural Biology? The Relationship between Protein Crystal Structures and Their Collision Cross Sections in the Gas Phase. *Analyst* **2011**, *136* (1), 20–28. https://doi.org/10.1039/C0AN00373E.

(81) Pringle, S. D.; Giles, K.; Wildgoose, J. L.; Williams, J. P.; Slade, S. E.; Thalassinos, K.; Bateman, R. H.; Bowers, M. T.; Scrivens, J. H. An Investigation of the Mobility Separation of Some Peptide and Protein Ions Using a New Hybrid Quadrupole/Travelling Wave IMS/Oa-ToF Instrument. *International Journal of Mass Spectrometry* **2007**, *261* (1), 1–12. https://doi.org/10.1016/j.ijms.2006.07.021.

(82) Ruotolo, B. T.; Giles, K.; Campuzano, I.; Sandercock, A. M.; Bateman, R. H.; Robinson, C. V. Evidence for Macromolecular Protein Rings in the Absence of Bulk Water. *Science* **2005**, *310* (5754), 1658–1661. https://doi.org/10.1126/science.1120177.

(83) Pagel, K.; Natan, E.; Hall, Z.; Fersht, A. R.; Robinson, C. V. Intrinsically Disordered P53 and Its Complexes Populate Compact Conformations in the Gas Phase. *Angewandte Chemie International Edition* **2013**, *52* (1), 361–365. https://doi.org/10.1002/anie.201203047.

(84) Jurneczko, E.; Cruickshank, F.; Porrini, M.; Clarke, D. J.; Campuzano, I. D. G.; Morris, M.; Nikolova, P. V.; Barran, P. E. Probing the Conformational Diversity of Cancer-Associated Mutations in P53 with Ion-Mobility Mass Spectrometry. *Angewandte Chemie International Edition* **2013**, *52* (16), 4370–4374. https://doi.org/10.1002/anie.201210015.

(85) Laganowsky, A.; Reading, E.; Allison, T. M.; Ulmschneider, M. B.; Degiacomi, M. T.; Baldwin, A. J.; Robinson, C. V. Membrane Proteins Bind Lipids Selectively to Modulate Their Structure and Function. *Nature* **2014**, *510* (7503), 172–175. https://doi.org/10.1038/nature13419.

(86) Hyung, S.-J.; Robinson, C. V.; Ruotolo, B. T. Gas-Phase Unfolding and Disassembly Reveals Stability Differences in Ligand-Bound Multiprotein Complexes. *Chem Biol* **2009**, *16* (4), 382–390. https://doi.org/10.1016/j.chembiol.2009.02.008.

(87) Tian, Y.; Han, L.; Buckner, A. C.; Ruotolo, B. T. Collision Induced Unfolding of Intact Antibodies: Rapid Characterization of Disulfide Bonding Patterns, Glycosylation, and Structures. *Anal. Chem.* **2015**, *87* (22), 11509–11515. https://doi.org/10.1021/acs.analchem.5b03291.

(88) Laszlo, K. J.; Munger, E. B.; Bush, M. F. Effects of Solution Structure on the Folding of Lysozyme Ions in the Gas Phase. *J. Phys. Chem. B* **2017**, *121* (13), 2759–2766. https://doi.org/10.1021/acs.jpcb.7b00783.

(89) Laszlo, K. J.; Buckner, J. H.; Munger, E. B.; Bush, M. F. Native-Like and Denatured Cytochrome <Emphasis Type="Italic">c</Emphasis> Ions Yield Cation-to-Anion Proton Transfer Reaction Products with Similar Collision Cross-Sections. *J. Am. Soc. Mass Spectrom.* **2017**, *28* (7), 1382–1391. https://doi.org/10.1007/s13361-017-1620-4.

(90) Woodall, D. W.; Henderson, L. W.; Raab, S. A.; Honma, K.; Clemmer, D. E. Understanding the Thermal Denaturation of Myoglobin with IMS-MS: Evidence for Multiple Stable Structures and Trapped Pre-Equilibrium States. *J. Am. Soc. Mass Spectrom.* **2020**. https://doi.org/10.1021/jasms.0c00075.

(91) Woodall, D. W.; Brown, C. J.; Raab, S. A.; El-Baba, T. J.; Laganowsky, A.; Russell, D. H.; Clemmer, D. E. Melting of Hemoglobin in Native Solutions as Measured by IMS-MS. *Anal. Chem.* **2020**, *92* (4), 3440–3446. https://doi.org/10.1021/acs.analchem.9b05561.

(92) Li, A.; Zi, Y.; Guo, H.; Wang, Z. L.; Fernández, F. M. Triboelectric Nanogenerators for Sensitive Nano-Coulomb Molecular Mass Spectrometry. *Nature Nanotechnology* **2017**, *12* (5), 481–487. https://doi.org/10.1038/nnano.2017.17.

Chapter 2

Effects of Charge State on the Structures of Serum Albumin Ions in the Gas Phase: Insights from Cation-to-Anion Proton-Transfer Reactions, Ion Mobility, and Mass Spectrometry

This chapter is reproduced with permission from Meagan M. Gadzuk-Shea and Matthew F. Bush "Effects of Charge State on the Structures of Serum Albumin Ion in the Gas Phase: Insights from Cation-to-Anion Proton-Transfer Reactions, Ion Mobility, and Mass Spectrometry" *The Journal of Physical Chemistry B* **2018** *122* (43), 9947-9955, DOI: 10.1021/acs.jpcb.8b08427.

2.1 Abstract

Understanding the structures of proteins in the gas phase is essential for using gas-phase measurements to infer the properties of proteins in solution. Using serum albumin as a model, this study aims to expand our understanding of this relationship for a larger (66 kDa), multi-domain protein that contains 17 internal disulfide bonds. Gas-phase ions were generated from five solutions that preserve varying extents of native structure. Ion mobility (IM) mass spectrometry (MS), cation-to-anion proton-transfer-reactions (CAPTR), and energy-dependent IM were used to probe the relationship between structure, charge, and solution. Ions generated from increasingly disruptive conditions exhibited higher charge states and larger collision cross section values. The collision cross sections of all CAPTR products depend on the original solution, and to varying extents, the charge state of the product and the precursor. For example, the collision cross sections of CAPTR products from denaturing conditions are all significantly larger than those of the original native-like ions. Results from energy-dependent experiments show that the structures of the original ions from electrospray ionization and their CAPTR products are a consequence of kinetic trapping and depend on the higher-order structure and disulfide bonding of serum albumin in solution. This study builds on our understanding of the relationship between solution condition, disulfide bonding, collision cross section, and charge for a larger, multi-domain protein, which may be applicable to future characterization of biotherapeutics that share these structural features.

2.2 Introduction

The biological functions and activities of proteins depend inextricably on their higher-order structures.[1] With a detailed understanding of this relationship, it is possible to tailor the function of a protein by manipulating its stability, conformational distribution, solubility, and assembly.[2–4] This concept has been applied in therapeutic research and development. For example, knowledge of the insulin dimerization interface was exploited to introduce single amino acid substitutions that cause like-charge repulsion at the interface.[5] These substitutions do not disrupt the receptor binding region of the functional monomer, but reduce the fraction of total insulin that forms lower-activity dimers at clinical concentrations.[5,6] This dramatically decreases the food-related, time sensitivity of insulin intake for diabetic patients. Despite this and other successes,[6,7] our ability to study the dynamics, evolution, and characteristics of a protein structure remains hindered. Condensed-phase techniques play dominant roles in structural biology and biophysics,[8] but possess inherent limitations. These techniques convolve intra- and intermolecular forces, are hindered by the presence heterogeneous mixtures of structure,[9] and often require that proteins are amenable to high concentrations and/or crystallization. Such challenges restrict the proteins that may be studied by condensed-phase techniques.[10]

The study of "naked" proteins in the solvent-free environment of a mass spectrometer isolates the intrinsic, intramolecular interactions by eliminating interactions with solvent and surrounding molecules. Furthermore, mass spectrometry (MS) offers rapid analysis, requires small amounts of sample, and is applicable to many more proteins relative to conventional techniques.[11] MS has been used to determine the mass,[12,13] connectivity,[14] interactions,[15] and stoichiometry[16,17] of proteins and protein complexes. Ion mobility (IM) has emerged as a useful technique to couple with MS and provides a complementary dimension of analysis that is sensitive to shape and size.[18] This structural information is obtained by measuring the mobility of an ion in a buffer gas under an electric field, which can be converted to a collision cross section (Ω).[19]

Electrospray ionization from "native-like" solutions (*i.e.*, aqueous solutions with ionic strength and pH similar to physiological conditions) can yield protein ions with Ω values that are correlated with

those calculated based on condensed-phase structures.[20,21] The evolution of native MS and the study of protein structure in the gas-phase have been reviewed previously.[22,23] There is substantial evidence that native-like ions can retain additional properties of their condensed-phase counterparts. For example, hybrid IM, infrared action spectroscopy, and MS analysis of native-like ions of β-lactoglobulin and myoglobin yielded infrared signatures that were consistent with the expected degrees of β-sheet and helical composition in solution.[24] Additionally, ions of the endospores of *Bacillus subtilis* have been successfully cultured following high-velocity collisions with surfaces, demonstrating that protein ions from electrospray ionization can even maintain biological function.[25]

Protein ions formed from denaturing solutions (*e.g.*, organic and acidified) exhibit higher charge-state (z) and Ω values than their native-like counterparts.[26,27] Interestingly, when these high-z ions undergo charge reduction in the gas phase, the resulting charge-reduced product ions can have more compact Ω values than the initial, unreduced ions.[28–31] The extents of charge reduction that can be achieved using ion/neutral reactions are limited by the thermodynamics and kinetics of those reactions.[32] Charge-transfer reactions between cations and anions are exothermic even at low charge states[33] and can proceed through either electron-transfer (Reaction 1) or proton-transfer reactions (Reaction 2):

$$[M_n+xH]^{x+}+A\cdot^{-} \rightarrow [M_n+xH]\cdot^{(x-1)+}+A \rightarrow \text{Dissociation} \qquad \text{Reaction (1)}$$

$$[M_n+xH]^{x+}+A^{-} \rightarrow [M_n+(x-1)H]^{(x-1)+}+AH \qquad \text{Reaction (2)}$$

Electron transfer yields a radical cation, which can undergo subsequent bond cleavage and fragmentation, *i.e.*, electron-transfer dissociation (ETD).[34] Conversely, proton-transfer reactions produce even-electron products that do not spontaneously fragment, which enables analysis of charge-reduced molecular ions.[32,33]

Recently, we introduced cation-to-anion proton-transfer-reactions (CAPTR) as a method to produce many charge-reduced product ions from isolated precursor ions via Reaction 2.[35] We've developed a strategy for investigating the relationship between z, Ω, and original solution condition of proteins that uses CAPTR, IM, and MS.[30,36–38] For example, the Ω values of lysozyme ions generated

from denaturing solution conditions are larger than those generated from native-like conditions. From denaturing conditions, lysozyme ions with four intact disulfide bonds have smaller Ω values than the corresponding ions with reduced disulfide bonds.[37,39] The CAPTR products of ions from both intact and reduced denaturing conditions all exhibit smaller Ω values than the respective precursor ions. Interestingly, for CAPTR products with $z \leq 6$, the disulfide-reduced products have smaller Ω values than corresponding disulfide-intact products. At the lowest *z* measured, all product ions isomerize to structures with Ω values similar to those measured for ions from native-like conditions and calculated from the crystal structure, although small differences were observed.[37] These results indicate that the structure and dynamics of gas-phase protein ions can depend on disulfide bonding and original condensed-phase environment. Other work has shown that for large protein and protein complex ions from native-like solutions (*i.e.*, aqueous 200 mM ammonium acetate at pH 7.0), the magnitude of excess charge can have small, but statistically significant, impacts on their Ω values.[38] These findings emphasize the importance of considering charge when using IM–MS to study structure in the gas phase.[40]

Here, we use CAPTR, IM–MS, and post-CAPTR activation to characterize the structures of serum albumin ions in the gas phase. Serum albumin is a 66 kDa protein that contains 17 internal disulfide bonds and three domains. Ions were generated from multiple solution conditions that retain varying extents of the native structure. The objective of this study is to expand our understanding of the relationship between solution conditions, internal disulfide bonds, Ω, and *z* for a larger, multi-domain protein.

2.3 Methods

Sample Preparation. Bovine serum albumin, which will be referred to as 'serum albumin', was purchased from Sigma Aldrich (St. Louis, MO) and prepared to a final protein concentration of 18-20 µM in each of the five solutions that are summarized in Table 1. For native-like, disulfide-intact (NI) conditions, the protein was dissolved in aqueous 200 mM ammonium acetate at pH 7.0. For native-like,

disulfide-intact, supercharging conditions (NISC), 3% by volume sulfolane was added to the solution for NI conditions. For denatured, disulfide-intact (DI) conditions, the protein was dissolved in a 70:30 (v:v) mixture of ultrapure MilliPore water and methanol with 0.1% by volume trifluoroacetic acid. For denatured, disulfide-intact, supercharging (DISC) conditions, the protein was dissolved into an 84.5:15:0.5 (v:v) mixture of water, propylene carbonate, and glacial acetic acid. Serum albumin was also reduced and alkylated using a procedure described in the *Supporting Information* and then stored at −80° C until use. For denatured, disulfide-reduced, supercharging (DRSC) conditions, the disulfide-reduced sample was transferred using a Merck ZipTip pipette tip (Darmstadt, Germany) into a 1:1 (v:v) mixture of acetonitrile and water with 0.1% trifluoroacetic acid, to which 15% by volume propylene carbonate was added.

Table 1. Solution Conditions

	DSB Intact	**Description**	**Solvent and Additives** (by volume)	z_{min}	z_{max}
DRSC	No[a]	denaturing, supercharging	1:1 water:acetonitrile with 0.1% trifluoroacetic acid and 15% propylene carbonate	53	92
DISC	Yes	denaturing, supercharging	water with 15% propylene carbonate and 0.5% acetic acid	34	87
DI	Yes	denaturing	70:30 water:methanol with 0.2% formic acid	26	56
NISC	Yes	native-like, supercharging	aqueous 200 mM ammonium acetate at pH 7 with 3% sulfolane	15	26
NI	Yes	native-like	aqueous 200 mM ammonium acetate at pH 7	14	17

[a] Prior to preparation of the electrospray solution, the protein sample was reduced and alkylated as described in the *Supporting Information*.

All experiments were conducted on a Waters Synapt G2 HDMS equipped with a glow-discharge ionization source for ion/ion chemistry[41] and a radio-frequency (rf) confining drift cell.[42] Cations were generated using nanoelectrospray ionization from borosilicate capillaries with inner diameters of 0.78 mm pulled to an ~1-3 μm tip using a Sutter Instruments P-97 micropipette puller (Novato, CA). A platinum

wire was inserted into the wide end of the capillary to make electrical contact with the solution. The atmospheric-pressure interface was maintained at 120 °C, which has been shown to induce some heat transfer to the sample.[36] For CAPTR, perfluoro-1,3-dimethylcyclohexane (PDCH, Sigma Aldrich, St. Louis, MO) vapor[32] was introduced into the glow-discharge ionization source.[41] The $[PDCH{-}F]^-$ fragments at *m*/*z* 381 were quadrupole selected and accumulated in the trap cell for 100 ms. The polarity of the instrument was then switched to positive mode and a narrow *m*/*z* window corresponding to a single charge state of the protein was quadrupole selected and transmitted through the cloud of accumulated anions for 2 to 10 s to induce CAPTR.[35] Charge-reduced product ions and residual precursor ions were then pulsed into the mobility cell for 200 µs every 27.6 or 36.4 ms, depending on the maximum *m*/*z* measured. Representative mass spectra are shown in Figure S1.

IM arrival-time distributions were measured using an rf-confining drift cell.[42] A constant electric field of 5 V cm^{-1} was applied to the drift cell, which was filled with approximately 1.4 Torr helium or 1.2 Torr nitrogen gas. Ω values and apparent widths were determined using a method reported previously[37] and described in the *Supporting Information*. Briefly, field-dependent measurements were used to determine the *m*/*z*-dependent and *m*/*z*-independent transport times of ions from the end of the mobility cell to the entrance of the time-of-flight mass analyzer. The arrival-time distributions measured at a single field strength were corrected for these transport times and used to calculate mobility (*K*) distributions. These *K* distributions were then converted to apparent Ω distributions using the Mason-Schamp equation:[19]

$$\Omega = \frac{3ez}{16N}\left(\frac{2\pi}{\mu k_B T}\right)^{1/2}\frac{1}{K} \quad (3)$$

where *z* is the charge state, *e* is the elementary charge, *N* is the number density of the drift gas, μ is the reduced mass of the ion and the drift gas, k_B is the Boltzmann constant, and *T* is the temperature of the drift gas (301 K). For post-CAPTR activation experiments, ions were collisionally activated during injection into the mobility cell. Note that activation can induce some spontaneous loss of charge.[30]

2.4 Results and Discussion

Using serum albumin as a model, this study aims to expand our understanding of the relationship between solution conditions, internal disulfide bonds, Ω, and z for a larger, multi-domain protein. This protein was selected because many biotherapeutic also contain multiple domains and are stabilized by disulfide bonds. Serum albumin ions were generated from five conditions that retained varying degrees of the native structure and are summarized in Table 1. IM–MS of ions generated from each solution condition will be used to examine the relationship between Ω and z of the original ions from electrospray. CAPTR of selected ions from each condition will be used to build a more general understanding of the relationship of Ω and z. Finally, results from energy-dependent experiments of z = 15+ ions generated through three different pathways will be used to compare the structures and stabilities of these ions.

2.4.1 Serum Albumin Ions from Electrospray. Figure 1 shows representative mass spectra obtained from each condition. Figure S2 shows that the neutral mass of the ions from DRSC conditions is ~2 kDa heavier than those from DISC conditions, which is consistent with the reduction and alkylation of the 17 native disulfide bonds and one free cysteine for the former. The maximum and minimum charges states observed from the spectra in Figure 1 are summarized in Table 1. Note that the range of charge states exhibited in a specific mass spectrum depends to some extent on the electrospray emitter and other parameters. The magnitude and widths of the charge state distributions exhibited by the ions generally increase with the increasingly disruptive nature of the solution condition (*i.e.*, NI < NISC < DI <DISC < DRSC). Results from mass spectrometry of serum albumin from various solution conditions (although not necessarily the exact same conditions used here) have been reported previously.[43,44] The values for the highest charge states observed for ions generated from DISC and DRSC conditions are generally consistent with those results, although some lower charge states observed previously were not observed in the present experiments. The charge-state distributions observed from NI, NISC, and DI conditions are consistent with previously reported values.[44,45]

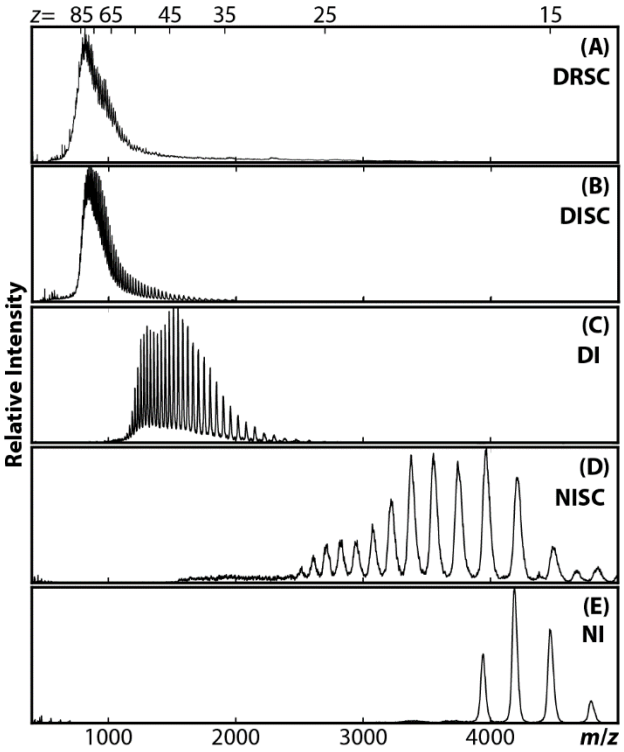

Figure 2.1. Representative mass spectra of serum albumin generated from each solution condition described in Table 1, as labeled in each panel. Values along the top axis correspond to the charge state assignments for panels B-E. Relative to the ions from the other conditions, the *m*/*z* values for the DRSC ions are shifted due to alkylation following reduction of the disulfide bonds. Note that as ions become larger and more highly charged, scattering during time-of-flight analysis becomes increasingly likely.

The mobilities of all ions were determined by measuring the time for an ion to traverse an rf-confining drift cell containing helium gas,[42] as described in the *Methods*. The arrival-time distributions were converted to median collision cross section with helium ($\tilde{\Omega}$) values as described in the *Methods* section, and the resulting values for a subset of ions from each condition are shown in Figure 2. For the ions from NI, NISC, DI, DISC, and DRSC conditions, the $\tilde{\Omega}$ values ranged from 40.2 to 41.3 nm^2, 43.6 to

56.6 nm^2, 93.0 to 109.9 nm^2, 119.3 to 129.4 nm^2, and 141.6 to 158.7 nm^2, respectively. The $\tilde{\Omega}$ values of these ions depend strongly on the original solution conditions; notably, none of the $\tilde{\Omega}$ ranges overlap. Ω values were calculated for native, α-helical, and linear models of serum albumin, as described in the *Supporting Information* and reported in Table S1. These models serve as qualitative points of comparison that are compact, extended with significant interactions between neighboring residues, and completely extended, respectively. Briefly, values measured for the NI ions are consistent with those calculated for the native model, values measured for the DRSC ions are between those calculated for the α-helical and linear models, and results for the ions from the other conditions fall between the two extremes. Additional comparisons between the experimental and calculated results are included in the *Supporting Information*. The $\tilde{\Omega}$ values from DI, NISC, and NI conditions are consistent with previous reports.[44,45] Ω_{N_2} values have been reported for serum albumin ions from conditions that are similar to the DISC and DRSC conditions used here, but directly comparing results from He- and N_2-based measurements is challenging[40,46,47] and beyond the scope of this paper.

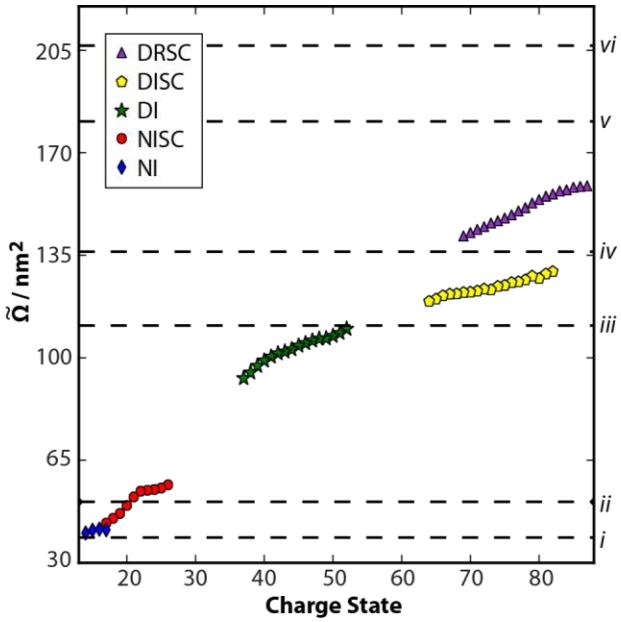

Figure 2.2. $\tilde{\Omega}$ values for a subset of the ions generated from each of the five solution conditions determined using a field-dependent method, as described in the *Supporting Information*. Note that all $\tilde{\Omega}$ values are with helium gas, unless otherwise noted. Black dashed lines correspond to Ω values calculated for the native (*i* and *ii*, for the projection approximation and exact hard sphere scattering methods, respectively), the α-helical (*iii* and *iv*), and the linear (*v* and *vi*) models of serum albumin. Details of the methods and rationale for the calculations are described in the *Supporting Information.*

The reduction of the internal disulfide bonds for the DRSC ions enables those ions to adopt more extended conformations and higher charge states than the corresponding DISC ions, consistent with previous results for lysozyme.[37,39] Most notably, the $\tilde{\Omega}$ value of the lowest-*z* ions from DRSC conditions (141.6 nm^2) is larger than the $\tilde{\Omega}$ value of the highest-*z* ions from DISC conditions (118.3 nm^2). This finding differs from that reported previously based on serum albumin ions generated from denaturing conditions with 5% by volume 1,2-butylene carbonate as the supercharging agent; there, many disulfide-

intact and disulfide-reduced ions of a given charge state exhibited similar Ω_{N_2} values.[43] The DRSC ions display an upper charge state limit of 92+, which is 5 charges more than that for the DISC ions (Figure 1). This suggests that the inherent threshold of potential charge-sites of serum albumin is not reached by the disulfide-intact ions and that the reduction of the disulfide bonds enables additional protonation that can be attributed to the exposure of previously buried titratable sites[48] and/or greater basicities.[49]

These results show that charge-state distributions and $\tilde{\Omega}$ values of serum albumin ions in the gas phase depend on the solutions from which the proteins were ionized and how these conditions influence their structures. In the following section, we will use CAPTR to probe the relationship between the charge state and $\tilde{\Omega}$ values of charge-reduced ions.

2.4.2 Cation-to-Anion Proton-Transfer Reactions (CAPTR). Selected serum albumin ions generated from each of the five solution conditions were isolated and subjected to CAPTR. These ions will be denoted by "$^{\text{Condition}}P\rightarrow C$", where "Condition" represents an abbreviation for a sample condition from Table 1, "*P"* is the charge state of the precursor cation, and "*C*" is the charge state of the CAPTR product. For example, "$^{\text{DRSC}}80\rightarrow 23$" refers to the 23+ CAPTR product from the 80+ ion generated from DRSC conditions. Representative mass spectra for the $^{\text{DRSC}}80\rightarrow C$, $^{\text{DISC}}80\rightarrow C$, $^{\text{DI}}45\rightarrow C$, $^{\text{NISC}}20\rightarrow C$, and $^{\text{NI}}17\rightarrow C$ ions are shown in Figure 3. The spectra all exhibit peaks originating from a long series of CAPTR products. The relative intensities of the CAPTR products depend on experimental conditions, which has been investigated previously.[35] Peaks for *C* of at least 10 were observed for the products of ions from DRSC, DISC, and DI conditions, and peaks for *C* of at least 6 were observed for the products of ions from NISC and NI conditions. Differences in the lowest value of *C* observed for ions originating from different conditions can be attributed to the especially low mobilities of some ions and their inefficient transfer into the drift cell.

For each condition, CAPTR products originating from one to four precursor ion charge states were analyzed using IM–MS. We will first discuss general trends in the $\tilde{\Omega}$ values for the $P\rightarrow C$ ions from a given condition, and then compare results for different conditions. Figure 4A shows that the $\tilde{\Omega}$ values

for the $^{DRSC}70 \rightarrow C$ and $^{DRSC}80 \rightarrow C$ ions depend weakly on P and decrease monotonically with decreasing C (Figure 4A). Figure 4B shows that the $\tilde{\Omega}$ values for the $^{DISC}P \rightarrow C$, P = 50, 60, 70, and 80, ions also depend weakly on P and decrease monotonically with decreasing C. Although the $\tilde{\Omega}$ values for the $^{DI}45 \rightarrow C$ ions generally decrease with decreasing C, the values for $C \approx 35$ to 40 are all similar and interrupt the monotonic decrease in $\tilde{\Omega}$ with decreasing C observed for higher and lower values of C (Figure 4C). The $\tilde{\Omega}$ values for the $^{NISC}P \rightarrow C$, P = 19 to 21, ions exhibit a large decrease after the first CAPTR event and smaller decreases for the subsequent CAPTR events, whereas the values for all $^{NISC}18 \rightarrow C$ ions are similar to each other (Figure 4D). The $\tilde{\Omega}$ values for the $^{NISC}P \rightarrow C$ ions of a given C increase slightly with P, *e.g.*, the $^{NISC}P \rightarrow 14$ ions have $\tilde{\Omega}$ values of 45.3, 44.1, 43.0 and 42.2 nm^2 for P = 21, 20, 19, and 18, respectively. However, the values for all $^{NISC}P \rightarrow 6$ ions differ by less than 2.5 nm^2. Finally, the $\tilde{\Omega}$ values for the $^{NI}P \rightarrow C$, P = 15 to 17, ions are similar to each other, as well as values reported previously for the CAPTR products of these ions[38] and to values reported previously for native-like serum albumin without charge reduction (Figure 4D).[45,50] These results for the ions from NI conditions are consistent with our previous claim that the excess charges present on the native-like ions of large proteins can have a modest effect on their $\tilde{\Omega}$ values.

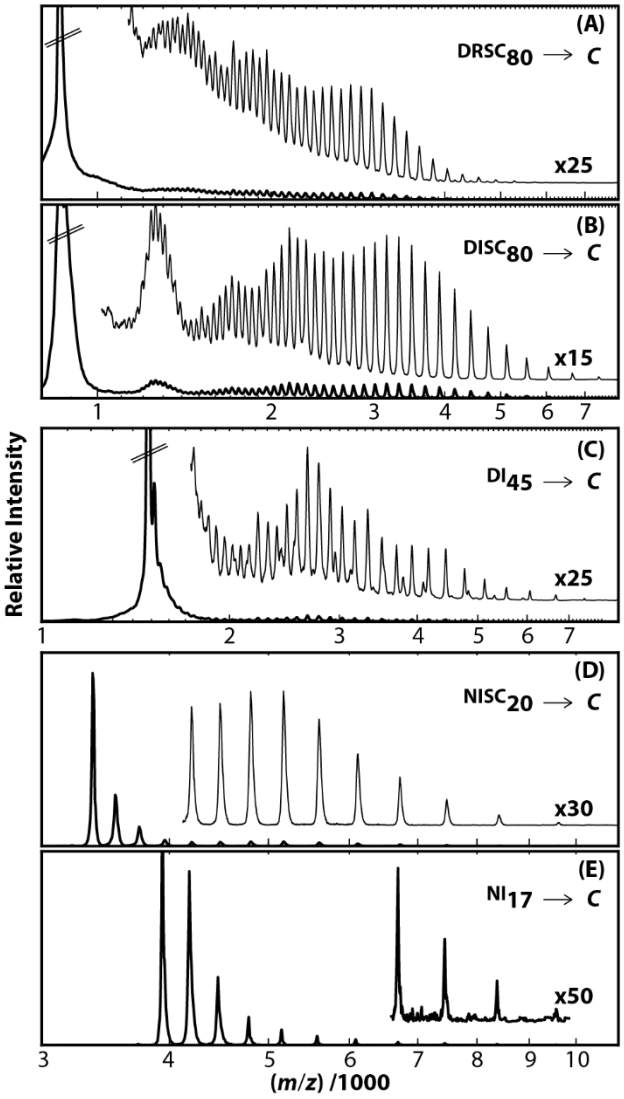

Figure 2.3. CAPTR mass spectra of the $^{DRSC}80 \rightarrow C$, $^{DISC}80 \rightarrow C$, $^{DI}45 \rightarrow C$, $^{NISC}20 \rightarrow C$, and $^{NI}17 \rightarrow C$ ions. The identities of ions are indicated by "$^{Condition}P \rightarrow C$", where "Condition" is an abbreviation from Table 1, "*P*" is the charge state of the precursor cation, and "*C*" is the charge state of the CAPTR product. Selected regions of each spectrum have been amplified as indicated and offset from the horizontal axis to aid in visualization.

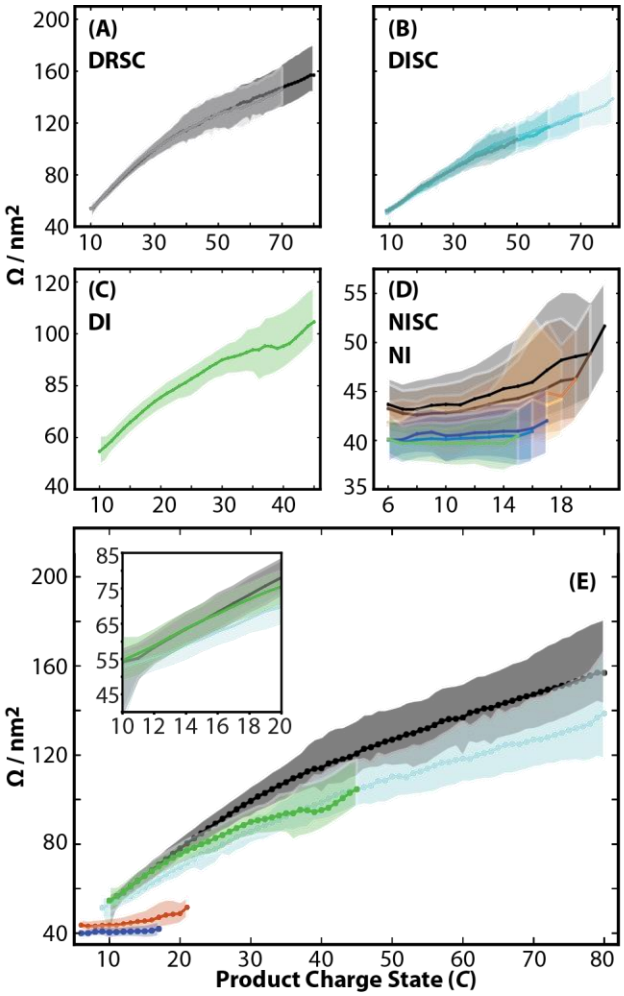

Figure 2.4. Results from IM–MS of the CAPTR products. Markers correspond to the $\tilde{\Omega}$ values and the shaded regions span from 10% to 90% of the cumulative distribution function of each apparent Ω distribution, as described in the *Supporting Information*. Results for (A) the $^{DRSC}P \rightarrow C$, P = 70 and 80, ions, (B) the $^{DISC}P \rightarrow C$, P = 50, 60, 70, and 80, ions, (C) the $^{DI}45 \rightarrow C$ ions, and (D) the $^{NISC}P \rightarrow C$, P = 18 to 21 (*copper tones*), and the $^{NI}P \rightarrow C$, P = 15 to 17 (*cool tones*), ions. (E) Summary of results for the highest P from each solution condition, *i.e.*, the $^{DRSC}80 \rightarrow C$, $^{DISC}80 \rightarrow C$, $^{DI}45 \rightarrow C$, $^{NISC}21 \rightarrow C$, and $^{NI}17 \rightarrow C$ ions. The

inset of E shows the results for $^{DRSC}80\rightarrow C$, $^{DISC}80\rightarrow C$, $^{DI}45\rightarrow C$ ions for $20 \geq C \geq 10$.

To aid in the direct comparison of results for ions from different conditions, Figure 4E shows the $\tilde{\Omega}$ values of the $^{DRSC}80\rightarrow C$, $^{DISC}80\rightarrow C$, $^{DI}45\rightarrow C$, $^{NISC}21\rightarrow C$, and $^{NI}17\rightarrow C$ ions. For each C, the $\tilde{\Omega}$ values for the ions from denaturing conditions are systematically larger than those for the $^{NISC}21\rightarrow C$ ions, which in turn are systematically larger than those for the $^{NI}17\rightarrow C$ ions. Among the ions from denaturing conditions, the $\tilde{\Omega}$ values of the $^{DISC}80\rightarrow C$ and $^{DI}45\rightarrow C$ ions for each C are similar to each other, except for the small difference for $C \approx 35$ to 40. By comparison, the $\tilde{\Omega}$ values of the $^{DRSC}80\rightarrow C$ are ~20 nm^2 larger for ions of large C, but those differences decrease with decreasing C. The $\tilde{\Omega}$ values from $^{DI}45\rightarrow C$, $^{DISC}80\rightarrow C$, and $^{DRSC}80\rightarrow C$ for $20 \geq C \geq 10$ ions is shown in the inset of Figure 4E, which shows that despite the decreasing differences in $\tilde{\Omega}$ values, there are still subtle differences over this range. This suggests that these ions are still sensitive to the condensed-phase environment from which their precursor ions were generated.

The lowest-C products observed from each condition, *i.e.*, the $^{DRSC}80\rightarrow 10$, $^{DISC}80\rightarrow 9$, $^{DI}45\rightarrow 10$, $^{NISC}21\rightarrow 6$, and $^{NI}17\rightarrow 6$ ion, have $\tilde{\Omega}$ values that are 66%, 61%, 50%, 15%, and 6% smaller than the values for the corresponding precursor ions, respectively. The maximum relative decreases for the CAPTR products from each of the three denaturing conditions are similar to the maximum relative decrease of 50% for $13\rightarrow 3$ ions of ubiquitin from denaturing conditions,[30] of 55% for $18\rightarrow 3$ ions of cytochrome *c* from denaturing conditions,[36] and of 57% for $19\rightarrow 3$ ions of lysozyme from denatured, disulfide-reduced conditions.[37] However, despite the large decreases in $\tilde{\Omega}$ values for the CAPTR products from each of the three denaturing conditions, the values for the $^{DRSC}80\rightarrow 10$, $^{DISC}80\rightarrow 9$, and $^{DI}45\rightarrow 10$ ions are all about 30% larger than those for all $^{NI}P\rightarrow C$ ions. The comparatively small maximum relative decrease for the $^{NI}17\rightarrow 6$ ions is consistent with the small relative decreases reported for ions of cytochrome *c*,[36] lysozyme,[37] serum albumin, streptavidin tetramer, avidin tetramer, and alcohol dehydrogenase tetramer[38]

from native-like conditions. Therefore, these results provide further support that the Ω values of native-like ions can depend only weakly on their charge state.

Although the $\tilde{\Omega}$ values of the $^{DRSC}P\rightarrow C$ ions are systematically larger than those of the corresponding $^{DISC}P\rightarrow C$ ions for high values of C, those values converge with decreasing C (Figure 4E). Therefore, the change in $\tilde{\Omega}$ values associated with each CAPTR event must be different for the ions generated from the two conditions. Figure 5 shows that for $C \geq 36$, the $\tilde{\Omega}$ values of the $^{DRSC}P\rightarrow C$ and $^{DISC}P\rightarrow C$ ions decrease on average by 1.03 and 0.95 nm^2, respectively, per CAPTR event. Both the $^{DRSC}P\rightarrow C$ and $^{DISC}P\rightarrow C$ ions exhibit greater decreases in $\tilde{\Omega}$ per CAPTR event for $C < 36$, but the average decrease for the $^{DRSC}P\rightarrow C$ ions is far greater (~2.2 nm^2 per event) than that for the $^{DISC}P\rightarrow C$ ions (~1.5 nm^2 per event). For comparison, lysozyme ions from denatured, disulfide-reduced conditions exhibit a greater decrease in $\tilde{\Omega}$ per CAPTR event than lysozyme ions from denatured, disulfide-intact conditions;[37] the magnitude of the decreases in $\tilde{\Omega}$ per CAPTR event did not converge for the high-C ions from the two conditions. These results all suggest that the presence of disulfide bonds creates additional constraints to protein ions adopting more extended structures with increasing z and refolding to more compact structures in response to CAPTR.

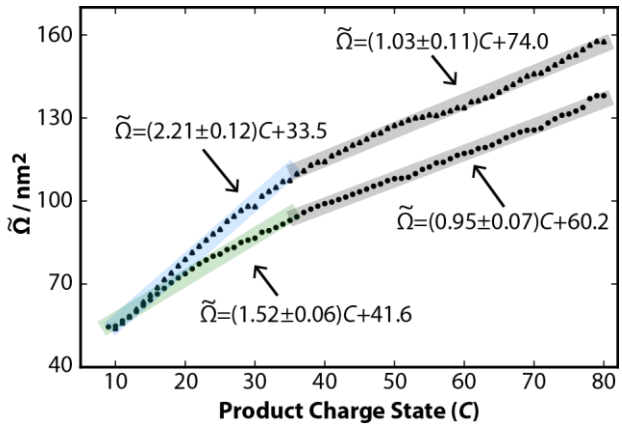

Figure 2.5. $\tilde{\Omega}$ values of the $^{DISC}P\rightarrow C$ (*circles*, average of results for P = 50, 60, 70, and 80) and $^{DRSC}P\rightarrow C$ (*triangles*, average of results for P = 80 and 70), as a function of C. The transparent lines correspond to the line of best-fit and spans the range of C used for the linear regression. Although the $\tilde{\Omega}$ values for the $^{DRSC}P\rightarrow C$ ions are systematically larger than the corresponding $^{DISC}P\rightarrow C$ ions, both exhibit similar changes in $\tilde{\Omega}$ per CAPTR event for $C \geq 36$ (~1.0 nm^2 per event, *gray lines*). In contrast, for $C < 36$ the change in $\tilde{\Omega}$ per CAPTR event for the $^{DRSC}P\rightarrow C$ ions is far greater (~2.2 nm^2 per event, *cyan line*) than that for the $^{DISC}P\rightarrow C$ ions (~1.5 nm^2 per event, *green line*).

Relative to NI conditions, ions from NISC conditions are generated from solutions that also contain 3% by volume sulfolane. The ions generated from NISC conditions exhibit higher charge states, larger $\tilde{\Omega}$ values, and $\tilde{\Omega}$ values that depend more strongly on z relative to those generated from NI conditions (Figures 1D, 1E, and 2). Furthermore, the $\tilde{\Omega}$ values for the $^{NISC}21\rightarrow C$ ions of a given C are systematically larger than those of the corresponding $^{NI}17\rightarrow C$ ions. Therefore, these results indicate that the addition of sulfolane results in structural changes that are concomitant with supercharging and that those changes are not reversed by charge reduction. In contrast, CAPTR of collisionally activated serum albumin ions from native-like conditions has been observed to result in ions with $\tilde{\Omega}$ values that are similar

to those of serum albumin ions from native-like conditions that had undergone minimal activation; thus CAPTR appears to mitigate some structural changes associated with collisional activation.[38] These findings therefore support conclusions by Williams and coworkers that supercharging can disrupt the native structures of proteins and protein complexes.[51]

In addition to the $\tilde{\Omega}$ values, Figure 4 also includes two other critical values from the apparent Ω distribution, *i.e.*, 10% and 90% of the cumulative distribution function of the apparent Ω distribution as described in the *Supporting Information*. For CAPTR products of a given *C* and solution condition, all three critical values appear to be largely independent of *P*. Note that apparent Ω distributions include contributions from gating at the beginning of and diffusion during separations,[42,52] which will be different for ions of different *z*. However, all three critical values of ions of a given *z* should be directly comparable. Quantifying these contributions and the underlying structural heterogeneity will be the subject of future studies.

These results show that the structures of CAPTR products depend on the condition from which the precursor ion was generated, the value of *C*, and to a lesser extent, the value of *P*. In the next section, we will use energy-dependent experiments to probe the potential-energy landscape for select ions to build on the relationship between Ω and *z* and potential contributions from kinetic trapping.

2.4.3 Conformational Landscapes of 15+ Serum Albumin. This study demonstrates that protein ions of a given charge state can be formed through multiple experimental schemes, including generation from different conditions and charge reduction via different numbers of CAPTR events. To investigate the relationship between 15+ serum albumin ions formed using three schemes, we will monitor the mobilities of these ions as a function of the injection voltage used to transfer the ions into a drift cell containing 1.2 Torr nitrogen gas. Energy deposition in these experiments will be less efficient than injection into a lower pressure, argon-filled collision cell, as used for collision-induced unfolding,[53] but more efficient than injection into a helium-filled drift cell, which occurs inadvertently in the preceding IM experiments. In this discussion, an "*" will be used to indicate the species that was activated in the

experiment, *e.g.*, "$^{DISC}60\rightarrow15^{*}$" indicates that the 15+ CAPTR product was activated during injection into the drift cell.

The structures and stabilities of the $^{NI}15^{*}$, $^{DRSC}70\rightarrow15^{*}$, and $^{DISC}60\rightarrow15^{*}$ ions were each probed using this strategy. The apparent Ω_{N_2} distributions of these ions are shown in Figure 6A and the $\widetilde{\Omega}_{N_2}$ values of those distributions are plotted in Figure 6B. At the lowest injection voltage, the $\widetilde{\Omega}_{N_2}$ values of the $^{DRSC}70\rightarrow15^{*}$ and $^{DISC}60\rightarrow15^{*}$ ions are similar to each other (~64 nm^2) and much larger than that for the $^{NI}15^{*}$ ions (~44 nm^2). This finding is consistent with the data in Figure 4, which were acquired with minimal activation. However, the $\widetilde{\Omega}_{N_2}$ values in Figure 6 are systematically larger than the $\widetilde{\Omega}_{He}$ values in Figure 4, which is consistent with Ω being a property of the ion-neutral pair as discussed elsewhere.[40,46,50,54] With increasing injection voltage, the $\widetilde{\Omega}_{N_2}$ values of the $^{DRSC}70\rightarrow15^{*}$ and $^{DISC}60\rightarrow15^{*}$ ions both increase to ~68 nm^2 and then decrease to values smaller than those for the ions at low energy. In contrast, the $\widetilde{\Omega}_{N_2}$ values of the $^{NI}15^{*}$ ions increase with increasing injection voltage over all energies.

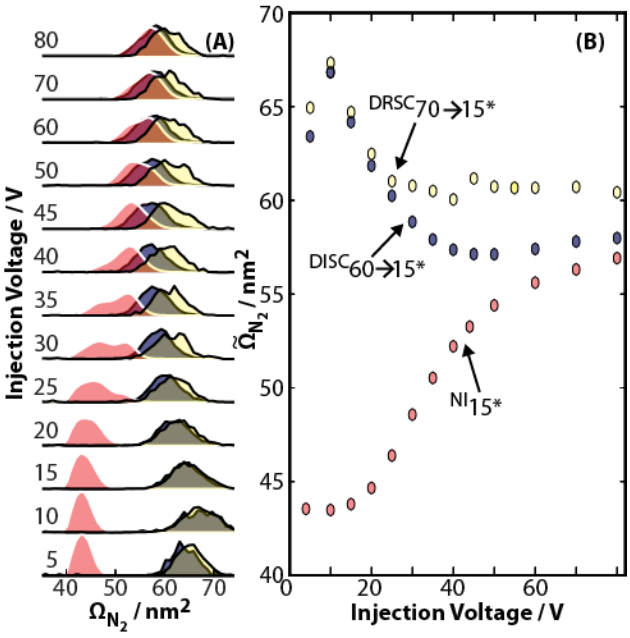

Figure 2.6. (A) Apparent Ω_{N_2} distributions of the $^{NI}15^*$ (*magenta*), $^{DISC}60\rightarrow15^*$ (*purple*), and $^{DISC}70\rightarrow15^*$ (*yellow*) ions as a function of the injection voltage used to transfer the ions into a drift cell containing 1.2 Torr nitrogen gas. (B) $\tilde{\Omega}_{N_2}$ values of the distributions in panel A as a function of the injection voltage.

At the highest energies, the apparent Ω_{N_2} distributions and the corresponding $\tilde{\Omega}_{N_2}$ values for the $^{NI}15^*$, $^{DRSC}70\rightarrow15^*$, and $^{DISC}60\rightarrow15^*$ ions each appear to have largely converged and no longer depend strongly on further increases in the injection voltage. This result is consistent with each of these ions adopting a quasi-equilibrium of structures, *i.e.*, the relative population of structures depends of the relative free energies of those structures after thermalization.[30,55] The quasi-equilibrium distributions of these ions exhibit significant overlap, which suggests that these ions may share many structural motifs and are populating similar regions of their potential- energy surfaces. However, it is also possible that that these ions have isomerized to different structures that coincidently have similar mobility distributions. For example, the quasi-equilibrium Ω_{N_2} distributions of the $^{NI}15^*$ and $^{DISC}60\rightarrow15^*$ ions are similar to each

other and shifted to slightly smaller values than that for the $^{DRSC}70\rightarrow15^*$ ions. This suggests that the presence of intact disulfide bonds may preferentially favor slightly more compact structures in the gas phase, even for low-*z* ions after considerable annealing.

These results indicate that the initial structures of the $^{NI}15$, $^{DRSC}70\rightarrow15$, and $^{DISC}60\rightarrow15$ ions, *i.e.*, those present during their accumulation prior to IM, are the result of kinetic trapping and memory of their prior structures. For example, the increase in the $\widetilde{\Omega}_{N_2}$ values with increasing energy for the $^{NI}15^*$ ions can be attributed to the ions overcoming isomerization barriers to more extended structures that minimize Coulombic repulsion between the excess charges, likely at the expense of other intramolecular interactions that were present in the initial, kinetically trapped structure. In contrast, the decrease in the $\widetilde{\Omega}_{N_2}$ values with increasing energy for the $^{DRSC}70\rightarrow15^*$ and $^{DISC}60\rightarrow15^*$ ions can be attributed to the ions overcoming isomerization barriers to more compact structures that include more favorable intramolecular interactions that were not present in the initial structures adopted after CAPTR of the highly charged precursor ions. Therefore, activation of these ions from very different conditions may enable access to similar regions of the potential energy landscape. These results complement a growing body of literature reporting that although many elements of condensed-phase structure can be preserved in the gas phase,[24] fidelity is the result of kinetic trapping and gas-phase protein ions at equilibrium may have vastly different structures.[56,57]

2.5 Conclusions

These experiments used CAPTR, IM, and post-CAPTR activation to explore the relationship between the $\tilde{\Omega}$ and *z* values of serum albumin ions generated from five conditions that retain varying degrees of the native structure (Table 1). Ions generated from increasingly disruptive conditions exhibited higher charge states and larger $\tilde{\Omega}$ values (Figures 1 and 2). CAPTR of selected precursor ions from each condition showed that the $\tilde{\Omega}$ values of the product ions depend on the original solution conditions, and to varying extents, the charge state of the product and precursor ions. The $\tilde{\Omega}$ values of the CAPTR products

of the ions from NISC conditions are systematically larger than those from NI conditions, and both depend weakly on *C* (Figure 4D). At high *C*, the $\tilde{\Omega}$ values of the CAPTR products of the ions generated from DRSC, DISC, and DI conditions depend strongly on both *C* and the presence of disulfide bonds (Figure 4). With decreasing *C*, the differences between the $\tilde{\Omega}$ values of the disulfide-intact and disulfide-reduced ions from these conditions decrease (Figure 4E), although small differences are still observed (Figure 4E, inset). This is a consequence of the change in the $\tilde{\Omega}$ value per CAPTR event being greater for the $^{DRSC}P \rightarrow C$ ions (2.2 nm^2) than for the $^{DISC}P \rightarrow C$ ions (1.5 nm^2) for $C < 36$, even though both ions exhibit an ~1.0 nm^2 decrease in $\tilde{\Omega}$ values per CAPTR event for larger *C* (Figure 5). More generally, these results are consistent with disulfide bonds preventing extension to larger structures at high *z,* as well as preventing isomerization to more compact structures at low *z*.

The stability of 15+ ions produced from three different origins was examined using post-CAPTR activation of the $^{DRSC}70 \rightarrow 15^*$, $^{DISC}60 \rightarrow 15^*$, and $^{NI}15^*$ ions. At low injection voltages, the denatured ions have $\tilde{\Omega}$ values that are significantly larger than those for the native-like ion. At high injection voltages, the three ions have converged to Ω distributions that have significant overlap, especially for the $^{DISC}60 \rightarrow 15^*$ and $^{NI}15^*$ ions. This is consistent with these ions sharing structural motifs and accessing similar regions of the potential-energy surface. Additionally, the $\tilde{\Omega}$ value of the $^{DRSC}70 \rightarrow 15^*$ and $^{DISC}60 \rightarrow 15^*$ ions becomes largely independent of the injection voltage above 45 V, consistent with these ions adopting a quasi-equilibrium of structures.

These results provided new insights into the relationship between the structures, charge states, and solution conditions of a large, multi-domain protein in the gas phase. Whereas the $\tilde{\Omega}$ values of low-*z* CAPTR products of small proteins from denaturing conditions are similar to those for the corresponding native-like ions, the low-*z* CAPTR products of serum albumin are at least 30% larger than those for the native-like ions of serum albumin. This large difference can be understood in the context of the energy-dependent experiments. Relative to the structures formed after significant annealing, the CAPTR products of the ions from denaturing conditions have significantly larger $\tilde{\Omega}$ values and the ions from native-like

conditions have significantly smaller $\tilde{\Omega}$ values (Figure 6). Together, these results show that the structures of the original ions from electrospray ionization and their CAPTR products all depend strongly on the original solution condition and are a consequence of kinetic trapping. Therefore, CAPTR and energy-dependent IM provide many complementary probes that are sensitive to the higher-order structures and disulfide bonding of proteins, which may be useful for biotherapeutic characterization.

2.6 Supporting Information. Supporting Information Available: This material is available free of charge via the Internet at http://pubs.acs.org.

> Protocol for reduction/alkylation of cysteine residues, determination of Ω values from arrival-time distributions, calculation of Ω values for models of serum albumin and comparison to experimental Ω values, Table S1, Figure S1, and Figure S2

2.7 Acknowledgments

This material is based upon work supported by the National Science Foundation under CHE–1807382 (M. F. B.).

2.8 References

(1) Fersht, A. R. From the First Protein Structures to Our Current Knowledge of Protein Folding: Delights and Scepticisms. *Nat. Rev. Mol. Cell Biol.* **2008**, *9*, 650–654.
(2) Carter, P. J. Introduction to Current and Future Protein Therapeutics: A Protein Engineering Perspective. *Exp. Cell Res.* **2011**, *317*, 1261–1269.
(3) Bale, J. B.; Gonen, S.; Liu, Y.; Sheffler, W.; Ellis, D.; Thomas, C.; Cascio, D.; Yeates, T. O.; Gonen, T.; King, N. P.; et al. Accurate Design of Megadalton-Scale Two-Component Icosahedral Protein Complexes. *Science* **2016**, *353*, 389–394.
(4) Hsia, Y.; Bale, J. B.; Gonen, S.; Shi, D.; Sheffler, W.; Fong, K. K.; Nattermann, U.; Xu, C.; Huang, P.-S.; Ravichandran, R.; et al. Design of a Hyperstable 60-Subunit Protein Icosahedron. *Nature* **2016**, *535*, 136–139.
(5) Brange, J.; Ribel, U.; Hansen, J. F.; Dodson, G.; Hansen, M. T.; Havelund, S.; Melberg, S. G.; Norris, F.; Norris, K.; Snel, L.; et al. Monomeric Insulins Obtained by Protein Engineering and Their Medical Implications. *Nature* **1988**, *333*, 679-682.
(6) Walsh, G.; Jefferis, R. Post-Translational Modifications in the Context of Therapeutic Proteins. *Nat. Biotechnol.* **2006**, *24*, 1241-1252.
(7) Walsh, G. Protein Engineering: Case Studies of Commercialized Engineered Products. *Biochem. Mol. Biol. Educ.* **2007**, *35*, 2–8.
(8) Pastore, A. New Challenges in Structural Biology: Catching the Complexity of Dynamic Nanomachines. *Front. Mol. Biosci.* **2014**, *1*, doi:10.3389/fmolb.2014.00003
(9) Rosati, S.; Yang, Y.; Barendregt, A.; Heck, A. J. R. Detailed Mass Analysis of Structural Heterogeneity in Monoclonal Antibodies Using Native Mass Spectrometry. *Nat. Protoc.* **2014**, *9*, 967–976.

(10) Slabinski, L.; Jaroszewski, L.; Rodrigues, A. P. C.; Rychlewski, L.; Wilson, I. A.; Lesley, S. A.; Godzik, A. The Challenge of Protein Structure Determination—lessons from Structural Genomics. *Protein Sci.* **2007**, *16*, 2472–2482.
(11) Liko, I.; Allison, T. M.; Hopper, J. T.; Robinson, C. V. Mass Spectrometry Guided Structural Biology. *Curr. Opin. Struct. Biol.* **2016**, *40*, 136–144.
(12) Beavis, R. C.; Chait, B. T. High-Accuracy Molecular Mass Determination of Proteins Using Matrix-Assisted Laser Desorption Mass Spectrometry. *Anal. Chem.* **1990**, *62*, 1836–1840.
(13) Olsen, J. V.; de Godoy, L. M. F.; Li, G.; Macek, B.; Mortensen, P.; Pesch, R.; Makarov, A.; Lange, O.; Horning, S.; Mann, M. Parts per Million Mass Accuracy on an Orbitrap Mass Spectrometer via Lock Mass Injection into a C-Trap. *Mol Cell Proteomics* **2005**, *4*, 2010–2021.
(14) Taverner, T.; Hernández, H.; Sharon, M.; Ruotolo, B. T.; Matak-Vinković, D.; Devos, D.; Russell, R. B.; Robinson, C. V. Subunit Architecture of Intact Protein Complexes from Mass Spectrometry and Homology Modeling. *Acc. Chem. Res.* **2008**, *41*, 617–627.
(15) Gahoual, R.; Heidenreich, A.-K.; Somsen, G. W.; Bulau, P.; Reusch, D.; Wuhrer, M.; Haberger, M. Detailed Characterization of Monoclonal Antibody Receptor Interaction Using Affinity Liquid Chromatography Hyphenated to Native Mass Spectrometry. *Anal. Chem.* **2017**, *89*, 5404–5412.
(16) Hernández, H.; Robinson, C. V. Determining the Stoichiometry and Interactions of Macromolecular Assemblies from Mass Spectrometry. *Nat. Protoc.* **2007**, *2*, 715–726.
(17) Aquilina, J. A.; Benesch, J. L. P.; Bateman, O. A.; Slingsby, C.; Robinson, C. V. Polydispersity of a Mammalian Chaperone: Mass Spectrometry Reveals the Population of Oligomers in αB-Crystallin. *Proc. Natl. Acad. Sci.* **2003**, *100*, 10611–10616.
(18) Lanucara, F.; Holman, S. W.; Gray, C. J.; Eyers, C. E. The Power of Ion Mobility-Mass Spectrometry for Structural Characterization and the Study of Conformational Dynamics. *Nat. Chem.* **2014**, *6*, 281–294.
(19) Gabelica, V.; Marklund, E. Fundamentals of Ion Mobility Spectrometry. *Curr. Opin. Chem. Biol.* **2018**, *42*, 51–59.
(20) Loo, J. A.; Berhane, B.; Kaddis, C. S.; Wooding, K. M.; Xie, Y.; Kaufman, S. L.; Chernushevich, I. V. Electrospray Ionization Mass Spectrometry and Ion Mobility Analysis of the 20S Proteasome Complex. *J. Am. Soc. Mass Spectrom.* **2005**, *16*, 998–1008.
(21) Hall, Z.; Politis, A.; Robinson, C. V. Structural Modeling of Heteromeric Protein Complexes from Disassembly Pathways and Ion Mobility-Mass Spectrometry. *Structure* **2012**, *20*, 1596–1609.
(22) Heck, A. J. R. Native Mass Spectrometry: A Bridge between Interactomics and Structural Biology. *Nat. Methods* **2008**, *5*, 927–933.
(23) Meyer, T.; Gabelica, V.; Grubmüller, H.; Orozco, M. Proteins in the Gas Phase. *Wiley Interdiscip. Rev. Comput. Mol. Sci.* **2013**, *3*, 408–425.
(24) Seo, J.; Hoffmann, W.; Warnke, S.; Bowers, M. T.; Pagel, K.; von Helden, G. Retention of Native Protein Structures in the Absence of Solvent: A Coupled Ion Mobility and Spectroscopic Study. *Angew. Chem. Int.* **2016**, *55*, 14173–14176.
(25) Barney, B. L.; Pratt, S. N.; Austin, D. E. Survivability of Bare, Individual Bacillus Subtilis Spores to High-Velocity Surface Impact: Implications for Microbial Transfer through Space. *Planet. Space Sci.* **2016**, *125*, 20–26.
(26) Bohrer, B. C.; Merenbloom, S. I.; Koeniger, S. L.; Hilderbrand, A. E.; Clemmer, D. E. Biomolecule Analysis by Ion Mobility Spectrometry. *Annu. Rev. Anal. Chem.* **2008**, *1*, 293–327.
(27) Wyttenbach, T.; Bowers, M. T. Structural Stability from Solution to the Gas Phase: Native Solution Structure of Ubiquitin Survives Analysis in a Solvent-Free Ion Mobility–Mass Spectrometry Environment. *J. Phys. Chem. B* **2011**, *115*, 12266–12275.
(28) Jarrold, M. F. Unfolding, Refolding, and Hydration of Proteins in the Gas Phase. *Acc. Chem. Res.* **1999**, *32*, 360–367.

(29) Zhao, Q.; Schieffer, G. M.; Soyk, M. W.; Anderson, T. J.; Houk, R. S.; Badman, E. R. Effects of Ion/ion Proton Transfer Reactions on Conformation of Gas-Phase Cytochrome c Ions. *J. Am. Soc. Mass Spectrom.* **2010**, *21*, 1208–1217.

(30) Laszlo, K. J.; Munger, E. B.; Bush, M. F. Folding of Protein Ions in the Gas Phase after Cation-to-Anion Proton-Transfer Reactions. *J. Am. Chem. Soc.* **2016**, *138*, 9581–9588.

(31) Lermyte, F.; Łącki, M. K.; Valkenborg, D.; Gambin, A.; Sobott, F. Conformational Space and Stability of ETD Charge Reduction Products of Ubiquitin. *J. Am. Soc. Mass Spectrom.* **2017**, *28*, 69–76.

(32) McLuckey, S. A.; Stephenson, J. L. Ion/ion Chemistry of High-Mass Multiply Charged Ions. *Mass Spectrom. Rev.* **1998**, *17*, 369–407.

(33) McLuckey, S. A.; Huang, T.-Y. Ion/Ion Reactions: New Chemistry for Analytical MS. *Anal. Chem.* **2009**, *81*, 8669–8676.

(34) Lermyte, F.; Konijnenberg, A.; Williams, J. P.; Brown, J. M.; Valkenborg, D.; Sobott, F. ETD Allows for Native Surface Mapping of a 150 kDa Noncovalent Complex on a Commercial Q-TWIMS-TOF Instrument. *J. Am. Soc. Mass Spectrom.* **2014**, *25*, 343–350.

(35) Laszlo, K. J.; Bush, M. F. Analysis of Native-Like Proteins and Protein Complexes Using Cation to Anion Proton Transfer Reactions (CAPTR). *J. Am. Soc. Mass Spectrom.* **2015**, *26*, 2152–2161.

(36) Laszlo, K. J.; Buckner, J. H.; Munger, E. B.; Bush, M. F. Native-Like and Denatured Cytochrome *c* Ions Yield Cation-to-Anion Proton Transfer Reaction Products with Similar Collision Cross-Sections. *J. Am. Soc. Mass Spectrom.* **2017**, *28*, 1382–1391.

(37) Laszlo, K. J.; Munger, E. B.; Bush, M. F. Effects of Solution Structure on the Folding of Lysozyme Ions in the Gas Phase. *J. Phys. Chem. B* **2017**, *121*, 2759–2766.

(38) Laszlo, K. J.; Bush, M. F. Interpreting the Collision Cross Sections of Native-like Protein Ions: Insights from Cation-to-Anion Proton-Transfer Reactions. *Anal. Chem.* **2017**, *89*, 7607–7614.

(39) Valentine, S. J.; Anderson, J. G.; Ellington, A. D.; Clemmer, D. E. Disulfide-Intact and -Reduced Lysozyme in the Gas Phase: Conformations and Pathways of Folding and Unfolding. *J. Phys. Chem. B* **1997**, *101*, 3891–3900.

(40) Canzani, D.; Laszlo, K. J.; Bush, M. F. Ion Mobility of Proteins in Nitrogen Gas: Effects of Charge State, Charge Distribution, and Structure. *J. Phys. Chem. A* **2018**, *122*, 5625-5634.

(41) Williams, J. P.; Brown, J. M.; Campuzano, I.; Sadler, P. J. Identifying Drug Metallation Sites on Peptides Using Electron Transfer Dissociation (ETD), Collision Induced Dissociation (CID) and Ion Mobility-Mass Spectrometry (IM-MS). *Chem. Commun.* **2010**, *46*, 5458–5460.

(42) Allen, S. J.; Giles, K.; Gilbert, T.; Bush, M. F. Ion Mobility Mass Spectrometry of Peptide, Protein, and Protein Complex Ions Using a Radio-Frequency Confining Drift Cell. *Analyst* **2016**, *141*, 884–891.

(43) Donor, M. T.; Ewing, S. A.; Zenaidee, M. A.; Donald, W. A.; Prell, J. S. Extended Protein Ions Are Formed by the Chain Ejection Model in Chemical Supercharging Electrospray Ionization. *Anal. Chem.* **2017**, *89*, 5107–5114.

(44) Allen, S. J. Development of Ion Mobility Mass Spectrometry Instrumentation to Investigate the Gas-Phase Structures of Protein and Protein Complex Ions. Thesis, 2017.

(45) Allen, S. J.; Schwartz, A. M.; Bush, M. F. Effects of Polarity on the Structures and Charge States of Native-like Proteins and Protein Complexes in the Gas Phase. *Anal. Chem.* **2013**, *85*, 12055–12061.

(46) Bleiholder, C.; Johnson, N. R.; Contreras, S.; Wyttenbach, T.; Bowers, M. T. Molecular Structures and Ion Mobility Cross Sections: Analysis of the Effects of He and N2 Buffer Gas. *Anal. Chem.* **2015**, *87*, 7196–7203.

(47) May, J. C.; Goodwin, C. R.; Lareau, N. M.; Leaptrot, K. L.; Morris, C. B.; Kurulugama, R. T.; Mordehai, A.; Klein, C.; Barry, W.; Darland, E.; et al. Conformational Ordering of Biomolecules in the Gas Phase: Nitrogen Collision Cross Sections Measured on a Prototype High Resolution Drift Tube Ion Mobility-Mass Spectrometer. *Anal. Chem.* **2014**, *86*, 2107–2116.

(48) Loo, R. R. O.; Lakshmanan, R.; Loo, J. A. What Protein Charging (and Supercharging) Reveal about the Mechanism of Electrospray Ionization. *J. Am. Soc. Mass Spectrom.* **2014**, *25*, 1675–1693.
(49) Zenaidee, M. A.; Leeming, M. G.; Zhang, F.; Funston, T. T.; Donald, W. A. Highly Charged Protein Ions: The Strongest Organic Acids to Date. *Angew. Chem. Int. Ed.* **2017**, *56*, 8522–8526.
(50) Bush, M. F.; Hall, Z.; Giles, K.; Hoyes, J.; Robinson, C. V.; Ruotolo, B. T. Collision Cross Sections of Proteins and Their Complexes: A Calibration Framework and Database for Gas-Phase Structural Biology. *Anal. Chem.* **2010**, *82*, 9557–9565.
(51) Sterling, H. J.; Prell, J. S.; Cassou, C. A.; Williams, E. R. Protein Conformation and Supercharging with DMSO from Aqueous Solution. *J. Am. Soc. Mass Spectrom.* **2011**, *22*, 1178–1186.
(52) Davidson, K. L.; Bush, M. F. Effects of Drift Gas Selection on the Ambient-Temperature, Ion Mobility Mass Spectrometry Analysis of Amino Acids. *Anal. Chem.* **2017**, *89*, 2017–2023.
(53) Eschweiler, J. D.; Martini, R. M.; Ruotolo, B. T. Chemical Probes and Engineered Constructs Reveal a Detailed Unfolding Mechanism for a Solvent-Free Multidomain Protein. *J. Am. Chem. Soc.* **2017**, *139*, 534–540.
(54) Lee, J. W.; Lee, H. H. L.; Davidson, K. L.; Bush, M. F.; Kim, H. I. Structural Characterization of Small Molecular Ions by Ion Mobility Mass Spectrometry in Nitrogen Drift Gas: Improving the Accuracy of Trajectory Method Calculations. *Analyst* **2018**, *143*, 1786–1796.
(55) Pierson, N. A.; Valentine, S. J.; Clemmer, D. E. Evidence for a Quasi-Equilibrium Distribution of States for Bradykinin [M + 3H]3+ Ions in the Gas Phase. *J. Phys. Chem. B* **2010**, *114*, 7777–7783.
(56) Breuker, K.; McLafferty, F. W. Stepwise Evolution of Protein Native Structure with Electrospray into the Gas Phase, 10^{-12} to 10^{2} s. *Proc. Natl. Acad. Sci.* **2008**, *105*, 18145–18152.
(57) Allen, S. J.; Eaton, R. M.; Bush, M. F. Structural Dynamics of Native-Like Ions in the Gas Phase: Results from Tandem Ion Mobility of Cytochrome c. *Anal. Chem.* **2017**, *89*, 7527–7534.

CHAPTER 3

Triboelectric Nanogenerator (TENG) Devices for Improved Sample Consumption in Ion Mobility Mass Spectrometry Analysis of Protein and Protein Complex Ions

This chapter is reproduced with permission from Meagan Gadzuk-Shea, Hikari Akasaki, Ben Zercher, and Matthew F Bush. *In Preparation.*

3.1 Abstract

Ion mobility – mass spectrometry is a powerful tool for characterizing the gas-phase structures of protein and protein complex ions. Many platforms suffer from low duty cycles that waste most of the ions generated from continuous ion sources, which can be detrimental to the analysis of low-quantity samples. Here, for the first time, a triboelectric nanogenerator (TENG) is used to generate pulses of nanoelectrospray-generated ions of proteins and protein complexes for ion mobility – mass spectrometry analysis. TENG devices increase sampling efficiency by creating ion pulses on demand. The TENG-derived mass spectra generally exhibit similar charge-state distributions to those obtained using DC power supplies, consistent with ion formation through a charged-residue mechanism and the retention of native-like structures. However, as the mass of the analyte increases, the quality of the spectrum decreases. The collision cross section values determined from the resulting arrival-time distributions generally fall within ±3% of those measured successively, but with a DC power supply, and those measured previously. However, there are some outliers and differences in the appearance of the distributions. These results suggest that TENG produces similar gas-phase structures and will be useful for sample-limited analytes in experiments with low duty cycles.

3.2 Introduction

Mass spectrometry (MS) has evolved to become a key component of many analytical platforms due to its superior sensitivity, speed, and specificity.[1–4] In native MS, electrospray-generated ions are formed from aqueous solutions that mimic electrolyte concentrations and pH of biological systems.[5] These solution conditions in combination with the softness of electrospray ionization (ESI) enable solution-phase properties to be retained and characteristics such as oligomeric state,[6] noncovalent interactions,[7] and stability[8] to be probed. Native MS is often coupled to ion mobility (IM), which separates ions based on shape and size in the presence of an inert neutral gas and an electric field. The electric field pulls ions through the mobility cell, and collisions with the neutral gas slow the ions down; larger ions will incur more collisions and thus take longer to traverse the mobility cell relative to smaller ions with the same charge state.[9,10] The time an ion takes to traverse the mobility region can be related to the higher-order structure of the analyte by determining the collision cross section using the Mason-Schamp equation.[11,12] The coupling of IM and MS has emerged as an important addition to the structural biology toolkit.[13–16] IM–MS has been leveraged in characterize oligomers implicated neurogenerative diseases,[17] to examine subunit exchange dynamic in biotherapeutics,[18] and to study enzyme inhibitors in bacteria biosynthesis.[19]

Native IM–MS is based largely on ESI[20] and nano–ESI (nESI)[21] because of the gentle nature of electrospray processes compared to other ionization techniques.[22–25] Compared to ESI, nESI requires a lower volume of analyte solution and little-to-no external gas flow.[26] Additionally, ESI and nESI generate distributions of multiply charged ions thereby lowering the mass-to-charge ratio (*m/z*) of large macromolecule ions to within the detection ranges of common mass analyzers..[27,28] However, typical ESI and ambient analogues like desorption ESI[29] and probe ESI[30] rely on high DC voltages to generate charged gas-phase ions from neutral solution-phase species.[31] The often expensive high-voltage power supplies needed for this decrease the accessibility and safety of ESI-MS. Furthermore, conventional ESI and nESI sources generate a continuous flow of ions, of which most is wasted due to the inherent low duty cycle of many ion-analysis platforms.[32–35] Despite the low flow rates of nESI ($nL \cdot min^{-1}$), this low

duty cycle still results in the loss of 80-95% of generated ions on common ion detection platforms, such as time-of-flight (TOF) mass spectrometers.[36]

Recently, triboelectric nanogenerators (TENGs) were introduced as a means to induce nESI in a simple, sustainable, and controlled manner.[31] TENGs convert mechanical energy into electric energy by leveraging electrostatic induction between two materials that have opposite tribo-polarity, or different propensities for gaining/losing charges.[37] Contact electrification, or tribocharging, is a process that has been recorded as far back as ancient Greece,[38] but has only recently emerged as an energy-harvesting technique for scientific advancement.[39,40] In these applications, there are two primary modes for harvesting energy: contact and sliding.[39,41] In contact mode, bringing together of two materials that possess different propensities for losing or gaining electrons will induce the transfer of charges between the materials; a potential difference is formed as the layers are separated.[39,40] Sliding mode is similar, however the motion between the two materials is parallel to the charged surface rather than perpendicular. When the materials are fully aligned, the positive and negative charges between the two materials are equally compensated by each other. The displacement of one of the materials causes an imbalance in these charges, resulting in a potential difference.[40] The amount of energy that is generated through tribocharging is fixed and proportional to the area of the functional material, thereby enabling precise control over how many charges are produced.[31]

Recent experiments have demonstrated the utility of TENG devices in nESI-MS. For example, TENG was used to effectively differentiate counterfeit anti-malarial medicines when coupled to a toothpick emitter.[42] In another study, it was demonstrated that TENG could be used to determine the locations of double bonds in unsaturated lipids.[43] The use of TENG as an nESI power source also offers enhanced control of the number of charges generated, increased sensitivity, and significant reduction in sample consumption.[31] To date, the coupling of TENG–nESI (^{TENG}nESI) to IM has not been demonstrated.

Herein, we demonstrate the ability to measure native-like ions of biomolecules covering a broad range of masses using a sliding TENG device for ^{TENG}nESI coupled to IM–MS. The ability to generate

discrete packets of ions for IM is very advantageous because many implementations of IM have low duty cycles. These results are systematically compared to IM–MS results collected successively with a DC power supply built into the instrument (^{DC}nESI). A comparison of the IM results to values measured previously is presented. Differences in the observed IM–MS data between the two power supplies and previously measured values are discussed in the context of possible ionization effects of ^{TENG}nESI on protein ion formation and structure. These comparisons provide insights into the potential use of ^{TENG}nESI as an alternative, more sample-conservative, power supply for IM–MS analysis of native like biomolecules and provide an important benchmark in incorporating ^{TENG}nESI into the structural biology toolkit. A demonstration of the ability to perform IM – MS analysis of a single burst of ions generated via ^{TENG}nESI on a structures-for-lossless-ion-manipulation (SLIM)[44] IM platform provides evidence for the enhanced sample conservation offered by implementing TENG devices into IM–MS workflows.

3.3 Methods

Human insulin (monomeric mass of 5.7 kDa), cyctochrome *c* (monomeric mass of 12.4 kDa), β-lactoglobulin (monomeric mass of 18.4 kDa), bovine serum albumin (BSA, 67.3 kDa), alcohol dehydrogenase (ADH, tetramer mass of 143 kDa), glyceraldehyde-3-phosphate-dehydrogenase (G3PD, tetramer mass of 145 kDa), and glutamate dehydrogenase (GDH, hexameric mass of 336 kDa) were acquired from Sigma Aldrich (St. Louis, MO) as lyophilized powder. All protein samples were dissolved in 200 mM ammonium acetate at pH 7 to a monomer concentration of 10 μM (insulin and albumin) or 20 μM (all other analytes). Protein solutions were aliquoted in 20 μL portions, flash frozen, and stored at −4 ˚C until use. In some cases, samples were desalted using a micro bio-spin column (Biorad, Hercules, CA).

The TENG device used in this work has two components. The bottom component consists of a thin layer of fluorinated polyethylene measuring 11 cm x 20 cm on top of two static electrodes and mounted on a piece of acrylic with tape. The top component is copper foil that is attached to a piece of acrylic measuring 7.5 cm x 10.2 cm. The top piece is used as the sliding layer to impart electrostatic imbalance in the device.

Unless noted, experiments were conducted on a Waters Synapt G2 modified with an rf-confining drift cell filled with 1.5 to 1.7 Torr He.[45] Cations were generated using nESI from borosilicate capillaries (i.d 0.78 mm) that were pulled to ~1-3 µm on one end with a micropipette puller (Sutter Instruments P-97, Novato, CA). For both power supplies, electrical contact with the solution was made by inserting a platinum wire into the wide end of the capillary. The platinum wire is electrically connected to the sample holder into which the capillary is immobilized; this presents multiple points on the surface that can be electrically connected to secondary devices. Approximately 5 µL of protein solution was loaded into a capillary into which the platinum wire was inserted, the sample holder was interfaced with the instrument and connected to the built-in DC power supply. ^{DC}nESI was achieved by the application of 0.6—1.0 kV of potential to the wire. Ion optic voltages were set to minimize ion activation and typical instrument parameters are detailed in Table S1. Arrival-time distributions (ATDs) at ten drift voltages ranging from 104 —353 V were measured in pseudo-random order and used to determine collision cross section (**Ω**) values following a procedure detailed elsewhere and in the SI.[46] Briefly, the field-dependent measurements are used to determine the *m*/*z*-independent and *m*/*z*-dependent transport time of ions exiting the mobility region of the instrument and entering the TOF mass analyzer. IM measurements made at a single field strength of 5 V·cm^{-1} and at the same mobility pressure as the field-dependent measurements were corrected for this transport time and converted to **Ω** values according to the Mason-Schamp equation:

$$\Omega = \frac{3ez}{16N}\left(\frac{2\pi}{\mu k_B T}\right)^{1/2}\frac{1}{K} \quad (1)$$

Following the field-dependent measurements, the capillary potential was set to 0 kV using the MassLynx user interface and the cord connecting the sample holder to the built-in DC power supply of the instrument was disconnected. A wire with alligator clips on each end was attached to one of the static electrodes of the TENG device on one end and was clipped to the back end of the sample holder on the other end to achieve electrical contact between the capillary and TENG device. Note that TENG

measurements were collected with the same capillary used to collect the field-dependent measurements to reduce the potential of systematic bias between the measurements made using the two power supplies. The other static electrode of the TENG device was grounded on the metal framing of the instrument housing. Prior to initializing data collection, the TENG device was manually actuated multiple times. Triggering nESI using the TENG device consists of sliding the top triboelectric layer along the length of the corresponding triboelectric layer. The motion of the top tribo-layer breaks the electrostatic balance, which is restored by charge-redistribution to the externally connected circuit (*i.e.*, the nESI sample holder).[31] Once a relatively reproducible signal was generated with each actuation, data collection was commenced. The number of TENG events and the duration of the acquisition was determined by visual inspection of the real-time data for adequate intensity to perform analysis. No effort was made to generate identical amounts of signal between the two power supplies. ^{TENG}nESI IM–MS data was collected at a single drift voltage of 212 V and was compared to IM–MS data collected under the same conditions using the DC power supply. Arrival times obtained from ^{TENG}nESI were corrected using the transport time determined from field dependent measurements of the ions generated by ^{DC}nESI.

Measurements on the SLIM platform followed the same signal generation procedure as measurements made using ^{TENG}nESI on the Synapt G2.

Mass spectra were analyzed with MassLynx 4.1 (Waters, Co., Milford, MA). ATDs were extracted and processed using in-house software.[47] The widths of ATDs and apparent Ω distributions are characterized by the 10% and 90% values of a cumulative distribution function applied to the observed distributions (Figure A1). The intensities of mass spectra and ATDs were normalized to a sum equal to one. Analysis of ^{TENG}nESI data incorporated signal from all TENG events in a single acquisition unless otherwise stated.

3.4 Results and Discussion

In this study, we determine the effect of a novel nESI power supply, TENG, on the gas-phase structures of protein and protein complex ions. Additionally, we assess the feasibility of producing adequate signal

from a discrete packet of ions to perform IM–MS analysis. Previous work suggests that TENG devices offer increased sensitivity and reduced sample consumption relative to the conventional DC power supplies used in nESI applications, making it an attractive alternative for increased sample efficiency for analysis of limited samples.[31,43] However, it is unclear if and how much the use of a TENG device to induce nESI influences the gas phase structure of protein ions. The following data compares IM–MS results of protein and protein complex ions generated using a conventional DC power source and a TENG device to assess the inter-device variability.

Each sample was analyzed using both the ^{DC}nESI and ^{TENG}nESI power supplies, but with the same capillary. Ions generated by ^{DC}nESI used the built-in power supply of the instrument. Generating ions by ^{TENG}nESI involved displacing the top copper layer along the length of the bottom, fluorinated polyethylene layer. This motion alters the electrostatic balance on the materials, which generates a net charge displacement. Through charge redistribution, the net charge is output to a connected external circuit, which in this case, is the nESI capillary. This process is illustrated schematically in Figure 1.

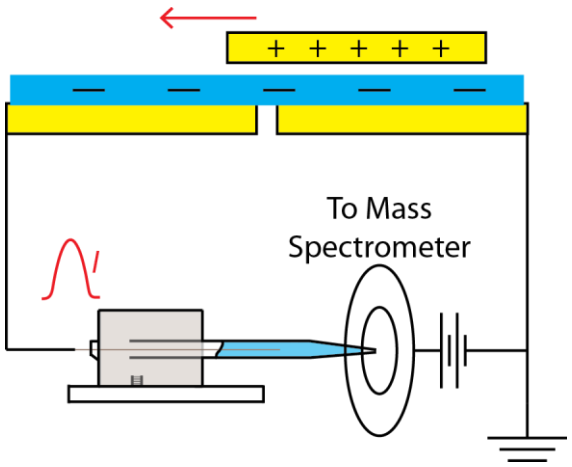

Figure 3.1. Schematic of the integration and operation of the SF-TENG power supply to the mass spectrometer. Yellow represents the copper electrodes and blue represents the fluorinated ethylene propylene layers. The red arrow represents the moving direction of the TENG electrode and

the pulse denotes the generated charge. This charge flow occurs once an onset voltage is reached and excess charges (ions) are leaked from the emitter to the atmospheric-pressure interface of the mass spectrometer.

3.4.1 Comparison of Mass Spectra: For each of the proteins considered, gas-phase ions were observed using ^{TENG}nESI, albeit with varying levels of success. Ions of small to intermediate mass (5.8 – 67.3 kDa) proteins yielded spectra that are very similar in charge state distribution and peak widths relative to the spectra of ^{DC}nESI-generated ions (Fig 2A-B, Fig A2A-B). As the mass of the analyte increases there is a notable broadening in the observed peaks of ions generated using ^{TENG}nESI. For example, Figure 2C shows the spectra of ADH produced using each power source; there is a clear shift to slightly higher *m*/*z* values and reduced resolution between the peaks for different charge states when ADH ions are produced using ^{TENG}nESI (orange trace). However, the ^{TENG}nESI spectrum of G3PD, which is similar in mass to ADH, exhibits only a modest increase in peak width relative to that produced using ^{DC}nESI. For the largest protein complex examined here, GDH, the charge-state distribution becomes narrower in addition to having significantly reduced resolution when produced using ^{TENG}nESI (Figure A2C). Generating a consistent signal of GDH via ^{TENG}nESI was also notably more challenging than any of the other analytes examined here.

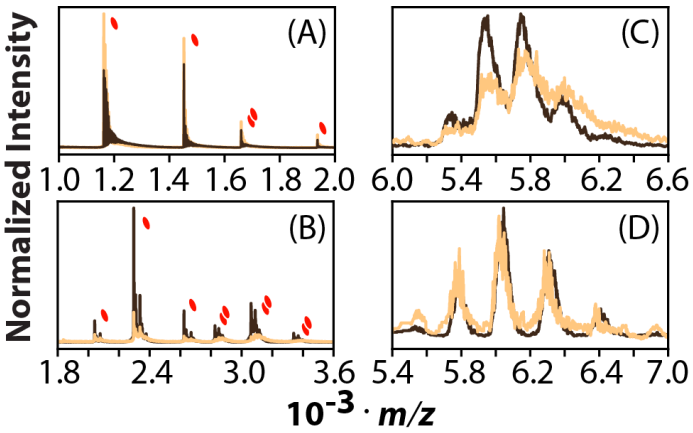

Figure 3.2. Comparison of mass spectra generated using a DC power supply (black trace) and TENG power supply (orange trace) of insulin (A; monomer mass of 5.8 kDa), β-lactoglobulin (B; monomer mass of 18.4 kDa), alcohol dehydrogenase (C; tetramer mass of 143.3 kDa), and glyceraldehyde-3-phosphate-dehydrogenase (D; tetramer mass of 145 kDa). Note that oligomeric state is indicated by the number of red spheres when multiple oligomeric states were observed.

Because the appearance of broader peaks in native mass spectra has previously been linked to incomplete desolvation and increased adduction,[48] these results suggest that the larger, gas-phase ions generated by ^{TENG}nESI may not desolvate as efficiently as those generated by ^{DC}nESI. The extent of droplet desolvation prior to reaching the mass spectrometer interface depends on multiple factors including solvent composition, initial droplet size, and extent of activation prior to mass analysis.[49,50] Furthermore, the characteristics of initial droplets depends on a number of factors including voltage, capillary tip size, and flow rate.[26,51,52] Higher voltages produce larger droplets in nESI.[51] The ^{DC}nESI experiments performed here used DC voltages < 1.0 kV to generate ions, whereas the output voltage of a similar TENG device was estimated to be between 1.6 – 2.0 kV.[31] This suggests that ions generated by ^{TENG}nESI likely originate from larger initial droplets than those generated by ^{DC}nESI. However, because

the charge-state distributions are similar between ions produced by both power supplies suggests that the ions generated by ^{TENG}nESI follow the charged-residue model (CRM).[45,53] or the combined charged-residue, ion-evaporation model.[54] In the CRM, a droplet undergoes solvent evaporation until the Coulombic repulsion of the excess charges exceeds the surface tension of the droplet, at which point a fission event occurs releasing a progeny droplet that is smaller and less charged than the parent droplet. This process continues until the droplet evaporates to dryness and the remaining charges in the final droplet are deposited onto the analyte to produce a bare gas-phase ion.[51,53,55] Larger droplet size has also been correlated to the formation of nonspecific aggregates in droplets,[51] however significantly higher levels of protein aggregation were not observed in the current data. The observation of peak broadening for larger protein ions generated by ^{TENG}nESI suggests that fewer analyte-containing droplets achieve complete desolvation and likely have more adducts that the corresponding ions generated by ^{DC}nESI. Interestingly, previous work revealed no clear relationship between adduct formation and mass or solvent accessible area[48]. As such, it unclear why the larger proteins considered here exhibit broader peaks and diminished resolution when they are generated from ^{TENG}nESI.

3.4.2 Comparing Arrival-Time Distributions and Collision Cross Section (Ω) *values from ^{TENG}nESI to ^{DC}nESI:* To assess the potential use of TENG devices for IM analysis of proteins and protein complexes, it is important to consider whether the gas-phase structures of native-like ions depend on the selection of a TENG versus a DC power supply. To address this, IM was used to analyze protein ions generated from the same borosilicate tip and using each power supply in successive experiments. Comparisons of arrival times refer to the median value of the observed arrival-time distributions that have not been corrected for the time the ion spends regions of the instrument other than the drift region (t_0). Prior to determining Ω values, the observed arrival times were corrected using t_0 values derived from field-dependent measurements and the DC power supply. The corrected arrival times reflect the mobility-dependent drift times, which were then used to determine and compare the Ω values for ions generated from each of the power supplies.

The drift times measured for all cations generated from both ^{TENG}nESI and ^{DC}nESI are compared in Figure 3A. These drift times using the two power supplies are highly correlated, with a slope of 0.972 and Pearson coefficient of 0.999. To further compare ions generated by ^{DC}nESI and ^{TENG}nESI, the relative differences in median arrival time are shown in Figure 3B. Of the 29 ions considered, 20 have median arrival times that differ by ±1% or less, which corresponds to 69% of the ions measured. The remaining 9 ions are within ±3% of one another. The range of differences in median collision cross section ($\widetilde{\Omega}$) values is slightly larger than that of the ATDs and spans from −1.1% to +3.5%, with 18 of the 29 differences are ±1% (Figure A4). For context, the absolute error in Ω values determined using similar IM platforms has been estimated to be <3% based on errors in drift time, pressure, and temperature and the uncertainties < 1%.[56] As the relative differences in $\widetilde{\Omega}$ are slightly larger than the relative difference in drift time observed in this work, the former may have contributions from other errors that are propagated in the analysis.

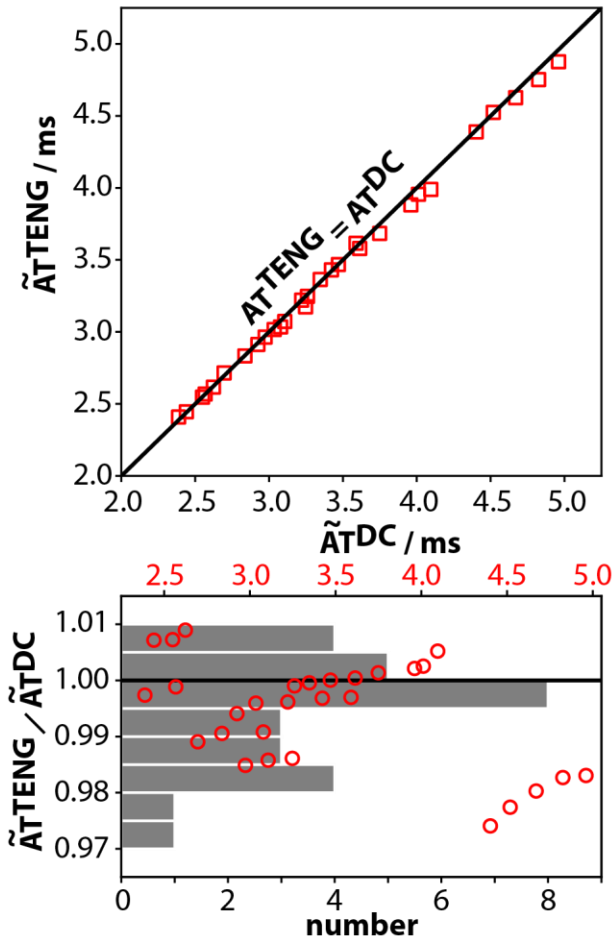

Figure 3.3. Median arrival times measured of ions generated using ^{TENG}nESI as a function of those for ions generated by ^{DC}nESI, with the line representing unity. B) The ratio of the median drift times for ions generated by ^{TENG}nESI to those generated by ^{DC}nESI, plotted as a function of the median drift time of the ions from ^{DC}nESI (red circles, top axis). The bar plot (bottom axis) represents the frequency of ions that occur within a certain ratio; this shows that all ions measured are within ±3%.

Figure 4 shows the ATDs and the corresponding Ω data for monomeric β-lactoglobulin and alcohol dehydrogenase. The widths and shapes of the ATDs for each charge state of the two protein ions appear very similar, suggesting that ^{DC}nESI and ^{TENG}nESI generate similar populations of gas phase structures (Figure 4 A and B). However, a slight growth towards shorter arrival times is observed for lower charge states (*i.e.*, 7+ β-lactoglobulin, as well as 23+ and 24+ alcohol dehydrogenase). Excluding the smallest proteins (insulin and cytochrome *c*), additional intensity at shorter arrival times for the lower charge states is observed for all other protein ions generated by ^{TENG}nESI (Figure A3). This increased intensity at shorter arrival times is also associated by an increase in the apparent widths of the Ω distributions. Of the 29 ions examined, 18 exhibit wider apparent Ω distributions for the ^{TENG}nESI-generated ions than for the ^{DC}nESI-generated ions. This affect also is observed through slightly smaller $\widetilde{\Omega}$ values. The data reveal that as the mass of the analyte increases, the $\widetilde{\Omega}$ values of ions produced by ^{TENG}nESI become increasingly smaller than the corresponding ion generated by ^{DC}nESI. For example, for the smallest protein examined, insulin, the ^{TENG}nESI-generated ion has a $\widetilde{\Omega}$ that is 0.34% larger than the corresponding ^{DC}nESI-generated ion (Figure A3B). Conversely, the 39+ ion of GDH generated using ^{TENG}nESI is 3.48% smaller than that produced using ^{DC}nESI (Figure A3J).

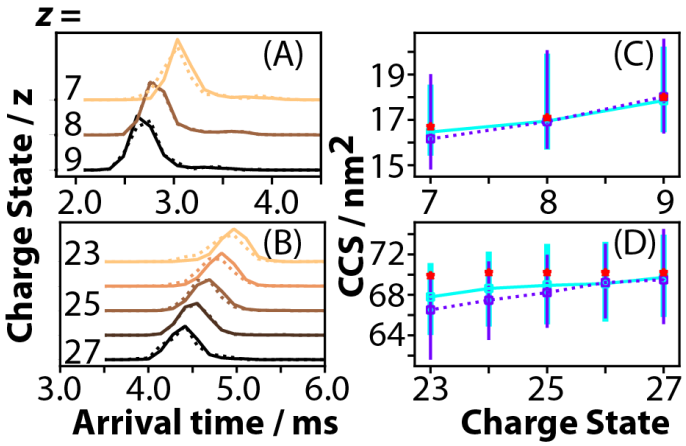

Figure 3.4. Ion mobility results of β-lactoglobulin monomer (A and C) and alcohol dehydrogenase (B and D). Panels A and B show the arrival-time distributions of each charge state observed for a given ion population generated from the DC power supply (solid traces) and from the TENG power supply (dashed traces). Panel C and D show the critical values from the apparent Ω distributions for ions produced using the DC power supply (solid trace) and the TENG power supply (dashed trace). Markers represent the median value of the cumulative distribution applied to each apparent Ω distribution and vertical bars span the 10% to 90% values of this distribution. The red markers denote the corresponding Ω values that have been reported previously.[45,54]

As described above, IM measurements made with the two power supplies deviate more as the mass of the analyte increases, with ions generated by ^{TENG}nESI exhibiting shorter and broader ATDs. This could be explained by charge-stripping, *i.e.*, an ion with charge *z* during IM separation may lose a charge following separation, but before detection in the TOF and thus be detected as a *z*-1 ion in the mass spectrum, which would create artifacts in the IM spectra.[57] Furthermore, because collisional activation for spectral cleaning preferentially eliminates adducts,[58] it is possible that larger analytes that are more

charged and more adducted (as per the results shown here) to lose a charge through the ion evaporation of a charged adduct.[54] Inspecting the ATDs for different charge states can illuminate as to whether charge stripping after IM is occurring. Previous work assessed ATD features appearing at shorter times to charge stripping by comparing the unexpected feature to the ATD for the ion with one greater charge.[59] In that work, there was high fidelity between the ATD of the *z*+1 ion and the small feature in the *z* ion, which provided strong evidence for charge stripping after IM.[59] Compared to that work, the ATDs observed here are much less resolved between charge states for a given protein. For example, Figure A6 displays the ATDs for *z* = 23+ to 25+ of ADH, which shows that the three charge states are not well resolved. Consequently, it is not possible to determine if the apparent shift to more compact structures for ions generated from ^{TENG}nESI reflects difference in structural features during the ionization process or if the ATD includes contributions from charge-stripped ions.

Together, these results indicate that ions produced by either ^{DC}nESI or ^{TENG}nESI likely have similar structures. Furthermore, this suggests that the ionization process induced by the different power sources do not cause ions to undergo significantly differing evaporation processes. However, the observed correlation of larger analyte mass producing smaller $\widetilde{\Omega}$ when the ions are produced by ^{TENG}nESI may suggest that something about the TENG-mediated ionization process causes these larger analytes to assume slightly more compact structures during the evaporation process, especially for lower charge states of a given protein. However, it is also possible that the observed shifts in ATD and apparent $\widetilde{\Omega}$ values are a consequence of charge stripped ions skewing the observed mobility data. Despite the discrepancies observed, the largest difference between $\widetilde{\Omega}$ values (3.48%) determined using the two power supplies is comparable to the upper limit of observed errors for this IM platform.[10]

3.4.3 Comparing $\widetilde{\Omega}$ *values to database* Ω *values:* Determining the variance between the observed $\widetilde{\Omega}$ values here and those reported elsewhere is an important comparison to make, as previously measured values are frequently referenced in the community although agreement on their validity is subject to debate.[12,60] Often, such values for native like proteins are assumed to represent the gas-phase structure

that most closely resembles the corresponding solution-phase structure. Therefore, comparing the present data to previously reported values provides insight into the structural differences of gas phase ions generated with a conventional DC power supply at a different time relative to those generated via TENG in this work.

Figure A5 shows the $\widetilde{\Omega}$ measured through ^{TENG}nESI as a function of those same ions measured previously using ^{DC}nESI on both the same IM platform and a similar platform.[45,56] This comparison reveals a high level of correlation, with a slope of 0.923 and Pearson coefficient of 0.998. Of those measured, 71% are within ±3% of those previously measured, although there are 4 ions that differ by more than 5% with the largest difference being 18.3%. This outlier corresponds to the 3+ ion of insulin. For comparison, 84% of the ions measured here using ^{DC}nESI are within ± 3% of those measured previously. The 3+ insulin ion measured here using ^{DC}nESI is also significantly smaller than the previously reported value (18.0%), which suggests that the source of difference between these values is not the power supply, but something else in the measurement. However, with this outlier removed the average difference decreases to 1.3%. The $\widetilde{\Omega}$ measured here using nESI^{TENG} are systematically smaller than those previously measured (2.5%) which is smaller than the standard deviation of the measured values (4.3%). These results indicate that $\widetilde{\Omega}$ measured using nESI^{TENG} are statistically similar to $\widetilde{\Omega}$ values measured previously and on different platforms.

3.4.4 Coupling ^{TENG}nESI with SLIM: One disadvantage of many IM–MS platforms is their low duty-cycle. In some workflows, less than 1% of a continuous ion beam is actually separated.[61] Therefore, it is of great interest to explore alternative options for improving sample utilization in IM–MS schemes. To evaluate the potential of ^{TENG}nESI as a means to improve sample efficiency, it was interfaced with a bespoke instrument constructed using the structures–for–lossless-ion manipulation (SLIM) architecture.[44] The goal of this experiment was to assess the feasibility of performing IM analysis of a burst of ions generated by a single TENG event, an in turn, characterize the temporal profile of that burst.

Figure 5 shows the resulting IM and mass spectra of insulin ions generated during a single TENG event. The ion count from the highlighted peak is adequate for analysis purposes and is only slightly low relative to previously reported work conducted on that SLIM platform.[44] However, it is important to note that previous measurements on SLIM platforms were collected using a continuous electrospray and longer acquisition times. This data demonstrates that a single TENG event is clearly capable of producing enough ions to perform IM separation and mass spectral detection. Additionally, the width of the IM peak of the ^{TENG}nESI–SLIM generated ions is approximately 10 times broader than the peak observed during IM separation using ^{DC}nESI–SLIM and gating prior to separation (Figure 5C). This difference indicates that the width of the TENG–generated IM data is determined by the temporal width of the TENG event (*i.e* how long the TENG actuation lasts) while the width of the DC–generated IM peak is dominated by diffusion of the released packet of ions and structural heterogeneity of the analyte. This result could be useful for the synchronization of ion generation and IM separation and significantly improve the duty cycle of these experiments.

3.5 Conclusions

A novel electrospray power source, TENG, was incorporated into two IM–MS platforms. For a broad range of masses and proteins, native-like ions generated using this novel power supply yielded arrival-time distributions and $\widetilde{\Omega}$ values that are similar to those measured using typical DC power supplies. On average, the median arrival time of ions measured using ^{TENG}nESI are very similar to those measured concurrently with ^{DC}nESI (0.6%). Additionally, the $\widetilde{\Omega}$ values measured using ^{TENG}nESI are similar to those reported previously (2.5%). Excluding the 3+ insulin ion, which has a significantly larger difference from previously reported values than any of the other ions considered here, minimizes the average difference in $\widetilde{\Omega}$ values to 1.3%. Generally, the mass spectra generated by the two power supplies exhibit similar charge state distributions. As the mass of analyte increases, there is more evidence for ion adduction and less complete desolvation for ions generated by ^{TENG}nESI. Nonetheless, these results

suggest that gas phase ions form according to the CRM[20] and possess similar structural characteristics when generated from either power supply.

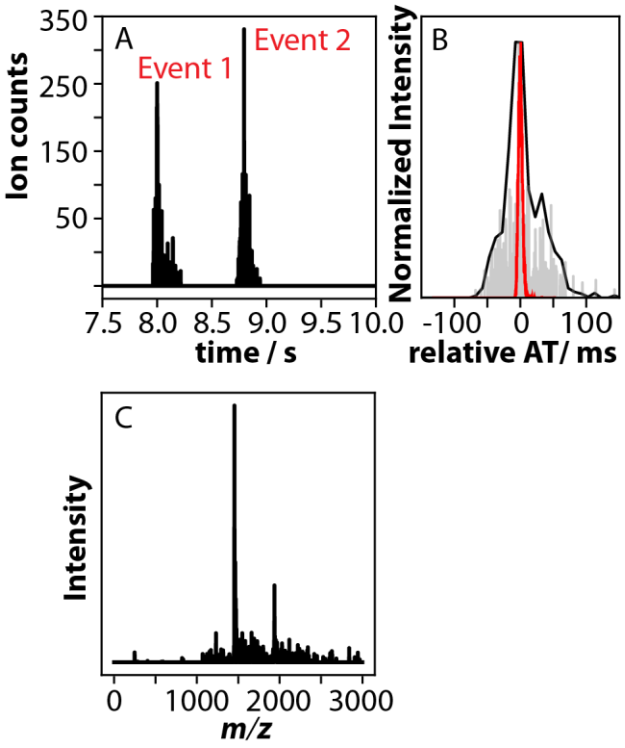

Figure 3.5. (A) Arrival-time distributions of insulin ions generated from two TENG events and probed using a SLIM−based instrument; note that the TENG events are not synchronized with the time axis in these experiments. (B) Comparison of IM peak widths observed when ions are generated using ^{DC}nESI, accumulated in the trap region, and released into the mobility cell as a discrete packet for IM separation (red trace) and when ions are generated from ^{TENG}nESI and introduced to the SLIM mobility cell without trapping and gating (C) The mass spectrum of the ions observed from the second TENG event.

This work demonstrates the first application of ^{TENG}nESI for the IM–MS analysis of moderate to large ions of native like proteins and protein complexes. It was also shown that a single TENG event can generate enough ions of a small protein for IM - MS analysis on SLIM platforms. This power supply presents an attractive alternative for electrospray ionization for improved sample efficiency and lower consumption. The work shown here serves as a starting point for the application of TENG to the analysis of native like protein ions. Optimizing the geometries of the TENG devices for the generation of large biomolecule ions (> 150 kDa) will aid in extending its application to biotherapeutics and other large analytes of interest. Additional work further characterizing TENGs ability to analyze native like structures by IM - MS with a focus on single-event analysis will provide additional insight into the utility of ^{TENG}nESI as a complement to the structural biology toolkit. More generally, these results indicate that TENG offers great potential for enabling the broader use of low-duty cycle IM and MS approaches to sample-limited questions in structural biology.

3.6 Supporting Information

Supporting Information can be found in Appendix A

3.7 Acknowledgments

This material is based upon work supported by the National Science Foundation under CHE–1807382 (M. F. B.).

3.8 References

(1) McLafferty, F. W. Tandem Mass Spectrometry. *Science* **1981**, *214* (4518), 280–287. https://doi.org/10.1126/science.7280693.

(2) El-Aneed, A.; Cohen, A.; Banoub, J. Mass Spectrometry, Review of the Basics: Electrospray, MALDI, and Commonly Used Mass Analyzers. *Appl. Spectrosc. Rev.* **2009**, *44* (3), 210–230. https://doi.org/10.1080/05704920902717872.

(3) McLafferty, F. W. Mass Spectrometry across the Sciences. *Proc. Natl. Acad. Sci. U. S. A.* **2008**, *105* (47), 18088–18089. https://doi.org/10.1073/pnas.0800784105.

(4) Finehout, E. J.; Lee, K. H. An Introduction to Mass Spectrometry Applications in Biological Research. *Biochem. Mol. Biol. Educ.* **2004**, *32* (2), 93–100. https://doi.org/10.1002/bmb.2004.494032020331.

(5) Lorenzen, K.; Duijn, E. van. Native Mass Spectrometry as a Tool in Structural Biology. *Curr. Protoc. Protein Sci.* **2010**, *62* (1), 17.12.1-17.12.17. https://doi.org/10.1002/0471140864.ps1712s62.

(6) Lu, Y.; Liu, H.; Saer, R. G.; Zhang, H.; Meyer, C. M.; Li, V. L.; Shi, L.; King, J. D.; Gross, M. L.; Blankenship, R. E. Native Mass Spectrometry Analysis of Oligomerization States of Fluorescence Recovery Protein and Orange Carotenoid Protein: Two Proteins Involved in the Cyanobacterial Photoprotection Cycle. *Biochemistry* **2017**, *56* (1), 160–166. https://doi.org/10.1021/acs.biochem.6b01094.

(7) Barrera, N. P.; Isaacson, S. C.; Zhou, M.; Bavro, V. N.; Welch, A.; Schaedler, T. A.; Seeger, M. A.; Miguel, R. N.; Korkhov, V. M.; van Veen, H. W.; Venter, H.; Walmsley, A. R.; Tate, C. G.; Robinson, C. V. Mass Spectrometry of Membrane Transporters Reveals Subunit Stoichiometry and Interactions. *Nat. Methods* **2009**, *6* (8), 585–587. https://doi.org/10.1038/nmeth.1347.

(8) Wang, W.; Kitova, E. N.; Klassen, J. S. Nonspecific Protein−Carbohydrate Complexes Produced by Nanoelectrospray Ionization. Factors Influencing Their Formation and Stability. *Anal. Chem.* **2005**, *77* (10), 3060–3071. https://doi.org/10.1021/ac048433y.

(9) May, J. C.; McLean, J. A. Ion Mobility-Mass Spectrometry: Time-Dispersive Instrumentation. *Anal. Chem.* **2015**, *87* (3), 1422–1436. https://doi.org/10.1021/ac504720m.

(10) Allen, S. J.; Bush, M. F. Radio-Frequency (Rf) Confinement in Ion Mobility Spectrometry: Apparent Mobilities and Effective Temperatures. *J. Am. Soc. Mass Spectrom.* **2016**, *27* (12), 2054–2063. https://doi.org/10.1021/jasms.8b05184.

(11) Mason; E.A.; McDaniel; E.W. *Transport Properties of Ions in Gases*; Wiley: New York, 1988.

(12) Gabelica, V.; Shvartsburg, A. A.; Afonso, C.; Barran, P.; Benesch, J. L. P.; Bleiholder, C.; Bowers, M. T.; Bilbao, A.; Bush, M. F.; Campbell, J. L.; Campuzano, I. D. G.; Causon, T.; Clowers, B. H.; Creaser, C. S.; Pauw, E. D.; Far, J.; Fernandez-Lima, F.; Fjeldsted, J. C.; Giles, K.; Groessl, M.; Hogan, C. J.; Hann, S.; Kim, H. I.; Kurulugama, R. T.; May, J. C.; McLean, J. A.; Pagel, K.; Richardson, K.; Ridgeway, M. E.; Rosu, F.; Sobott, F.; Thalassinos, K.; Valentine, S. J.; Wyttenbach, T. Recommendations for Reporting Ion Mobility Mass Spectrometry Measurements. *Mass Spectrom. Rev.* **2019**, *38* (3), 291–320. https://doi.org/10.1002/mas.21585.

(13) Thalassinos, K.; Slade, S. E.; Jennings, K. R.; Scrivens, J. H.; Giles, K.; Wildgoose, J.; Hoyes, J.; Bateman, R. H.; Bowers, M. T. Ion Mobility Mass Spectrometry of Proteins in a Modified Commercial Mass Spectrometer. *Int. J. Mass Spectrom.* **2004**, *236* (1), 55–63. https://doi.org/10.1016/j.ijms.2004.05.008.

(14) Woods, L. A.; Radford, S. E.; Ashcroft, A. E. Advances in Ion Mobility Spectrometry–Mass Spectrometry Reveal Key Insights into Amyloid Assembly. *Biochim. Biophys. Acta BBA - Proteins Proteomics* **2013**, *1834* (6), 1257–1268. https://doi.org/10.1016/j.bbapap.2012.10.002.

(15) Pukala, T. Importance of Collision Cross Section Measurements by Ion Mobility Mass Spectrometry in Structural Biology. *Rapid Commun. Mass Spectrom.* **2019**, *33* (S3), 72–82. https://doi.org/10.1002/rcm.8294.

(16) Seo, J.; Hoffmann, W.; Warnke, S.; Bowers, M. T.; Pagel, K.; von Helden, G. Retention of Native Protein Structures in the Absence of Solvent: A Coupled Ion Mobility and Spectroscopic Study. *Angew. Chem. Int. Ed.* **2016**, *55* (45), 14173–14176. https://doi.org/10.1002/anie.201606029.

(17) Österlund, N.; Moons, R.; Ilag, L. L.; Sobott, F.; Gräslund, A. Native Ion Mobility-Mass Spectrometry Reveals the Formation of β-Barrel Shaped Amyloid-β Hexamers in a Membrane-Mimicking Environment. *J. Am. Chem. Soc.* **2019**, *141* (26), 10440–10450. https://doi.org/10.1021/jacs.9b04596.

(18) Debaene, F.; Wagner-Rousset, E.; Colas, O.; Ayoub, D.; Corvaïa, N.; Van Dorsselaer, A.; Beck, A.; Cianférani, S. Time Resolved Native Ion-Mobility Mass Spectrometry to Monitor Dynamics of IgG4 Fab Arm Exchange and "Bispecific" Monoclonal Antibody Formation. *Anal. Chem.* **2013**, *85* (20), 9785–9792. https://doi.org/10.1021/ac402237v.

(19) Chan, D. S.-H.; Hess, J.; Shaw, E.; Spry, C.; Starley, R.; Dagostin, C.; Dias, M. V. B.; Kale, R.; Mendes, V.; Blundell, T. L.; Coyne, A. G.; Abell, C. Structural Insights into Escherichia Coli Phosphopantothenoylcysteine Synthetase by Native Ion Mobility–Mass Spectrometry. *Biochem. J.* **2019**, *476* (21), 3125–3139. https://doi.org/10.1042/BCJ20190318.

(20) Dole, M.; Mack, L. L.; Hines, R. L.; Mobley, R. C.; Ferguson, L. D.; Alice, M. B. Molecular Beams of Macroions. *J. Chem. Phys.* **1968**, *49* (5), 2240–2249. https://doi.org/10.1063/1.1670391.

(21) Wilm, M.; Mann, M. Analytical Properties of the Nanoelectrospray Ion Source. *Anal. Chem.* **1996**, *68* (1), 1–8. https://doi.org/10.1021/ac9509519.

(22) Munson, M. S. B.; Field, F. H. Chemical Ionization Mass Spectrometry. I. General Introduction https://pubs.acs.org/doi/pdf/10.1021/ja00964a001 (accessed Oct 13, 2020). https://doi.org/10.1021/ja00964a001.

(23) Mirsaleh-Kohan, N.; Robertson, W. D.; Compton, R. N. Electron Ionization Time-of-Flight Mass Spectrometry: Historical Review and Current Applications. *Mass Spectrom. Rev.* **2008**, *27* (3), 237–285. https://doi.org/10.1002/mas.20162.

(24) Barber, M.; Bordoli, R. S.; Elliott, G. J.; Sedgwick, R. D.; Tyler, A. N. Fast atom bombardment mass spectrometry https://pubs.acs.org/doi/pdf/10.1021/ac00241a002 (accessed Oct 13, 2020). https://doi.org/10.1021/ac00241a002.

(25) Leney, A. C.; Heck, A. J. R. Native Mass Spectrometry: What Is in the Name? *J. Am. Soc. Mass Spectrom.* **2017**, *28* (1), 5–13. https://doi.org/10.1007/s13361-016-1545-3.

(26) Schmidt, A.; Karas, M.; Dülcks, T. Effect of Different Solution Flow Rates on Analyte Ion Signals in Nano-ESI MS, or: When Does ESI Turn into Nano-ESI? *J. Am. Soc. Mass Spectrom.* **2003**, *14* (5), 492–500. https://doi.org/10.1016/S1044-0305(03)00128-4.

(27) Whitehouse, C. M.; Dreyer, R. N.; Yamashita, Masamichi.; Fenn, J. B. Electrospray Interface for Liquid Chromatographs and Mass Spectrometers. *Anal. Chem.* **1985**, *57* (3), 675–679. https://doi.org/10.1021/ac00280a023.

(28) Nohmi, T.; Fenn, J. B. Electrospray Mass Spectrometry of Poly(Ethylene Glycols) with Molecular Weights up to Five Million. *J. Am. Chem. Soc.* **1992**, *114* (9), 3241–3246. https://doi.org/10.1021/ja00035a012.

(29) Takáts, Z.; Wiseman, J. M.; Gologan, B.; Cooks, R. G. Mass Spectrometry Sampling Under Ambient Conditions with Desorption Electrospray Ionization. *Science* **2004**, *306* (5695), 471–473. https://doi.org/10.1126/science.1104404.

(30) Mandal, M. K.; Chen, L. C.; Hashimoto, Y.; Yu, Z.; Hiraoka, K. Detection of Biomolecules from Solutions with High Concentration of Salts Using Probe Electrospray and Nano-Electrospray Ionization Mass Spectrometry. *Anal. Methods* **2010**, *2* (12), 1905–1912. https://doi.org/10.1039/C0AY00530D.

(31) Li, A.; Zi, Y.; Guo, H.; Wang, Z. L.; Fernández, F. M. Triboelectric Nanogenerators for Sensitive Nano-Coulomb Molecular Mass Spectrometry. *Nat. Nanotechnol.* **2017**, *12* (5), 481–487. https://doi.org/10.1038/nnano.2017.17.

(32) Ruotolo, B. T.; Benesch, J. L. P.; Sandercock, A. M.; Hyung, S.-J.; Robinson, C. V. Ion Mobility–Mass Spectrometry Analysis of Large Protein Complexes. *Nat. Protoc.* **2008**, *3* (7), 1139–1152. https://doi.org/10.1038/nprot.2008.78.

(33) Bohrer, B. C.; Merenbloom, S. I.; Koeniger, S. L.; Hilderbrand, A. E.; Clemmer, D. E. Biomolecule Analysis by Ion Mobility Spectrometry. *Annu. Rev. Anal. Chem. Palo Alto Calif* **2008**, *1*, 293–327. https://doi.org/10.1146/annurev.anchem.1.031207.113001.

(34) Loboda, A. V.; Chernushevich, I. V. A Novel Ion Trap That Enables High Duty Cycle and Wide m/z Range on an Orthogonal Injection TOF Mass Spectrometer. *J. Am. Soc. Mass Spectrom.* **2009**, *20* (7), 1342–1348. https://doi.org/10.1016/j.jasms.2009.03.018.

(35) Senko, M. W.; Hendrickson, C. L.; Emmett, M. R.; Shi, S. D. H.; Marshall, A. G. External Accumulation of Ions for Enhanced Electrospray Ionization Fourier Transform Ion Cyclotron Resonance Mass Spectrometry. *J. Am. Soc. Mass Spectrom.* **1997**, *8* (9), 970–976. https://doi.org/10.1016/S1044-0305(97)00126-8.

(36) Hashimoto, Y.; Hasegawa, H.; Satake, H.; Baba, T.; Waki, I. Duty Cycle Enhancement of an Orthogonal Acceleration TOF Mass Spectrometer Using an Axially-Resonant Excitation Linear

Ion Trap. *J. Am. Soc. Mass Spectrom.* **2006**, *17* (12), 1669–1674. https://doi.org/10.1016/j.jasms.2006.07.020.

(37) Zou, H.; Zhang, Y.; Guo, L.; Wang, P.; He, X.; Dai, G.; Zheng, H.; Chen, C.; Wang, A. C.; Xu, C.; Wang, Z. L. Quantifying the Triboelectric Series. *Nat. Commun.* **2019**, *10* (1), 1427. https://doi.org/10.1038/s41467-019-09461-x.

(38) McCarty, L. S.; Whitesides, G. M. Electrostatic Charging Due to Separation of Ions at Interfaces: Contact Electrification of Ionic Electrets. *Angew. Chem. Int. Ed.* **2008**, *47* (12), 2188–2207. https://doi.org/10.1002/anie.200701812.

(39) Zhu, G.; Pan, C.; Guo, W.; Chen, C.-Y.; Zhou, Y.; Yu, R.; Wang, Z. L. Triboelectric-Generator-Driven Pulse Electrodeposition for Micropatterning. *Nano Lett.* **2012**, *12* (9), 4960–4965. https://doi.org/10.1021/nl302560k.

(40) Zhu, G.; Peng, B.; Chen, J.; Jing, Q.; Lin Wang, Z. Triboelectric Nanogenerators as a New Energy Technology: From Fundamentals, Devices, to Applications. *Nano Energy* **2015**, *14*, 126–138. https://doi.org/10.1016/j.nanoen.2014.11.050.

(41) Castle, G. S. P. Contact Charging between Insulators. *J. Electrost.* **1997**, *40–41*, 13–20. https://doi.org/10.1016/S0304-3886(97)00009-0.

(42) Bernier, M. C.; Li, A.; Winalski, L.; Zi, Y.; Li, Y.; Caillet, C.; Newton, P.; Wang, Z. L.; Fernández, F. M. Triboelectric Nanogenerator (TENG) Mass Spectrometry of Falsified Antimalarials. *Rapid Commun. Mass Spectrom.* **2018**, *32* (18), 1585–1590. https://doi.org/10.1002/rcm.8207.

(43) Bouza, M.; Li, Y.; Wu, C.; Guo, H.; Wang, Z. L.; Fernández, F. M. Large-Area Triboelectric Nanogenerator Mass Spectrometry: Expanded Coverage, Double-Bond Pinpointing, and Supercharging. *J. Am. Soc. Mass Spectrom.* **2020**, *31* (3), 727–734. https://doi.org/10.1021/jasms.0c00002.

(44) Allen, S. J.; Eaton, R. M.; Bush, M. F. Analysis of Native-Like Ions Using Structures for Lossless Ion Manipulations. *Anal. Chem.* **2016**, *88* (18), 9118–9126. https://doi.org/10.1021/acs.analchem.6b02089.

(45) Allen, S. J.; Giles, K.; Gilbert, T.; Bush, M. F. Ion Mobility Mass Spectrometry of Peptide, Protein, and Protein Complex Ions Using a Radio-Frequency Confining Drift Cell. *Analyst* **2016**, *141* (3), 884–891. https://doi.org/10.1039/c5an02107c.

(46) Laszlo, K. J.; Munger, E. B.; Bush, M. F. Folding of Protein Ions in the Gas Phase after Cation-to-Anion Proton-Transfer Reactions. *J. Am. Chem. Soc.* **2016**, *138* (30), 9581–9588. https://doi.org/10.1021/jacs.6b04282.

(47) Bush, M. F.; Campuzano, I. D. G.; Robinson, C. V. Ion Mobility Mass Spectrometry of Peptide Ions: Effects of Drift Gas and Calibration Strategies. *Anal. Chem.* **2012**, *84* (16), 7124–7130. https://doi.org/10.1021/ac3014498.

(48) McKay, A. R.; Ruotolo, B. T.; Ilag, L. L.; Robinson, C. V. Mass Measurements of Increased Accuracy Resolve Heterogeneous Populations of Intact Ribosomes. *J. Am. Chem. Soc.* **2006**, *128* (35), 11433–11442. https://doi.org/10.1021/ja061468q.

(49) Liigand, P.; Heering (Suu), A.; Kaupmees, K.; Leito, I.; Girod, M.; Antoine, R.; Kruve, A. The Evolution of Electrospray Generated Droplets Is Not Affected by Ionization Mode. *J. Am. Soc. Mass Spectrom.* **2017**, *28* (10), 2124–2131. https://doi.org/10.1007/s13361-017-1737-5.

(50) Gardner, M. W.; Brodbelt, J. S. Reduction of Chemical Noise in Electrospray Ionization Mass Spectrometry by Supplemental IR Activation. *J. Am. Soc. Mass Spectrom.* **2009**, *20* (12), 2206–2210. https://doi.org/10.1016/j.jasms.2009.08.008.

(51) Davidson, K. L.; Oberreit, D. R.; Hogan, C. J.; Bush, M. F. Nonspecific Aggregation in Native Electrokinetic Nanoelectrospray Ionization. *Int. J. Mass Spectrom.* **2017**, *420*, 35–42. https://doi.org/10.1016/j.ijms.2016.09.013.

(52) Xia, Z.; Williams, E. R. Effect of Droplet Lifetime on Where Ions Are Formed in Electrospray Ionization. *Analyst* **2018**, *144* (1), 237–248. https://doi.org/10.1039/C8AN01824C.

(53) Konermann, L.; Ahadi, E.; Rodriguez, A. D.; Vahidi, S. Unraveling the Mechanism of Electrospray Ionization. *Anal. Chem.* **2013**, *85* (1), 2–9. https://doi.org/10.1021/ac302789c.

(54) Allen, S. J.; Schwartz, A. M.; Bush, M. F. Effects of Polarity on the Structures and Charge States of Native-Like Proteins and Protein Complexes in the Gas Phase. *Anal. Chem.* **2013**, *85* (24), 12055–12061. https://doi.org/10.1021/ac403139d.

(55) Kebarle, P.; Verkerk, U. H. Electrospray: From Ions in Solution to Ions in the Gas Phase, What We Know Now. *Mass Spectrom. Rev.* **2009**, *28* (6), 898–917. https://doi.org/10.1002/mas.20247.

(56) Bush, M. F.; Hall, Z.; Giles, K.; Hoyes, J.; Robinson, C. V.; Ruotolo, B. T. Collision Cross Sections of Proteins and Their Complexes: A Calibration Framework and Database for Gas-Phase Structural Biology. *Anal. Chem.* **2010**, *82* (22), 9557–9565. https://doi.org/10.1021/ac1022953.

(57) Allen, S. J.; Eaton, R. M.; Bush, M. F. Structural Dynamics of Native-Like Ions in the Gas Phase: Results from Tandem Ion Mobility of Cytochrome c. *Anal. Chem.* **2017**, *89* (14), 7527–7534. https://doi.org/10.1021/acs.analchem.7b01234.

(58) Chowdhury, S. K.; Katta, V.; Beavis, R. C.; Chait, B. T. Origin and Removal of Adducts (Molecular Mass = 98 u) Attached to Peptide and Protein Ions in Electrospray Ionization Mass Spectra. *J. Am. Soc. Mass Spectrom.* **1990**, *1* (5), 382–388. https://doi.org/10.1016/1044-0305(90)85018-H.

(59) Freeke, J.; Bush, M. F.; Robinson, C. V.; Ruotolo, B. T. Gas-Phase Protein Assemblies: Unfolding Landscapes and Preserving Native-like Structures Using Noncovalent Adducts. *Chem. Phys. Lett.* **2012**, *524*, 1–9. https://doi.org/10.1016/j.cplett.2011.11.014.

(60) May, J. C.; Morris, C. B.; McLean, J. A. Ion Mobility Collision Cross Section Compendium. *Anal. Chem.* **2017**, *89* (2), 1032–1044. https://doi.org/10.1021/acs.analchem.6b04905.

(61) Hoaglund, C. S.; Valentine, S. J.; Clemmer, D. E. An Ion Trap Interface for ESI−Ion Mobility Experiments. *Anal. Chem.* **1997**, *69* (20), 4156–4161. https://doi.org/10.1021/ac970526a.

Chapter 4

So *How* Bad is Ammonium Acetate for Native Mass Spectrometry? A Quantitation of pH Changes in Nanoelectrospray Ionization (nESI) Using a Fluorescent Probe

This chapter is reproduced with permission from Meagan M. Gadzuk-Shea, Evan Hubbard, and Matthew F. Bush. *In Preparation.*

4.1 Abstract

The ability of nanoelectrospray ionization (nESI) to generate a continuous flow of charged droplets is reliant on the electrolytic nature of the process. This necessary electrochemistry can lead to the build of redox products in the capillary solution and change the composition of the ESI solution. This consequence can have significant implications for native mass spectrometry (MS), which aims to probe the intact and folded form of biomolecules. Here, a pH-sensitive fluorescent probe, SNARF-4F, is used to quantify changes in solution composition during nESI for conditions relevant to native MS. The results show that the extent and rate of change in solution composition is dependent on several experimental parameters. There is a strong correlation between the extent and rate of change in solution composition and the magnitude of nESI current, as well as the concentration of electrolyte. Changes in solution composition are less significant when a negative potential is applied. Alternating the polarity of the applied potential is demonstrated as an effective strategy to mitigate the observed changes.

4.2 Introduction

The advent of electrospray ionization (ESI) made possible the analysis of large biomolecules by mass spectrometry (MS).[1] In ESI, an analyte solution is put into electrical contact with a potential that drives the generation of charged droplets. Most ESI sources use metal capillaries with large (~100-200 µm) tips that require external pumping and applied potentials in excess of 3 kV to move solutions and generate charged droplets.[1–5] These conditions can result in poor sample efficiency and sample aggregation due to formation of large droplet.[5,6] The mid-90's brought the introduction of nanoelectrospray ionization (nESI) from the work of Wilm and Mann, which sought to address some of the challenges associated with standard ESI sources.[5,7] In this altered source, droplets ≤ 200 nm in diameter could be produced (compared to 1 µm in diameter in ESI).[5] Generally, nESI utilizes borosilicate glass or fused silica capillaries that have been pulled to a tip of 1 to 10 µm and that have inner diameters of less than 1000 µm. The application of a potential is achieved by coating the capillary with a conductive material such as gold, or through the insertion of a wire. In nESI, a potential of ≤ 1.5 kV is sufficient to generate a Taylor cone and movement of the sample solution can be maintained through electrokinetic flow, without applying additional pressure.[4] Flow rates in nESI devices range from 6 – 50 nL min^{-1} and depend on the composition of the solvent, the tip orifice, and distance to counter electrode (mass spectrometer).[6,8–10] For comparison, flow rates in conventional ESI devices are in the range of µL min^{-1} and are determined by external pumping.[9,10]

Native MS coupled to nESI has been used to study intact structures of biomolecules.[11–13] In native MS, protein ions are generated from solutions with ionic strength and pH similar to a biological system, *e.g.*, aqueous ammonium acetate (10-500 mM) adjusted to pH 7.[14] Ammonium acetate has been used widely due to its volatility, which makes it particularly amenable to MS. Additionally, the combination of ammonia (pK_a 9.25) and acetic acid (pK_a 4.8) results in a mixture that is close to neutral.[15] Unfortunately, this solvent system is *not* a buffer at this pH and therefore is ineffective at resisting pH changes. Buffers are most effective at resisting pH changes within a ± 1 range of their pK_a.[16] Susa and coworkers investigated using ammonium phosphate for native-MS, which has a p$K_{a,2}$ 7.4 and would therefore buffer

at neutral pH.[17] However, achieving usable data required the use of emitter tips ≤ 1.6 μm, which suffer from clogging and are challenging to reproduce consistently. Ammonium bicarbonate is another popular option for native MS,[18] however it has been shown to induce protein unfolding and is therefore not an ideal option.[19,20]

The electrolytic nature of the electrospray process is not really a debate, more so the implications and analytical significance of its occurrence.[21] During electrospray, application of a potential to a capillary containing solution causes electrophoretic separation of the ions present. Species of the same charge as the applied potential move toward the exit of the capillary, which creates a destabilization effect at the capillary tip.[22] When the coulombic repulsion at the tip exceeds the surface tension of the liquid, charged droplets are released in a Taylor cone.[2,5,23] Through solvent evaporation and fission events, these charged droplets become bare ions which can be detected by a mass spectrometer.[3] The ability to generate this continuous flow of charged droplets requires that charge balancing reactions occur.[24,25] For example, when a positive potential is applied and thus positive charges are expelled, and only electrons flow through the wire electrode, it follows that electrons must be produced within the solution.[25,26] Charge balancing occurs through redox reactions, which can produce electrons, positively charged ions, and negatively charged ions to effect the required charge balance.[21,27–29] The specific redox reactions that occur during electrospray are determined by a complex interaction of experimental parameters such as flow rate, concentration of electrolytes, magnitude of electrospray current, and redox properties of species within the system.[21,28] As a point of reference, Table 1 lists the possible redox reactions that water can undergo during ESI, which only represent a subset of the possibilities for a given solvent system,[30]

Table 5.1. Electrochemical reactions of water during ESI[a]

Positive ionization (oxidation)		**Negative ionization (reduction)**	
Reaction	E^0 (V) vs SHE	Reaction	E^0 (V) vs SHE
$2H_2O \rightarrow O_2 + 4H^+ + 4e^-$	1.23	$2H_2O + 2e^- \rightarrow H_2 + 2OH^-$	0.07
$4OH^- \rightarrow 2H_2O + O_2 + 4e^-$	0.40	$O_2 + 4H^+ + 4e^- \rightarrow 2H_2O$	1.23
$2OH^- \rightarrow H_2O_2 + 2e^-$	0.88	$2H_2O + 4e^- + O_2 \rightarrow 4OH^-$	0.40
$2H_2O \rightarrow H_2O_2 + 2H^+ + 2e^-$	1.77	$2H^+ \rightarrow H_2$	0.00
$OH^- \rightarrow OH^* + e^-$	1.89	$2H_2O + O_2 + 2e^- \rightarrow H_2O_2 + 2OH^-$	-0.13
		$O_2 + e^- \rightarrow O_2^-$	-0.33
		$O_2 + 2H^+ + 2e^- \rightarrow H_2O_2$	0.70

[a] Listed reactions and potentials from Van Berkel and Kertesz.[30]

There are many direct observations of redox reactions concomitant with electrospray. For example, Blades *et al* demonstrated electrode oxidation by using zinc or iron wires as electrospray electrodes; both metals have low reduction potentials. Following the application of a positive potential to either electrode resulted in the appearance of the oxidized form of the metal, Zn^{2+} and Fe^{2+}, in the mass spectra.[22] Work by Zhou *et al* revealed that is was possible for solution species to participate in the redox chemistry by monitoring the absorbance spectrum, and therefore extent of oxidation, of a porphyrin solution as a function of electrospray parameters.[31] There is much literature regarding the electrolytic nature of ESI.[21,32–38] It has been leveraged for the analysis of molecules otherwise challenging to create ions of, such as metallocene's, fullerenes, and inorganic compounds.[35,36,39–41] Changes in solution composition can also affect redox chemistry occurring during electrospray.[27,29,42] Gatlin and Tureček used Fe and Ni complexes with 2,2'-bipyridine (bpy) to estimate the pH of the microdroplets formed from ESI relative to the bulk solution pH. The dissociation of the metal-bpy complexes was correlated to the solution-phase chemistry, and revealed a 10^3 to 10^4 increase in $[H_3O]^+$ concentration (pH = 2.6-3.3)

compared to the bulk solution.[43] In other work investigators observed a 5 to 7 fold increase in proton concentration in droplets that had traveled 7 mm from the capillary tip by measured the fluorescence ratio of a pH-sensitive probe.[44] These studies and others have established that redox chemistry occurs during the electrospray process and that the pH of electrospray-produced droplets can be very different than bulk solution.

Despite the obvious occurrence of redox-induced changes in solution pH, little work has examined pH change in solution conditions utilized for native MS. If native MS strives to examine the native fold of protein structure, changes in the solvent pH within the duration of the experiment could impede this effort by inducing disassociation of noncovalent complexes and/or denaturation as pH becomes increasingly acidic or basic, depending on the polarity of ionization.[15] This is especially prevalent for efforts examining proteins that are highly sensitive to the pH of their environment. For example, the dissociation constant of dimerization of the chaperone HSPB5 α-crystallin domain changes by a factor of 15 between solution pH 7.5 and 6.5.[45] Intrinsically disordered proteins, like the Alzheimer's disease related α-synuclein, have demonstrated aggregation dependence on solution pH,[46] yet the use of nESI native MS to study them is rapidly growing.[47] Therefore, it is of great interest to determine to what extent these changes occur and devise schemes to avoid and/or mitigate these changes. In this work, we aim to quantitatively assess the changes in pH of solutions typically implemented in native-MS experiments using nESI in both positive and negative ionization modes. It is widely believed that the structures of gas-phase ions reflect, at least to some extent, a snapshot of the solution structure prior to ionization.[48–50] Therefore, we specifically examine the changes within the bulk solution of the nESI capillary, rather than the plume. We evaluate these changes as a function of time, with a focus on timescales typical for these experiments. This timescale takes into consideration typical flowrates and volumes loaded into nESI capillaries.[6,13,51] Additionally, we explore alternating polarities during experiments as a strategy for mitigating pH changes during experiments.

4.3 Methods

4.3.1 Samples and solutions: SNARF™-4F 5-(and-6)-carboxylic acid (SNARF-4F) was purchased from Fisher Scientific (Rockwood, TN) as a lyophilized solid. A stock solution was prepared by dissolving the solid in 18.6 MΩ water to a concentration of 2 mM. Aliquots containing 5 µL of stock solution were kept frozen at –80 ˚C or –18 ˚C and protected from light until use. Prior to experiments, one aliquot was thawed and diluted to a final concentration of 1 µM. Solution conditions utilized in this work are listed in Table 1 and were prepared as follows. Aqueous ammonium acetate solutions were prepared at 200 mM and 1 M concentration; 10 mM solutions were prepared through serial dilution of the 200 mM solution. Solution pH was adjusted with a solution hydrochloric acid or ammonium hydroxide with the same concentration as the electrolyte in the solution being adjusted.

4.3.2 Fluorescence Measurements: To assess the fluorescence signature of SNARF-4F under conditions of the nESI for native MS, SNARF-4F was added to pH-adjusted solutions of 200 mM ammonium acetate to a concentration of 500 nM. Final solution pHs were 3.4, 5.4, 6.4, 7.4, 8.4, and 9.4. A small volume of each solution was added to a quartz microcuvette (path length, 1.0 cm). Emission spectra were collected with a Perkin Elmer LS-50B luminescence spectrophotometer (Perkin Elmer, Walham, MA) using an excitation wavelength of 530 nm, an excitation and emission slit width of 10 nm, and a scan rate of 200 nm min^{-1} from 400 nm to 780 nm. Data was processed using a home-built script.

4.3.3 Experimental setup: To probe solution pH during electrospray, a system capable of detecting fluorescence was designed, is described herein, and is shown in Figure 1. A 530 nm LED (Luxeon Stars, Brantford, Ontario) was mounted to a 50 mm x 45 mm High Alpha Heat Sink (Luxeon Stars) using Arctic Silver low thermal resistance adhesive. The LED power was controlled by a DC power supply (72-420, Tenma labs) and set to 1A (V, Figure B1). The light emitted from the LED was passed through a 525 nm bandpass filter (ED00256B, Omega Optical, LLC,, Brattleboro, VT) then collimated through an aspheric condenser lens with a focal length of 20 mm (ACL2520U-A, Thorlabs). The collimated light was focused through a coated plano convex lens with a focal length of 75 mm (LA1608-A, Thorlabs). As the focused light began to expand, it was re-collimated through another

aspheric condenser lens with a 20 mm focal length. The re-collimated light illuminated a nESI capillary containing SNARF-4F solution. The capillary was placed below a filter wheel (Thorlabs FW102C, Newton, NJ) containing two bandpass filters (3305/25, 3416/25, Omega Optical, LLC, Brattleboro, VT). The entrance to the filter wheel contained a long-pass filter (FGL550, Thorlabs) to further increase the rejection of residual excitation light. The resulting fluorescence at 577 nm and 655 nm is detected by a camera (ASI120MM-S, ZWO, Suzhou, China) positioned above the orifice of the filter wheel. The camera was placed at a slight angle, approximately 12˚, to further reduce the amount of scattered excitation light captured in images. The LED, filter wheel, and camera operation are synchronized and automated using software developed in-house.

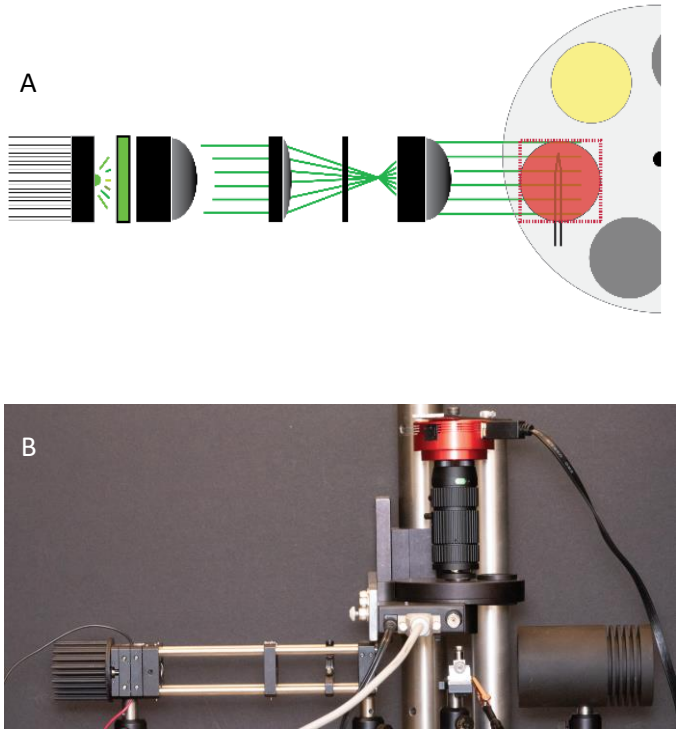

Figure 5.1. (A) Diagram of instrumental setup and (B) picture of the apparatus from the side. Samples are illuminated with a semi-collimated beam of 532 nm light from a LED. The filter wheel contains a long pass filter to eliminate the LED wavelength and two bandpass filters to

capture the fluorescence of SNARF-4F at 577 nm and 655 nm. The fluorescence at each wavelength is imaged at fixed intervals by a camera positioned above the orifice of the filter wheel. The camera is mounted above the filter wheel at a slight angle to reduce the amount of scattered light captured in the images.

4.3.4 Calibration: Solutions of 400 nM SNARF-4F were prepared in 200 mM ammonium phosphate at known pH values for use as standards. Ratiometric analysis of the fluorescence signatures of these solutions was used for semi-quantitation of experimental shifts in the fluorescence ratio. The final pH values of the standard solutions were 3.5, 5.4, 6.4, 7.4, 8.4, and 9.3. The ratio of fluorescence at 655 nm relative to 577 nm was recorded at each pH value six times. The platinum wire was inserted in the capillary for each measurement, although no potential was applied. Measurements were taken in a pseudo-random order to minimize systemic biases. Each measurement used a new borosilicate capillary and the platinum wire was rinsed with 18.6 MΩ water prior to insertion into the solution-containing capillary. These steps were taken in effort to fully capture the variability in the experimental measurements. The resulting data were fit to a curve to relate pH to fluorescence ratio (R) according to Equation 1:[52,53]

$$R = {R_B 10^{pH-PK} + R_A}/{1 + 10^{pH-PK}} \qquad Equation\ 1$$

Where R_B and R_A are the fluorescence ratio for the most basic and acidic forms of SNARF-4F, respectively, and PK is a modified form of pK_a that accounts for the dependence of SNARF-4F fluorescence intensity on the environment.[53] The fitting parameters from that were leveraged to estimate experimental pH values from ratiometric measurements following the rearranged form of Equation 1:[52]

$$pH = PK + \log_{10}\left(\frac{(R - R_A)}{(R_B - R)}\right) \qquad Equation\ 2$$

4.3.5 Electrospray experiments: Approximately 10 µL of diluted SNARF-4F was loaded into a borosilicate capillary that was pulled to an ~ 1-3 µm tip (Sutter Instruments P-97). A platinum wire was inserted through the wide end of the capillary to make electrical contact with the solution. Electrospray was achieved by applying 0.7 to 2.7 kV of potential to the wire using a Bertan high voltage power supply (205B-03R, Hicksville, NY). The current was detected by placing a metal plate ~10 mm from the capillary tip that measured the potential different between the collection plate and ground using a picoammeter (Keithley 485, Cleveland, OH). The magnitude of applied potential was adjusted to maintain a relatively constant electrospray current (±10 nA). Any experiments that exhibited erratic current were terminated and a new tip loaded. Fluorescence was initiated by illuminating the sample with semi-collimated 530 nm light for fixed intervals of time. Images were collected using in-house written software that automated the LED, the filter wheel, and the camera. For each data point, two images were collected for each fluorescence wavelength. Images were collected with an exposure time of 400 ms and a gain of zero. For most experiments, fluorescence images were recorded every 25 seconds for 125 iterations. During rotation of the filter wheel, the LED was switched off to minimize bleaching the probe.

4.3.6 Polarity switching: A Jennings RF1J-26S vacuum relay was used to enable polarity switching. This relay was integrated into a circuit with binary operation; one position connected to a power supply operated at one polarity and the other position connected to a different power supply operated at the opposite polarity. In-house software enabled the frequency and number of polarity switches to be set by the user and synchronized with the fluorescence experiments. Voltages on the two attached power supplies were adjusted throughout the experiment to maintain relatively constant and equal current magnitudes, although this was minimally necessary.

4.3.7 Data processing: Ratiometric analysis of the fluorescence intensity of SNARF-4F at 655 nm and 577 nm was performed to relate the fluorescence ratio to solution pH. Prior to ratio analysis, the intensities of two images taken at the same time point were added for each test wavelength. The data was then binned with a block size of 4 or 16 pixels and masked using a minimum threshold to eliminate low-intensity interference and a maximum threshold to exclude a few “hot” pixels on the sensor. The intensity

of fluorescence at 655 nm was plotted against the fluorescence intensity at 577 nm for each data point. The slope resulting from regression analysis of these data was taken as the experimental ratio, which was then related to apparent solution pH. This workflow is outlined in Figure B2.

4.4 Results and Discussion

The objective of study was to quantify and better understand the effects of electrospray on the pH of solutions typically employed in native MS. Using a pH-dependent fluorescent probe with a pK_a of ~6.4 and a simple LED microscopy setup, ratiometric measurements were recorded and provided insight into these processes. Specifically, we were interested in the dependence of these changes on the magnitude of the applied electrospray current, electrolyte concentration, the starting pH of the solution, and the polarity of the applied voltage. These points of interest were selected because they could have significant implications for the assumptions made regarding protein structure during native MS experiments, depending on the extent of the pH changes.

Fluorescence spectra of SNARF-4F prepared in 200 mM ammonium phosphate at various pH values were used to select bandpass filter for the fluorescence imaging experiments. At the lowest solution pH, 3.4, excitation of SNARF-4F by 530 nm light results in an emission spectrum with maximum intensity around 585 nm and a less intense shoulder at longer wavelengths. As shown in Figure B4, the feature at 585 nm decreases in intensity with increasing solution pH (almost disappearing by pH 7.4) and the longer-wavelength feature increases in intensity and appears centered near 652 nm. Between pH 8.4 and 9.4, the intensity of the feature near 652 nm is nearly constant, indicating that the deprotonated form of SNARF-4F is predominant.[44]

The effectiveness of the fluorescent probe for studying solutions around neutral pH was validated through the development of a calibration scheme. A series of solutions at known pH values containing SNARF-4F were prepared. Fluorescence images of SNARF-4F were recorded at 577 nm and 655 nm, and a ratio between these emissions was calculated as described in the *Methods*. Plotting the ratio as a function of pH yielded a sigmoidal relationship, with the steepest region falling between pH values of ~

6.5 and 8.5. This is consistent with the expected acid-base equilibria[54] and previous pH-dependent measurements of SNARF-4F using other fluorescence measurements.[55] The resulting curve was used to parameterize Equation 1 The potential variance of these measurements was evaluated by repeatedly adjusting the capillary position to mimic inter-experiment tip placement variations. Additionally, this series of measurements was recorded on different days to characterize any potential day-to-day differences. The results were to fit a sigmoidal curve. The covariance matrix produced from this fitting was used to generate 1000 solutions to Equation 1 This analysis provided insight to the range of ratio values that could be used to estimate pH values for experimental results. Conveniently, the determined range fell between ratio values corresponding to pH values between 6 and 8, which is a highly relevant range for native MS experiments. However, as shown in figure B3, this range corresponds to the steepest range in the sigmoidal calibration curve. This means that within this range, the fluorescence ratio observed will be highly sensitive to the solution pH.

4.4.1 A Typical Case: A starting point for many native MS workflows is to prepare samples in aqueous 200 mM ammonium acetate at neutral pH and to use positive ionization mode with a modest electrospray current.[6,12,56,57] Because of the prevalence of these conditions, they will be referred to as "the status quo" for the remainder of this discussion and will pertain to experiments using a solution of 200 mM electrolyte at pH 7 with 60 nA of applied current under positive polarity. This "status quo" current is slightly elevated compared to the reported thresholds for nESI of 30 nA,[6] as this low of a current generally leads to poor signal for MS.[48] Additionally, a surplus of replicates under these "status quo" conditions were performed spanning multiple weeks and sample preparations to capture the inherent variability of these measurements. To aid in discussion of the results, the experiment is presented in four regions with the first three regions corresponding to 10-minute intervals of electrospray, the final region refers to 30 minutes to the end of the experiment and is around 20 minutes in duration.

Figure 2 shows the results from many "status quo" replicates. Under these conditions, the solutions displayed an initial fluorescence ratio of 2.41 (95% CI: 2.35-2.47) corresponding to a solution pH of 6.92 (95% CI: 6.91-6.94). During the first 10 minutes of electrospray (region I) the solutions

exhibit a slow decrease in fluorescence ratio averaging −0.02 min^{-1}. In region II, 10-20 minutes, the rate of change in fluorescence ratio increases to −0.0604 min^{-1}. Region III is similar, exhibiting an average rate of change of −0.0529 min^{-1}. Region IV reveals significant slowing in the rate of decrease of −0.0211 min^{-1} and apparent leveling of the ratio is observed at the conclusion of the experiment. All status-quo experiments result in an apparent decrease in solution pH of over 1 pH unit; on average, the solution pH drops below 6 after 34 minutes of electrospray. We attribute the increased stability of fluorescence ratios at longer times (and lower pH) to (1) increased buffering at lower pH by acetic acid, which has a pK_a of 4.8, and (2) the sigmoidal fluorescence ratio and pH.

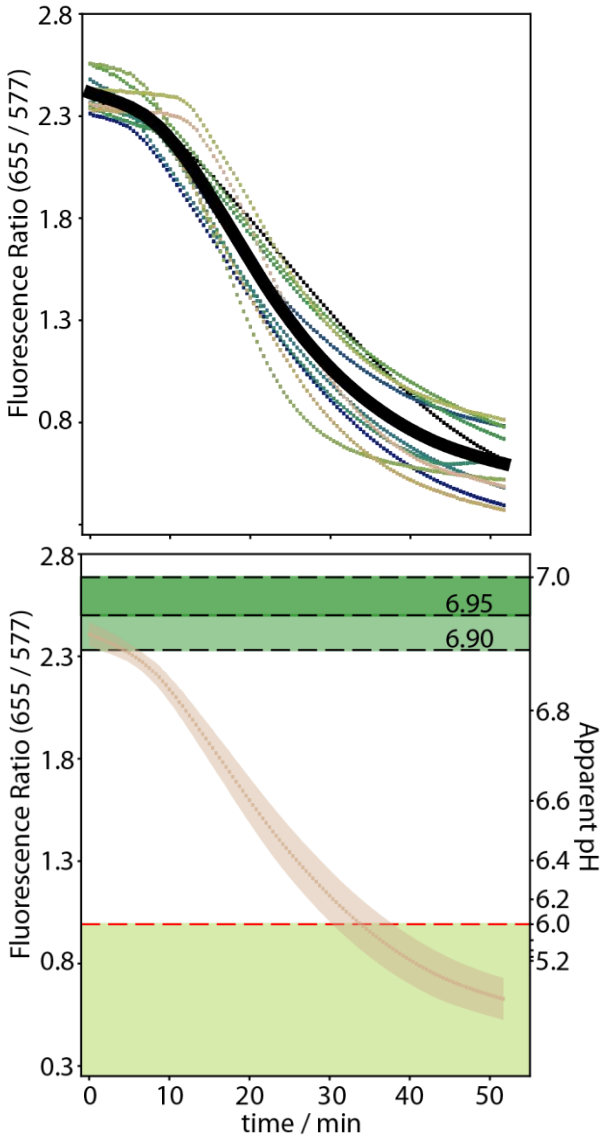

Figure 4.2. Changes in solution pH during electrospray under conditions commonly used in native MS workflows. These experiments were performed under "status-quo" conditions, which refers to an aqueous solution at neutral pH with 200 mM concentration of electrolyte and an electrospray current of 60 nA. Over a 52-minute period, 125 sets of images capturing the fluorescence of SNARF-4F at 655 nm and 577 nm are recorded. Ratiometric analysis of the fluorescence intensity at the two wavelengths was used to estimate the solution pH. The markers correspond to the average ratio of 11 replicates and the shaded region

spans the 95% CI. Green shaded regions correspond to pH regions of interest: near-neutral pH and pH ≤ 6. Solutions under status-quo conditions exhibit a slow decrease in fluorescence ratio during the first ten minutes of electrospray. After ten minutes, the ratio drops at a faster rate indicating more rapid acidification of the solution. From approximately 40 minutes to the end of the experiment the rate of change in the fluorescence ratio exhibits asymptotic behavior.

4.4.2 Effect of electrospray current: To characterize the effects of electrospray current on the pH of solutions in native MS experiments, experiments that varied only the magnitude of electrospray current were conducted. Although electrospray currents are not typically reported in literature, it is common for a range of potentials applied to generate ions to be included in experimental sections. Values between 0.7 kV and 2.0 kV[58–60] are common; the width of that range suggests that different studies fall under different current regimes. For this work, we chose to examine a low current of 30 nA, a moderate current of 60 nA, and a high current of 120 nA, which fall within the range of currents that have been reported.[6,61] Figure 3 shows the fluorescence ratios as a function of time for each of the three currents. There is a clear relationship between the onset and magnitude of change in fluorescence ratio and the magnitude of the electrospray current. During region I, the smallest current (30 nA, black trace) exhibits the slowest change in fluorescence ratio and the largest current (120 nA, green trace) displays the most dramatic change in fluorescence ratio. An intermediate amount of current (60 nA, tan trace) falls in between the two extremes. However, beyond region I, the rate of change in fluorescence ratio displays some convergence between the three magnitudes of current. Within region III, the three test currents display changes that span 0.0172 min^{-1} which is a 75% reduction in the range of rates observed in region I. In region IV, the rate of change slows in all three cases, with 120 nA leveling off the most dramatically, although it exhibits the greatest overall change in fluorescence ratio relative to of the other currents. In region IV, 30 nA induces the fastest relative change in fluorescence ratio, which may be attributed to the

higher currents causing the solution to reach a pH within the buffering capacity of acetic acid sooner. The enhanced resistance of that same solution to changes in solution pH when electrosprayed at 30 nA may be attributed to slower production of redox products relative to the two higher currents.

Overall, all currents exhibit a substantial decrease in fluorescence ratio and therefore acidification during electrospray, although at different rates and to varying extents. The highest magnitude of current, 120 nA, displays an 85% drop in fluorescence ratio and 60 nA and 30 nA decreasing 74% and 65%, respectively. All three test currents result in acidification of more than 1 pH unit within the timescale of the experiment. At 120 nA of current, the drop below pH 6 occurs after ~20.4 minutes of nESI. These results demonstrate that using lower electrospray currents in nESI will delay the onset of acidification from redox chemistry.

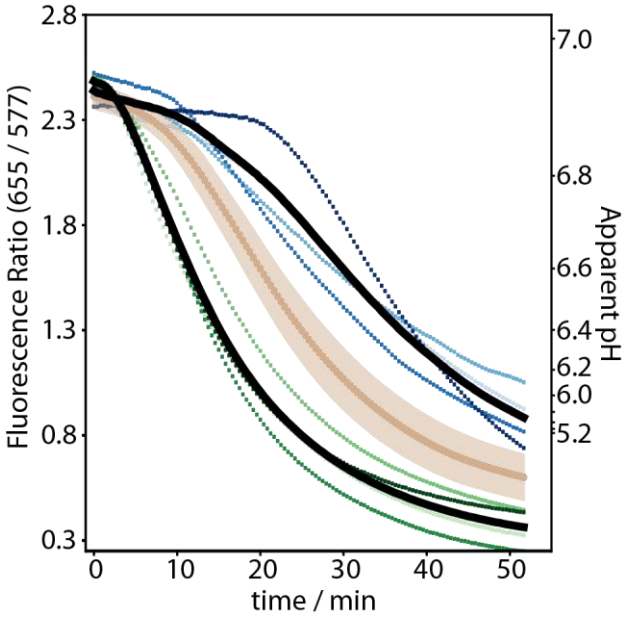

Figure 4.3. The effect of current on the rate and extent of changes in solution pH during electrospray. Black traces represent the average values of multiple (4-11) replicates. Blue traces correspond to 30 nA of current and green traces correspond to 120 nA of current. Results from

status quo experiments are shown in tan, with the markers representing the average ratio and the shaded region span the 95% CI.

4.4.3 Effect of electrolyte concentration: Although ammonium acetate has very little buffering capacity at pH 7, it has been suggested that higher concentrations of ammonium acetate will improve the buffering capacity, but will also increase the formation rate of REDOX products.[15] To explore which of these factors would prevail, SNARF-4F was electrosprayed from aqueous ammonium acetate at 10 mM, 200 mM, and 1 M that was adjusted to pH ~7.0; this range of concentrations spans that used in most native MS experiments.[50,62,63] The results from applying 60 nA of current to SNARF-4F prepared in each of these solutions are shown in Figure 4. The observed trends demonstrate that increasing electrolyte concentration increases the initial resistance to nESI-induced changes in pH. During region I, the fluorescence ratio decreases > 17 times faster in the 10 mM solution than in the 1 M solution. The steep drop in the fluorescence ratio indicates rapid acidification of the 10 mM solution. The 1 M solution exhibits a slope close to zero (-0.008 min^{-1}) during the same period. However, as nESI continues, the rate of acidification of the 10 mM solution slows while the 1 M solution begins to acidify more quickly. For example, in region II, the 10 mM solution exhibits an average decrease in fluorescence ratio of -0.04 min^{-1}, which is 70% less than that observed during the first ten minutes. During region III, this rate slows further to −0.01 min^{-1} and then to 0.003 min^{-1} in the region IV. Conversely, the rate of acidification of the 1 M solution is almost constant from regions I through III. Beyond region III, there is a dramatic change in this rate to a rate that is 10 times faster than the former part. However, the fastest rate of acidification observed with 1M electrolyte is still about half that observed for the 10mM electrolyte.

These results indicate that higher electrolyte concentrations in nESI applications are more effective at resisting pH changes from electrospray relative to lower electrolyte concentrations. High concentrations of ammonium acetate can also improve the quality of protein mass spectra by reducing the relative abundance of metal ion adducts.[63] However, high concentrations of electrolyte can affect the

strengths of some protein-ligand[64] and protein-protein interactions[63,65]. Therefore, care should be taken when choosing the concentration of electrolyte to use with respect to the analyte system of interest.

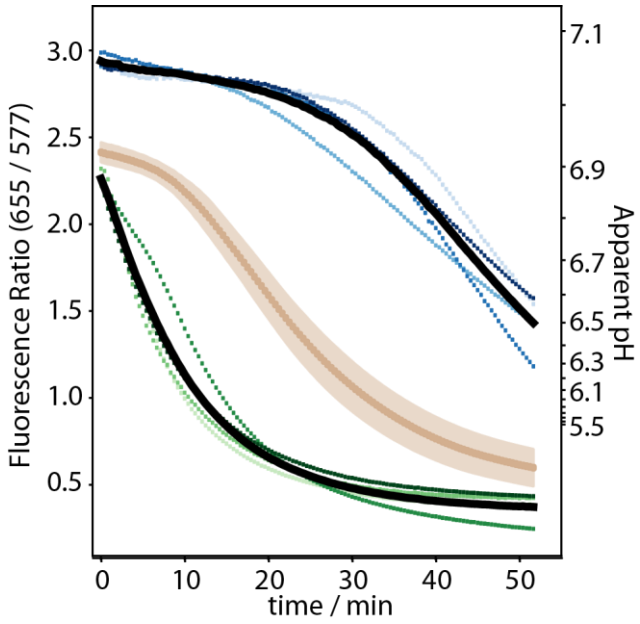

Figure 4.4. The effect of ammonium acetate concentration on the response to the solution to an electrospray current of 60 nA in positive-ion mode. Black traces represent the average ratio for a given set of replicates. The highest electrolyte concentration, 1 M ammonium acetate, blue traces, exhibits the greatest resistance to redox-induced changes in solution pH. The lowest concentration, 10 mM, green traces, displays rapid acidification almost immediately upon the application of a potential. In final 20 minutes, region IV, solutions of 200 mM (tan trace) and 10 mM ammonium acetate exhibit similar slowing in the acidification, indicative of acetic acid buffering.

4.4.4 Initial pH of solution: Figure B5 shows the fluorescence response of SNARF-4F in solutions with different initial pH values under positive ionization, 60 nA of current, and 200 mM

electrolyte. A solution starting at a pH of 8 exhibits the most rapid change in ratio for any conditions examined here. In region I, the ratio drops an average of 0.7434 min^{-1}. The apparent solution pH drops below 7 after 13 minutes of electrospray and below 6 after 23 minutes. Interesting, the apparent pH of a solution starting at pH 8 acidifies to below pH 6 before a solution under the same conditions that started at pH 7. One possible explanation of this observation is the equilibrium of redox reactants present in the solution at the different solution pH values and their relativity reactivity. In other words, a solution at pH 8 will have more hydroxide ions available to be oxidized relative to a solution at pH 7.[27]

4.4.5 Effect of electrospray polarity: Although most native MS experiments probe native-like cations, there is also interest in the properties of native-like anions.[66] Therefore, it is relevant to understand how the application of positive versus negative potential during electrospray affects the characteristics of the electrospray solution. Therefore, we considered the "status quo" conditions described above (*i.e.*, 200 mM electrolyte, pH 7, 60 nA of nESI current; Table 1), but under negative polarity. The results from this set of conditions are shown by the black trace in Figure 5. A negative potential clearly has a vastly different effect on the electrospray solution compared to a positive potential under the same conditions. The apparent pH of the electrospray solution changes less than 0.1 pH unit under negative polarity, which corresponds to a 25% increase in hydroxide concentration. Conversely, a positive potential induces a shift of multiple pH units, an increase in proton concentration of several orders of magnitude. Because these conditions produced such contrasting results depending on the polarity of the applied potential, we chose to also examine 10 mM electrolyte under negative polarity. The results from applying −60 nA of current to a solution with 10 mM electrolyte is shown by the green trace in Figure 5. For comparison, results from the same experiment under positive mode are shown in tan. Under negative polarity, the fluorescence ratio increased by 3.815 which is an increase in apparent solution pH of 0.65. Over regions I to III, the change in fluorescence ratio appears very linear and exhibits a rate of change of +0.087 min^{-1} with a correlation of 0.999. The rate of change slows only slightly in the final 20 minutes of nESI to +0.055 min^{-1} although with slightly less linearity (R^2 = 0.997). This small variation in the rate of change of the fluorescence ratio over the course of the experiment is in stark

contrast to the results for the same solution but a positive potential. Under positive polarity, the rate of change differs by 98% in the first 10 minutes of nESI relative to the last 20 minutes. For the same time segments, the rate of change differs by 38% when a negative potential is applied.

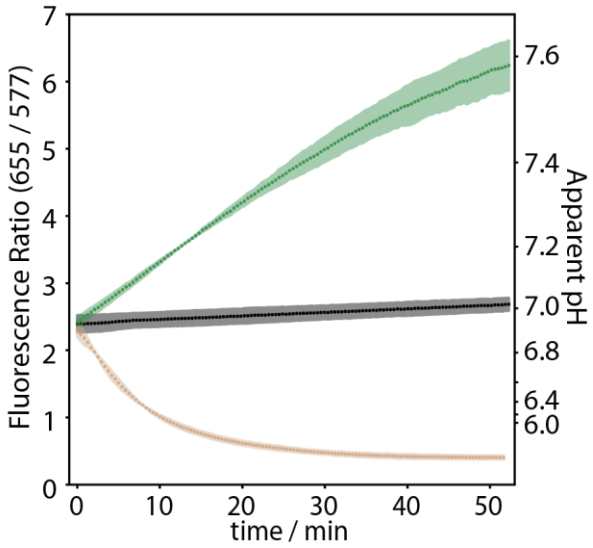

Figure 4.5. The effect of the polarity of the applied potential on changes in solution composition during nESI. Shaded regions represent the highest and lowest values observed in replicate analysis (n = 2 to 6). Solutions of 200 mM ammonium acetate and 60 nA under negative polarity (black traces) exhibit a nearly constant fluorescence ratio throughout the experiment. Solutions of 10 mM ammonium acetate and 60 nA under negative polarity (green traces) display modest alkalization, however the change in apparent solution pH is much less than what is observed for the same solution and current, but with a positive applied potential (tan trace).

The persistent rate of change in fluorescence ratio with negative ionization and 10 mM ammonium acetate can be attributed to the solution not reaching the buffering regime of ammonium (pK_a

9.25). The minimal alkalization of the 200 mM ammonium acetate solution is less straightforward to explain. With a platinum electrode, water oxidation and reduction should be the primary source of charge balance and redox-induced changes in solution pH under positive and negative polarity, respectively.[30] Because there a multiple redox reactions that water can undergo (Table 1) that vary in reduction potential (and therefore probability of occurrence) , it is plausible that the reduction reactions that take place under negative-mode ionization contribute less pH-altering species.[30] This may account for both the slower rate of alkalization observed as well as the smaller overall change in solution composition over the timeframe of the experiment. However, this is a gross oversimplification of the electrochemistry that is likely occurring within the solution and means to provide only a basis of explanation.[27]

4.4.6 Polarity switching; Because both alkalization and acidification were observed in the preceding experiments, we hypothesized that alternating both polarities would counteract the buildup of pH-changing redox products. To test this hypothesis, we used a high-voltage relay to alternate between two high-voltage power supplies operated at opposite polarities. The relay was computer controlled and synchronized with the fluorescence imaging apparatus. These experiments were conducted with aqueous 200 mM ammonium acetate and 60 nA of current for both polarities. The solution exhibited significant resistance to pH changes when the polarity of the applied potential was alternated every 25 seconds. Over the course of the 40-minute experiment, the apparent solution pH exhibited a decrease of < 0.05, indicating that insignificant concentrations of redox products accumulate in the solution. As a control, the blue trace shows the change in fluorescence ratio when the electrode is alternated between a positive potential and ground (*i.e.*, no electrospray) every 25 seconds, which exhibits an extended period of no change in solution composition followed by a steady decrease in fluorescence that is consistent with acidification. These results indicate that alternating between positive and negative electrosprays is an effective strategy for minimizing the buildup of redox products that affect the pH of solutions for native MS.

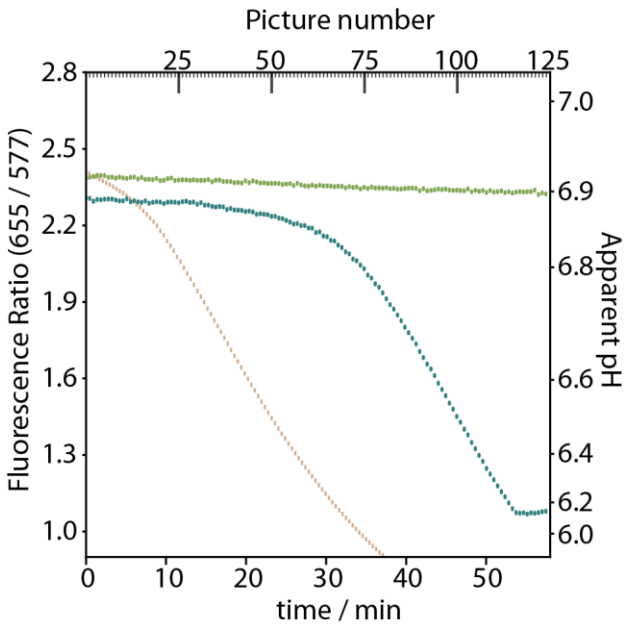

Figure 5.6. Results from switching the polarity of the applied potential during electrospray with varying frequency. The fluorescence ratio stays nearly constant when the applied potential is switched from positive to negative every set of pictures, or approximately every 25 seconds (green trace). When a positive potential is alternated with no potential every set of pictures, approximately 25 seconds, the solution exhibits significant acidification beginning after approximately 30 minutes (blue trace). For comparison, the average fluorescence ratio from status quo experiments is shown (tan trace) which shows that even alternating between a positive potential and no potential offsets changes in solution pH significantly and that alternation of the polarity counteracts the buildup of redox products.

4.5 Conclusions

The results presented here provide clear evidence for significant changes in electrospray solutions relevant to the field of nESI and native MS, especially the most common conditions (Figure 2). For experiments conducted in positive ionization mode, the data demonstrate that, for the same electrolyte concentration, a higher magnitude of electrospray current will incur more rapid acidification of the solution relative to lower currents (Figure 3). Additionally, it was shown that higher concentrations of electrolyte improve the ability of a solution to resist changes in solution composition during electrospray (Figure 4). Adjusting the initial pH of the solution to between 6 and 8 revealed that starting at a higher pH increases the rate at which acidification occurs over the entire duration of the experiment (Figure B5). Operating under negative ionization induces less changes in the solution composition during electrospray. Interestingly, at 200 mM electrolyte, solutions maintained a near-neutral pH during the entire experiment when a negative potential is applied.

Strategies to mitigate the solution changes observed here are crucial for the study of analytes that are sensitive to solution pH. Switching the polarity of the applied potential between positive and negative during the experiment is an effective method for counteracting redox-induced pH changes in solution. This setup is similar to a recent report that induced ESI, which generates bipolar droplets, is also effective at minimizing oxidative processes in the bulk solution.[42] Other promising strategies include using solutions that can buffer at neutral pH in combination with much smaller electrospray tips.[17,67] Further development of methods for minimizing redox process during nESI will facilitate the ability to examine proteins with structures that are dependent on the composition of their environment.

4.6 Supporting Information

Supporting Information can be found in Appendix B

4.7 Acknowledgments

This material is based upon work supported by the National Science Foundation under CHE–1807382 (M. F. B.).

4.8 References

(1) Fenn, J. B.; Mann, M.; Meng, C. K.; Wong, S. F.; Whitehouse, C. M. Electrospray Ionization for Mass Spectrometry of Large Biomolecules. *Science* **1989**, *246* (4926), 64–71.

(2) Whitehouse, C. M.; Dreyer, R. N.; Yamashita, Masamichi.; Fenn, J. B. Electrospray Interface for Liquid Chromatographs and Mass Spectrometers. *Anal. Chem.* **1985**, *57* (3), 675–679. https://doi.org/10.1021/ac00280a023.

(3) Konermann, L.; Ahadi, E.; Rodriguez, A. D.; Vahidi, S. Unraveling the Mechanism of Electrospray Ionization. *Anal. Chem.* **2013**, *85* (1), 2–9. https://doi.org/10.1021/ac302789c.

(4) Karas, M.; Bahr, U.; Dülcks, T. Nano-Electrospray Ionization Mass Spectrometry: Addressing Analytical Problems beyond Routine. *Fresenius J Anal Chem* **2000**, *366* (6), 669–676. https://doi.org/10.1007/s002160051561.

(5) Wilm, M. S.; Mann, M. Electrospray and Taylor-Cone Theory, Dole's Beam of Macromolecules at Last? *International Journal of Mass Spectrometry and Ion Processes* **1994**, *136* (2), 167–180. https://doi.org/10.1016/0168-1176(94)04024-9.

(6) Davidson, K. L.; Oberreit, D. R.; Hogan, C. J.; Bush, M. F. Nonspecific Aggregation in Native Electrokinetic Nanoelectrospray Ionization. *International Journal of Mass Spectrometry* **2017**, *420* (Supplement C), 35–42. https://doi.org/10.1016/j.ijms.2016.09.013.

(7) Wilm, M.; Mann, M. Analytical Properties of the Nanoelectrospray Ion Source. *Anal. Chem.* **1996**, *68* (1), 1–8. https://doi.org/10.1021/ac9509519.

(8) El-Faramawy, A.; Siu, K. W. M.; Thomson, B. A. Efficiency of Nano-Electrospray Ionization. *J Am Soc Mass Spectrom* **2005**, *16* (10), 1702–1707. https://doi.org/10.1016/j.jasms.2005.06.011.

(9) Tang, X.; Bruce, J. E.; Hill, H. H. Characterizing Electrospray Ionization Using Atmospheric Pressure Ion Mobility Spectrometry. *Anal. Chem.* **2006**, *78* (22), 7751–7760. https://doi.org/10.1021/ac0613380.

(10) Juraschek, R.; Dülcks, T.; Karas, M. Nanoelectrospray—More than Just a Minimized-Flow Electrospray Ionization Source. *J. Am. Soc. Mass Spectrom.* **1999**, *10* (4), 300–308. https://doi.org/10.1021/jasms.8b01315.

(11) Heck, A. J. R. Native Mass Spectrometry: A Bridge between Interactomics and Structural Biology. *Nature Methods* **2008**, *5* (11), 927–933. https://doi.org/10.1038/nmeth.1265.

(12) Leney, A. C.; Heck, A. J. R. Native Mass Spectrometry: What Is in the Name? *J. Am. Soc. Mass Spectrom.* **2017**, *28* (1), 5–13. https://doi.org/10.1007/s13361-016-1545-3.

(13) Laszlo, K. J.; Bush, M. F. Analysis of Native-Like Proteins and Protein Complexes Using Cation to Anion Proton Transfer Reactions (CAPTR). *J. Am. Soc. Mass Spectrom.* **2015**, *26* (12), 2152–2161. https://doi.org/10.1007/s13361-015-1245-4.

(14) Donnelly, D. P.; Rawlins, C. M.; DeHart, C. J.; Fornelli, L.; Schachner, L. F.; Lin, Z.; Lippens, J. L.; Aluri, K. C.; Sarin, R.; Chen, B.; Lantz, C.; Jung, W.; Johnson, K. R.; Koller, A.; Wolff, J. J.; Campuzano, I. D. G.; Auclair, J. R.; Ivanov, A. R.; Whitelegge, J. P.; Paša-Tolić, L.; Chamot-Rooke, J.; Danis, P. O.; Smith, L. M.; Tsybin, Y. O.; Loo, J. A.; Ge, Y.; Kelleher, N. L.; Agar, J. N. Best Practices and Benchmarks for Intact Protein Analysis for Top-down Mass Spectrometry. *Nature Methods* **2019**, *16* (7), 587–594. https://doi.org/10.1038/s41592-019-0457-0.

(15) Konermann, L. Addressing a Common Misconception: Ammonium Acetate as Neutral PH "Buffer" for Native Electrospray Mass Spectrometry. *J. Am. Soc. Mass Spectrom.* **2017**, *28* (9), 1827–1835. https://doi.org/10.1007/s13361-017-1739-3.

(16) Stoll, V. S.; Blanchard, J. S. Chapter 6 Buffers: Principles and Practice1. In *Methods in Enzymology*; Burgess, R. R., Deutscher, M. P., Eds.; Guide to Protein Purification, 2nd Edition; Academic Press, 2009; Vol. 463, pp 43–56. https://doi.org/10.1016/S0076-6879(09)63006-8.

(17) Susa, A. C.; Xia, Z.; Williams, E. R. Small Emitter Tips for Native Mass Spectrometry of Proteins and Protein Complexes from Nonvolatile Buffers That Mimic the Intracellular Environment. *Anal. Chem.* **2017**, *89* (5), 3116–3122. https://doi.org/10.1021/acs.analchem.6b04897.

(18) Cassou, C. A.; Sterling, H. J.; Susa, A. C.; Williams, E. R. Electrothermal Supercharging in Mass Spectrometry and Tandem Mass Spectrometry of Native Proteins. *Anal Chem* **2013**, *85* (1), 138–146. https://doi.org/10.1021/ac302256d.

(19) Hedges, J. B.; Vahidi, S.; Yue, X.; Konermann, L. Effects of Ammonium Bicarbonate on the Electrospray Mass Spectra of Proteins: Evidence for Bubble-Induced Unfolding. *Anal Chem* **2013**, *85* (13), 6469–6476. https://doi.org/10.1021/ac401020s.

(20) Cassou, C. A.; Williams, E. R. Anions in Electrothermal Supercharging of Proteins with Electrospray Ionization Follow a Reverse Hofmeister Series. *Anal. Chem.* **2014**, *86* (3), 1640–1647. https://doi.org/10.1021/ac403398j.

(21) Mora, J. F. de la; Berkel, G. J. V.; Enke, C. G.; Cole, R. B.; Martinez-Sanchez, M.; Fenn, J. B. Electrochemical Processes in Electrospray Ionization Mass Spectrometry. *Journal of Mass Spectrometry 35* (8), 939–952. https://doi.org/10.1002/1096-9888(200008)35:8<939::AID-JMS36>3.0.CO;2-V.

(22) Blades, A. T.; Ikonomou, M. G.; Kebarle, Paul. Mechanism of Electrospray Mass Spectrometry. Electrospray as an Electrolysis Cell. *Anal. Chem.* **1991**, *63* (19), 2109–2114. https://doi.org/10.1021/ac00019a009.

(23) Taylor Geoffrey Ingram. Disintegration of Water Drops in an Electric Field. *Proceedings of the Royal Society of London. Series A. Mathematical and Physical Sciences* **1964**, *280* (1382), 383–397. https://doi.org/10.1098/rspa.1964.0151.

(24) Zhou, S.; Edwards, A. G.; Cook, K. D.; Van Berkel, G. J. Investigation of the Electrospray Plume by Laser-Induced Fluorescence Spectroscopy. *Anal. Chem.* **1999**, *71* (4), 769–776. https://doi.org/10.1021/ac981259r.

(25) Jackson, G. S.; Enke, C. G. Electrical Equivalence of Electrospray Ionization with Conducting and Nonconducting Needles. *Anal. Chem.* **1999**, *71* (17), 3777–3784. https://doi.org/10.1021/ac9902244.

(26) Kebarle, P.; Verkerk, U. H. Electrospray: From Ions in Solution to Ions in the Gas Phase, What We Know Now. *Mass Spectrometry Reviews* **2009**, *28* (6), 898–917. https://doi.org/10.1002/mas.20247.

(27) Van Berkel, G. J.; Zhou, Feimeng.; Aronson, J. T. Changes in Bulk Solution PH Caused by the Inherent Controlled-Current Electrolytic Process of an Electrospray Ion Source. *International Journal of Mass Spectrometry and Ion Processes* **1997**, *162* (1–3), 55–67. https://doi.org/10.1016/S0168-1176(96)04476-X.

(28) Berkel, G. J. V. Electrolytic Corrosion of a Stainless-Steel Electrospray Emitter Monitored Using an Electrospray–Photodiode Array System. *J. Anal. At. Spectrom.* **1998**, *13* (7), 603–607. https://doi.org/10.1039/A800373D.

(29) Van Berkel, G. J.; Asano, K. G.; Schnier, P. D. Electrochemical Processes in a Wire-in-a-Capillary Bulk-Loaded, Nano-Electrospray Emitter. *Journal of the American Society for Mass Spectrometry* **2001**, *12* (7), 853–862. https://doi.org/10.1016/S1044-0305(01)00264-1.

(30) Van Berkel, G. J.; Kertesz, V. Using the Electrochemistry of the Electrospray Ion Source. *Anal. Chem.* **2007**, *79* (15), 5510–5520. https://doi.org/10.1021/ac071944a.

(31) Van Berkel, G. J.; Zhou, Feimeng. Characterization of an Electrospray Ion Source as a Controlled-Current Electrolytic Cell. *Anal. Chem.* **1995**, *67* (17), 2916–2923. https://doi.org/10.1021/ac00113a028.

(32) Pan, P.; McLuckey, S. A. The Effect of Small Cations on the Positive Electrospray Responses of Proteins at Low PH. *Anal. Chem.* **2003**, *75* (20), 5468–5474. https://doi.org/10.1021/ac034344u.

(33) Pan, P.; Gunawardena, H. P.; Xia, Y.; McLuckey, S. A. Nanoelectrospray Ionization of Protein Mixtures: Solution PH and Protein PI. *Anal. Chem.* **2004**, *76* (4), 1165–1174. https://doi.org/10.1021/ac035209k.

(34) Hiraoka, K.; Aizawa, K.; Murata, K.; Fujimaki, S. Electrochemical Reduction and Highly-Sensitive Analysis of Iodine in Electrospray Mass Spectrometry. *Journal of the Mass Spectrometry Society of Japan* **1995**, *43* (1), 77–83. https://doi.org/10.5702/massspec.43.77.

(35) Dupont, A.; Gisselbrecht, J.-P.; Leize, E.; Wagner, L.; Van Dorsselaer, A. Electrospray Mass Spectrometry of Electrochemically Ionized Molecules : Application to the Study of Fullerenes. *Tetrahedron Letters* **1994**, *35* (33), 6083–6086. https://doi.org/10.1016/0040-4039(94)88081-6.

(36) Hop, C. E. C. A.; Saulys, D. A.; Gaines, D. F. Electrospray Mass Spectrometry of Borane Salts: The Electrospray Needle as an Electrochemical Cell. *J. Am. Soc. Mass Spectrom.* **1995**, *6* (9), 860–865. https://doi.org/10.1021/jasms.8b00763.

(37) Vandell, V. E.; Limbach, P. A. Electrospray Ionization Mass Spectrometry of Metalloporphyrins. *Journal of Mass Spectrometry* **1998**, *33* (3), 212–220. https://doi.org/10.1002/(SICI)1096-9888(199803)33:3<212::AID-JMS619>3.0.CO;2-E.

(38) Pozniak, B. P.; Cole, R. B. Perspective on Electrospray Ionization and Its Relation to Electrochemistry. *J. Am. Soc. Mass Spectrom.* **2015**, *26* (3), 369–385. https://doi.org/10.1007/s13361-014-1066-x.

(39) Guaratini, T.; Vessecchi, R.; Pinto, E.; Colepicolo, P.; Lopes, N. P. Balance of Xanthophylls Molecular and Protonated Molecular Ions in Electrospray Ionization. *Journal of Mass Spectrometry* **2005**, *40* (7), 963–968. https://doi.org/10.1002/jms.874.

(40) Xu, Xiaoming.; Nolan, S. P.; Cole, R. B. Electrochemical Oxidation and Nucleophilic Addition Reactions of Metallocenes in Electrospray Mass Spectrometry. *Anal. Chem.* **1994**, *66* (1), 119–125. https://doi.org/10.1021/ac00073a021.

(41) Rondeau, D.; Kreher, D.; Cariou, M.; Hudhomme, P.; Gorgues, A.; Richomme, P. Electrolytic Electrospray Ionization Mass Spectrometry of C60-TTF-C60 Derivatives: High-Resolution Mass Measurement and Molecular Ion Gas-Phase Reactivity. *Rapid Communications in Mass Spectrometry* **2001**, *15* (18), 1708–1712. https://doi.org/10.1002/rcm.423.

(42) Pei, J.; Zhou, X.; Wang, X.; Huang, G. Alleviation of Electrochemical Oxidation for Peptides and Proteins in Electrospray Ionization: Obtaining More Accurate Mass Spectra with Induced High Voltage. *Anal. Chem.* **2015**, *87* (5), 2727–2733. https://doi.org/10.1021/ac503990a.

(43) Gatlin, C. L.; Turecek, Frantisek. Acidity Determination in Droplets Formed by Electrospraying Methanol-Water Solutions. *Anal. Chem.* **1994**, *66* (5), 712–718. https://doi.org/10.1021/ac00077a021.

(44) Zhou, S.; Prebyl, B. S.; Cook, K. D. Profiling PH Changes in the Electrospray Plume. *Anal. Chem.* **2002**, *74* (19), 4885–4888. https://doi.org/10.1021/ac025960d.

(45) Rajagopal, P.; Tse, E.; Borst, A. J.; Delbecq, S. P.; Shi, L.; Southworth, D. R.; Klevit, R. E. A Conserved Histidine Modulates HSPB5 Structure to Trigger Chaperone Activity in Response to Stress-Related Acidosis. *eLife 4*. https://doi.org/10.7554/eLife.07304.

(46) Santos, J.; Iglesias, V.; Santos-Suárez, J.; Mangiagalli, M.; Brocca, S.; Pallarès, I.; Ventura, S. PH-Dependent Aggregation in Intrinsically Disordered Proteins Is Determined by Charge and Lipophilicity. *Cells* **2020**, *9* (1). https://doi.org/10.3390/cells9010145.

(47) Santambrogio, C.; Natalello, A.; Brocca, S.; Ponzini, E.; Grandori, R. Conformational Characterization and Classification of Intrinsically Disordered Proteins by Native Mass Spectrometry and Charge-State Distribution Analysis. *Proteomics* **2019**, *19* (6), e1800060. https://doi.org/10.1002/pmic.201800060.

(48) Chingin, K.; Barylyuk, K.; Chen, H. On the Preservation of Non-Covalent Protein Complexes during Electrospray Ionization. *Philos Trans A Math Phys Eng Sci* **2016**, *374* (2079). https://doi.org/10.1098/rsta.2015.0377.

(49) Meyer, T.; Gabelica, V.; Grubmüller, H.; Orozco, M. Proteins in the Gas Phase. *WIREs Computational Molecular Science* **2013**, *3* (4), 408–425. https://doi.org/10.1002/wcms.1130.

(50) Gadzuk-Shea, M. M.; Bush, M. F. Effects of Charge State on the Structures of Serum Albumin Ions in the Gas Phase: Insights from Cation-to-Anion Proton-Transfer Reactions, Ion Mobility, and Mass Spectrometry. *J. Phys. Chem. B* **2018**, *122* (43), 9947–9955. https://doi.org/10.1021/acs.jpcb.8b08427.

(51) Thompson, N. J.; Rosati, S.; Heck, A. J. R. Performing Native Mass Spectrometry Analysis on Therapeutic Antibodies. *Methods* **2014**, *65* (1), 11–17. https://doi.org/10.1016/j.ymeth.2013.05.003.

(52) Raimondo, J. V.; Irkle, A.; Wefelmeyer, W.; Newey, S. E.; Akerman, C. J. Genetically Encoded Proton Sensors Reveal Activity-Dependent PH Changes in Neurons. *Front Mol Neurosci* **2012**, *5*. https://doi.org/10.3389/fnmol.2012.00068.

(53) Grynkiewicz, G.; Poenie, M.; Tsien, R. Y. A New Generation of Ca2+ Indicators with Greatly Improved Fluorescence Properties. *J Biol Chem* **1985**, *260* (6), 3440–3450.

(54) Waser, J. Acid-Base Titration and Distribution Curves. *J. Chem. Educ.* **1967**, *44* (5), 274. https://doi.org/10.1021/ed044p274.

(55) Marcotte, N.; Brouwer, A. M. Carboxy SNARF-4F as a Fluorescent PH Probe for Ensemble and Fluorescence Correlation Spectroscopies. *J. Phys. Chem. B* **2005**, *109* (23), 11819–11828. https://doi.org/10.1021/jp0510138.

(56) Bush, M. F.; Hall, Z.; Giles, K.; Hoyes, J.; Robinson, C. V.; Ruotolo, B. T. Collision Cross Sections of Proteins and Their Complexes: A Calibration Framework and Database for Gas-Phase Structural Biology. *Anal. Chem.* **2010**, *82* (22), 9557–9565. https://doi.org/10.1021/ac1022953.

(57) Hernández, H.; Robinson, C. V. Determining the Stoichiometry and Interactions of Macromolecular Assemblies from Mass Spectrometry. *Nat Protoc* **2007**, *2* (3), 715–726. https://doi.org/10.1038/nprot.2007.73.

(58) Österlund, N.; Moons, R.; Ilag, L. L.; Sobott, F.; Gräslund, A. Native Ion Mobility-Mass Spectrometry Reveals the Formation of β-Barrel Shaped Amyloid-β Hexamers in a Membrane-Mimicking Environment. *J. Am. Chem. Soc.* **2019**, *141* (26), 10440–10450. https://doi.org/10.1021/jacs.9b04596.

(59) Gabelica, V.; Livet, S.; Rosu, F. Optimizing Native Ion Mobility Q-TOF in Helium and Nitrogen for Very Fragile Noncovalent Structures. *J. Am. Soc. Mass Spectrom.* **2018**, *29* (11), 2189–2198. https://doi.org/10.1021/jasms.8b05701.

(60) Wyttenbach, T.; Bowers, M. T. Structural Stability from Solution to the Gas Phase: Native Solution Structure of Ubiquitin Survives Analysis in a Solvent-Free Ion Mobility–Mass Spectrometry Environment | The Journal of Physical Chemistry B https://pubs-acs-org.offcampus.lib.washington.edu/doi/full/10.1021/jp206867a (accessed Nov 5, 2020).

(61) Schmidt, A.; Karas, M.; Dülcks, T. Effect of Different Solution Flow Rates on Analyte Ion Signals in Nano-ESI MS, or: When Does ESI Turn into Nano-ESI? *J Am Soc Mass Spectrom* **2003**, *14* (5), 492–500. https://doi.org/10.1016/S1044-0305(03)00128-4.

(62) Chen, S.-H.; Russell, D. H. How Closely Related Are Conformations of Protein Ions Sampled by IM-MS to Native Solution Structures? *J. Am. Soc. Mass Spectrom.* **2015**, *26* (9), 1433–1443. https://doi.org/10.1007/s13361-015-1191-1.

(63) Sterling, H. J.; Batchelor, J. D.; Wemmer, D. E.; Williams, E. R. Effects of Buffer Loading for Electrospray Ionization Mass Spectrometry of a Noncovalent Protein Complex That Requires High Concentrations of Essential Salts. *J Am Soc Mass Spectrom* **2010**, *21* (6), 1045–1049. https://doi.org/10.1016/j.jasms.2010.02.003.

(64) Gavriilidou, A. F. M.; Gülbakan, B.; Zenobi, R. Influence of Ammonium Acetate Concentration on Receptor–Ligand Binding Affinities Measured by Native Nano ESI-MS: A Systematic Study. *Anal. Chem.* **2015**, *87* (20), 10378–10384. https://doi.org/10.1021/acs.analchem.5b02478.

(65) Zhou, M.; Sandercock, A. M.; Fraser, C. S.; Ridlova, G.; Stephens, E.; Schenauer, M. R.; Yokoi-Fong, T.; Barsky, D.; Leary, J. A.; Hershey, J. W.; Doudna, J. A.; Robinson, C. V. Mass Spectrometry Reveals Modularity and a Complete Subunit Interaction Map of the Eukaryotic Translation Factor EIF3. *PNAS* **2008**, *105* (47), 18139–18144. https://doi.org/10.1073/pnas.0801313105.

(66) Hong, S.; Bush, M. F. Collision-Induced Unfolding Is Sensitive to the Polarity of Proteins and Protein Complexes. *J. Am. Soc. Mass Spectrom.* **2019**, *30* (11), 2430–2437. https://doi.org/10.1021/jasms.8b06263.

(67) Xia, Z.; DeGrandchamp, J. B.; Williams, E. R. Native Mass Spectrometry beyond Ammonium Acetate: Effects of Nonvolatile Salts on Protein Stability and Structure. *Analyst* **2019**, *144* (8), 2565–2573. https://doi.org/10.1039/C9AN00266A.

Appendix A

SUPPORTING INFORMATION

Triboelectric nanogenerators (TENG) devices for improved sample consumption in ion mobility mass spectrometry analysis of protein and protein complex ions

---

Meagan Gadzuk-Shea, Hikari Akasaki, Ben Zercher, and Matthew F. Bush

Table of Contents

Determining Ω values from arrival-time distributions

Determination of transport time of ions from exit of drift cell to time-of-flight mass analyzer. This section has been reproduced from Allen *et al*.[1] In the experimental setup used in this work, the drift voltage can be varied up to 354 V. The centroid of each arrival-time distribution is estimated by fitting the distribution to a Gaussian function using in-house software.[2] For mobility experiments, arrival times were measured at 10 drift voltages ranging from 104 to 354 V for all charge states observed of each protein. Plotting arrival time versus reciprocal drift voltage enables the determination of t_0, the time for ions to exit the drift cell and reach to time-of-flight mass analyzer. Experimental arrival times were corrected for this transport prior to calculating Ω values.

Converting from arrival-time to collision-cross-section. This section has largely been reproduced from Laszlo *et al.*[3] Arrival time (t_A) measurements in ion mobility experiments include the mobility-dependent drift time (t_D) and the time for ions to exit the drift cell and reach to time-of-flight mass analyzer (t_0):

$$t_A = t_D + t_0 \quad \text{(Equation S1)}$$

Where t_D is defined:

$$t_D = \frac{(\text{length of drift cell})^2}{KV} \quad \text{(Equation S2)}$$

where K is defined as the mobility of the ion and V is the voltage drop across the drift cell. t_0 is defined as:

$$t_0 = t_{ind} + t_{m/z} \quad \text{(Equation S3)}$$

and $t_{m/z}$ is defined by:[4]

$$t_{m/z} = \frac{c\sqrt{m/z}}{1000} \quad \text{(Equation S4)}$$

where *c* is an instrument specific parameter call the 'enhanced duty cycle delay coefficient. With this relationship, Equation S1 can be rewritten as:

$$t_D = \frac{(\text{length of drift cell})^2}{KV} = t_A - \left(t_{ind} + \frac{c\sqrt{m/z}}{1000}\right) \quad \text{(Equation S5)}$$

For this work, t_0 is determined by field-dependent measurements of precursor ions, using a previously explained approach.[1] Equation S5 can be rewritten as:

$$\frac{1}{K} = \frac{\left[t_A - \left(t_{ind} + \frac{c\sqrt{m/z}}{1000}\right)\right] * V}{(\text{length of drift cell})^2} \quad \text{(Equation S6)}$$

The mobility can then be converted to a collision cross section (Ω) using the Mason-Schamp equation:[5]

$$\Omega = \frac{3ez}{16N}\left(\frac{2\pi}{\mu k_B T}\right)^{1/2}\frac{1}{K} \quad \text{(Equation S7)}$$

Substituting equation S6 into S7 yields:

$$\Omega = \frac{3ez}{16N}\left(\frac{2\pi}{\mu k_B T}\right)^{1/2} \frac{\left[t_A - \left(t_{ind} + \frac{c\sqrt{m/z}}{1000}\right)\right] * V}{(\text{length of drift cell})^2} \qquad \text{(Equation S8)}$$

where *e* is the fundamental charge, *z* is the charge state, N is the number density of the drift gas, μ is the reduced mass of the ion and drift gas, k_B is the Boltzmann constant, and T is the drift-gas temperature. This relationship enables experimental t_D to be converted to Ω.

Cumulative distribution functions (CDF) for each Ω distribution were calculated to determine critical values from the Ω distribution. To do so, critical Ω values corresponding to the 10%, 50%, and 90% of the CDF were used to describe the lower bound, median, and upper bound of the distribution, respectively.

Table A1. Typical IM settings for minimal activation of ions introduced into the instrument

Parameter	Typical Setting Range	Unit
Capillary potential	0.6-1.0	kV
Sampling cone	20-50	V
Source temperature	30	˚C
Trap collision energy	5	V
Trap gas flow	4	$mL \cdot min^{-1}$
IM gas flow	175	$mL \cdot min^{-1}$
Trap entrance	0-1	V
Trap bias	5-10	V
Trap exit	1	V
Backing pressure	4.5-7.0	mbar
Trapping release time	200	µs

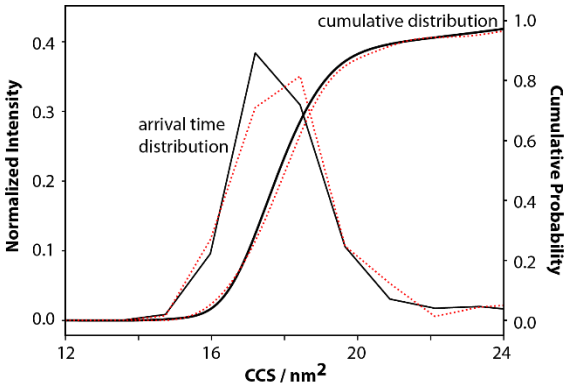

Figure A1. The Ω distribution resulting from ion mobility analysis of the 9+ ion of β-lactoglobulin monomer generated by DC power supply (solid black trace) and by TENG power supply (dashed red trace) and the corresponding cumulative distributions fit to the arrival times shown on the right axis. Ω values corresponding to 0.1, 0.5, and 0.9 are used to describe the widths of the observed distributions.

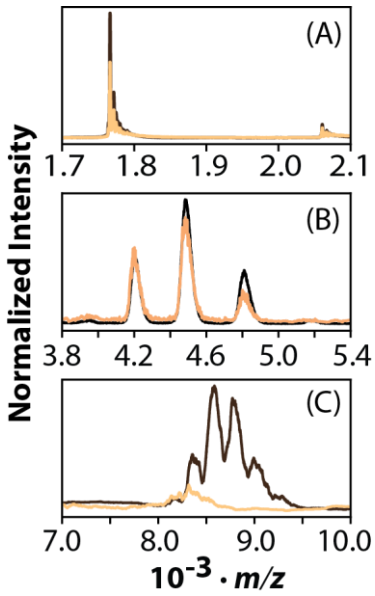

Figure A2. Comparison of mass spectra of cyctochrome *c* (A, molecular weight 12.4 kDa), albumin (B, molecular weight 67.3 kDa), and glutamate dehydrogenase (C, molecular weight 336 kDa) generated by DC power supply (black trace) and TENG power supply (orange trace).

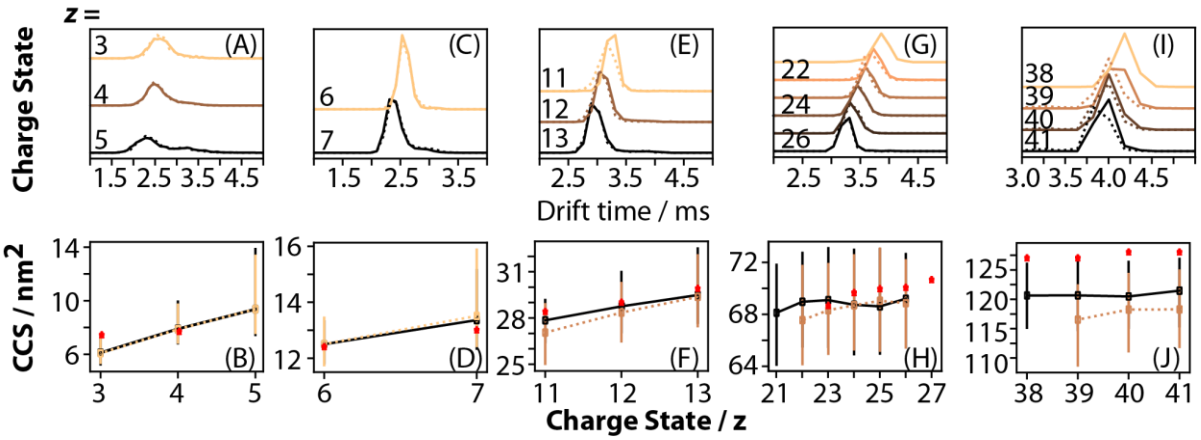

Figure A3. Ion mobility results of ions generated from DC power supply (solid traces) and from TENG power supply (dashed traces). The top row (A, C, E, G, I) displays the arrival time distributions of charge states produced from protein and protein complex ion populations. The bottom row (B, D, F, H, J) shows the Ω values from converting the arrival time axis to a collision cross section axis. Markers represent the median values of the cumulative distribution fit to the arrival time and the vertical bars span the 10% to 90% values of the cumulative distribution. Red markers correspond to Ω values from a collision cross section data base.[6,7] Protein and protein complex ions examined include monomeric insulin (A, B, 5.8 kDa), cytochrome *c* (C, D, molecular weight 12.4 kDa), dimeric β-lactoglobulin (E, F, 36.8 kDa), G3PD (G, H, 145 kDa), and GDH (I, J, 336 kDa).

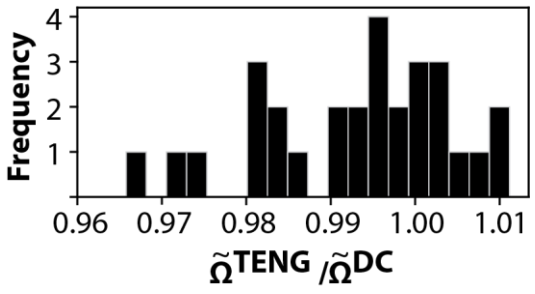

Figure A4. The ratio of $\widetilde{\Omega}$ values of ions generated by TENG power supply relative to those same ions generated by a DC power supply.

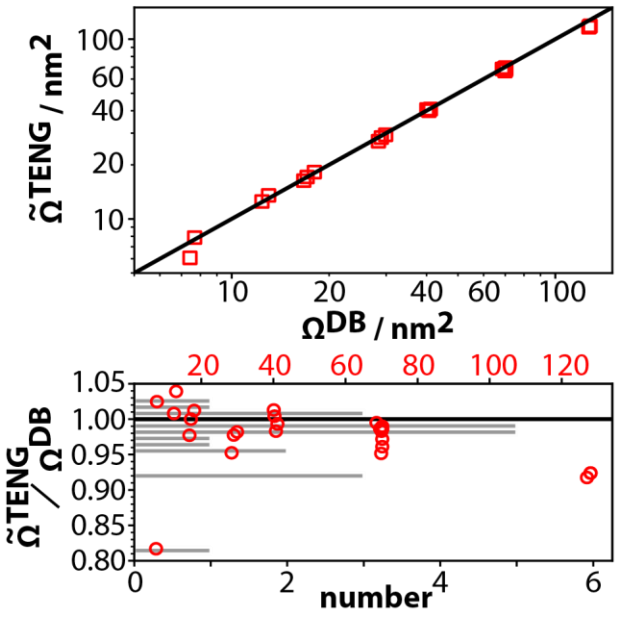

Figure A5. (A) comparison of $\tilde{\Omega}$ observed to Ω values that have been measured previously on the same and different IM–MS platforms. The black trace represents where the two values are equivalent to one another. (B) The ratios of the $\tilde{\Omega}$ measured using nESI^{TENG} relative to Ω values measured previously are shown against the Ω values measured previously along the top (red markers). The overlayed bar plot shows that most of the ions considered are within ±3% of each other, except for one gross outlier.

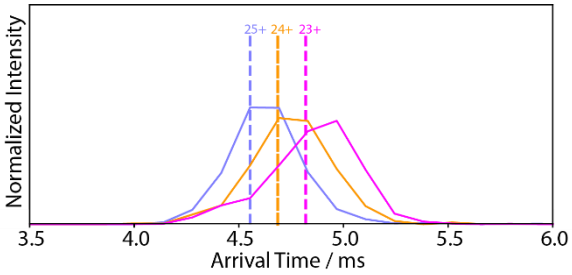

Figure A6. Arrival time distributions for the 23 – 25+ charge states of alcohol dehydrogenase ions generated by nESI^{TENG}. Dashed lines correspond to the 50% value from the cdf applied to the distribution. The lack of resolution between charge states precludes the determination of the source of shorter ATDs for ions generated by nESI^{TENG} relative to ions generated by nESI^{DC}.

(1) Allen, S. J.; Bush, M. F. Radio-Frequency (Rf) Confinement in Ion Mobility Spectrometry: Apparent Mobilities and Effective Temperatures. *J. Am. Soc. Mass Spectrom.* **2016**, *27* (12), 2054–2063. https://doi.org/10.1021/jasms.8b05184.

(2) Bush, M. F.; Campuzano, I. D. G.; Robinson, C. V. Ion Mobility Mass Spectrometry of Peptide Ions: Effects of Drift Gas and Calibration Strategies. *Anal. Chem.* **2012**, *84* (16), 7124–7130. https://doi.org/10.1021/ac3014498.

(3) Laszlo, K. J.; Munger, E. B.; Bush, M. F. Folding of Protein Ions in the Gas Phase after Cation-to-Anion Proton-Transfer Reactions. *J. Am. Chem. Soc.* **2016**, *138* (30), 9581–9588. https://doi.org/10.1021/jacs.6b04282.

(4) Ruotolo, B. T.; Benesch, J. L. P.; Sandercock, A. M.; Hyung, S.-J.; Robinson, C. V. Ion Mobility–Mass Spectrometry Analysis of Large Protein Complexes. *Nat. Protoc.* **2008**, *3* (7), 1139–1152. https://doi.org/10.1038/nprot.2008.78.

(5) Mason; E.A.; McDaniel; E.W. *Transport Properties of Ions in Gases*; Wiley: New York, 1988.

(6) Allen, S. J.; Giles, K.; Gilbert, T.; Bush, M. F. Ion Mobility Mass Spectrometry of Peptide, Protein, and Protein Complex Ions Using a Radio-Frequency Confining Drift Cell. *Analyst* **2016**, *141* (3), 884–891. https://doi.org/10.1039/c5an02107c.

(7) Allen, S. J.; Schwartz, A. M.; Bush, M. F. Effects of Polarity on the Structures and Charge States of Native-Like Proteins and Protein Complexes in the Gas Phase. *Anal. Chem.* **2013**, *85* (24), 12055–12061. https://doi.org/10.1021/ac403139d.

Appendix B

SUPPORTING INFORMATION

So *How* Bad is Ammonium Acetate for Native Mass Spectrometry? A Quantitation of pH Changes in Nanoelectrospray Ionization (nESI) Using a Fluorescent Probe

Meagan M. Gadzuk-Shea, Evan Hubbard, Matthew F. Bush*

Table of Contents

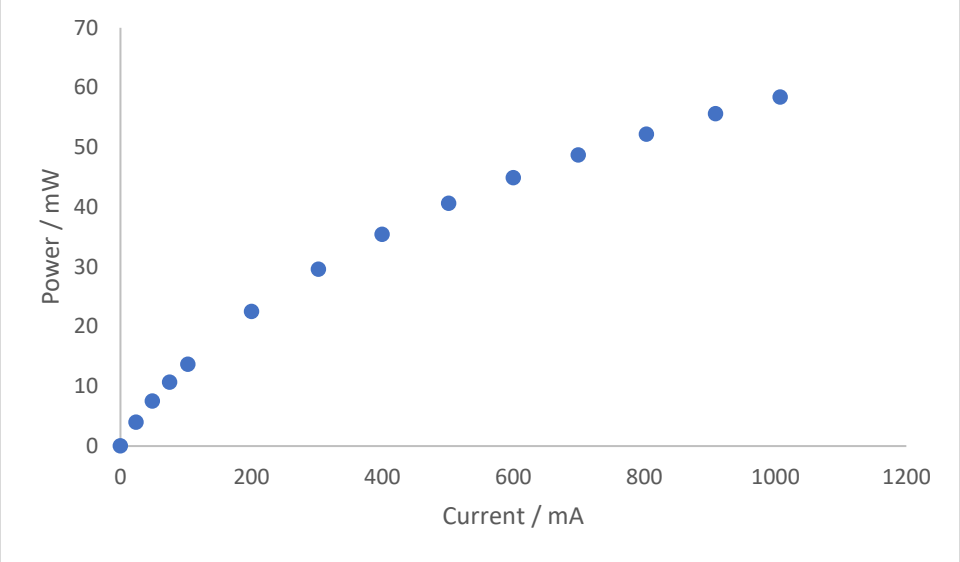

Figure B1 The power generated by the LED as a function of current set on the power supply

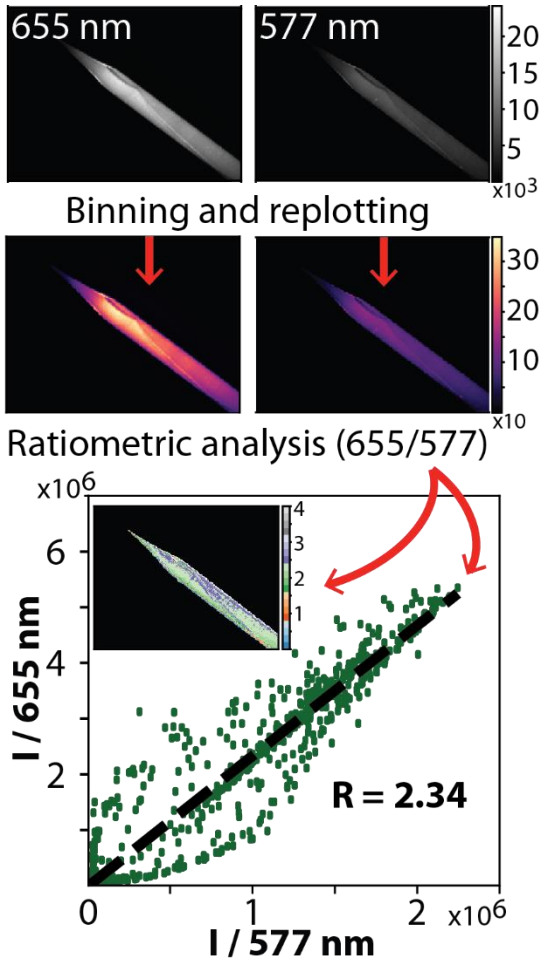

Figure B2 Experimental workflow to relate fluorescence to solution pH. The recorded fluorescence intensities at each wavelength were binned and a minimum and maximum threshold was applied to eliminate low intensity and "hot" pixels. The slope obtained from plotting the fluorescence intensities against each other was used as the fluorescence ratio for analysis. A pixel-based superimposition of the images using a qualitative colormap illustrates the variance of fluorescence throughout the capillary.

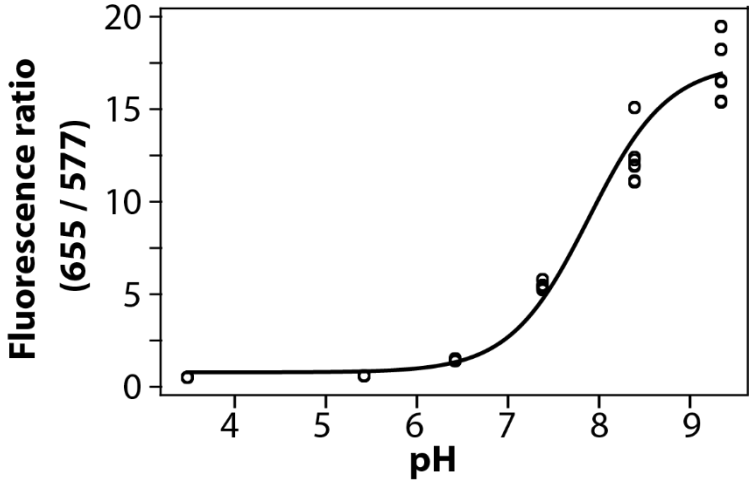

Figure B3 Calibration curve generated from measuring the fluorescence ratio of SNARF-4F prepared in ammonium phosphate solutions at known pH.

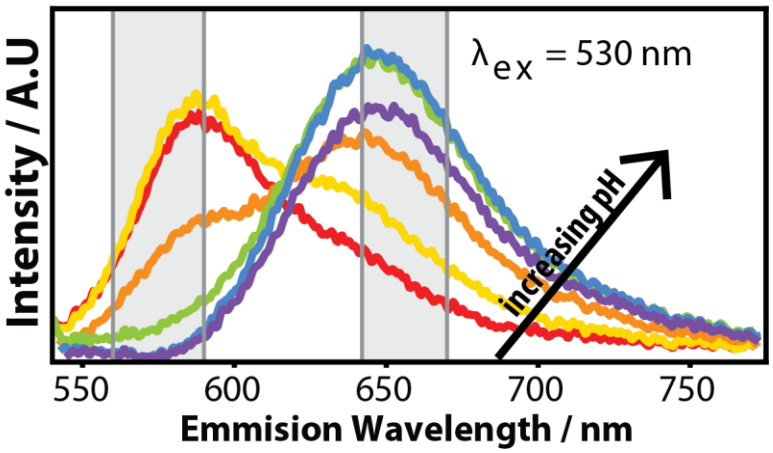

Figure B4. pH-dependent fluorescence of SNARF-4F at varying solution pH values. The feature observed around 650 nm increases with the alkalinity of the solution. The shaded regions represent the transmission windows of the bandpass filters used to detect the fluorescence in the experiment.

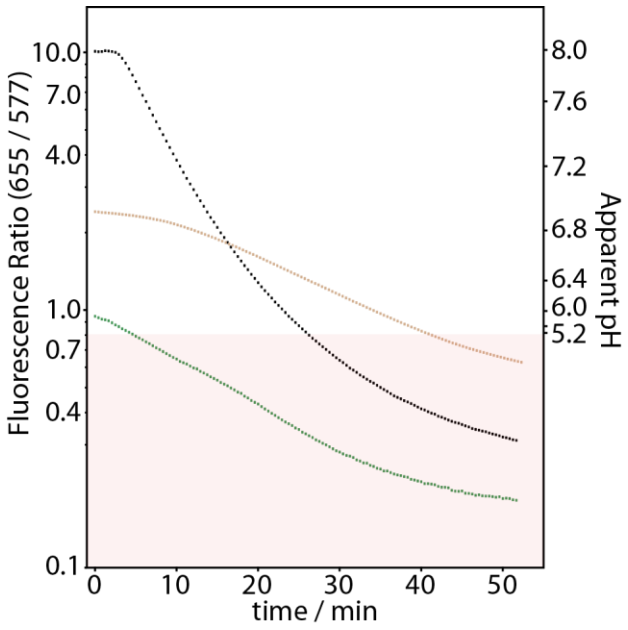

Figure B5. The effect of initial solution pH on the extent of pH changes during positive electrospray; the shaded red region represents solution pH values ≤ 5. All three solutions display decreases in solution pH greater than 1 pH unit. An initial pH of 8 (black trace) displays a short period of resistance to pH changes but shifts to rapid acidification indicated by a steep decrease in fluorescence ratio between 5—30 minutes. A solution starting at neutral pH (tan trace) exhibits slow acidification in the first 10 minutes and then more rapid acidification as time progresses. An initial solution pH of 6 (green trace) exhibits immediate acidification with the application of a potential which persists in a near linear fashion for the duration of the experiment.